Graduate School ETD Form 9
(Revised 12/07)

PURDUE UNIVERSITY
GRADUATE SCHOOL
Thesis/Dissertation Acceptance

This is to certify that the thesis/dissertation prepared

By Prasanna Chinnathambi

Entitled
Experimental Investigation on Traversing Hot Jet Ignition of Lean Hydrocarbon-Air Mixtures in a Constant Volume Combustor

For the degree of Master of Science in Mechanical Engineering

Is approved by the final examining committee:

M. Razi Nalim
Chair

Whitney Yu

Likun Zhu

To the best of my knowledge and as understood by the student in the *Research Integrity and Copyright Disclaimer (Graduate School Form 20)*, this thesis/dissertation adheres to the provisions of Purdue University's "Policy on Integrity in Research" and the use of copyrighted material.

Approved by Major Professor(s): M. Razi Nalim

Approved by: Sohel Anwar 12/03/2013
Head of the Graduate Program Date

EXPERIMENTAL STUDY OF TRAVERSING HOT-JET IGNITION OF LEAN HYDROCARBON-AIR MIXTURES IN A CONSTANT-VOLUME COMBUSTOR

A Thesis
Submitted to the Faculty
of
Purdue University
by
Prasanna Chinnathambi

In Partial Fulfillment of the
Requirements for the Degree
of
Master of Science in Mechanical Engineering

December 2013
Purdue University
Indianapolis, Indiana

ACKNOWLEDGEMENTS

Firstly I would like to express my greatest gratitude to my advisor, Professor Dr. Razi Nalim, for all the guidance throughout my Master's degree. His abundance of knowledge, experience and directions has aided me a lot in this research study. His Gas Dynamics class was the best one I had during this program. I would also like to thank Professor Dr. Whitney Yu and Dr. Likun Zhu for their time, good advice and proposing improvements on my thesis. Appreciation and thanks is also given to Ms. Valerie Lim Diemer and Ms. Vitanemi Sara for their help and guidance that was provided in helping me to prepare my thesis.

I am also very thankful to Dr. Manikanda Rajagopal, the post-doctoral research associate at CPRL and my lab mate Abdullah Karimi for sharing their knowledge and research experience which helped me in finding the right way to do conduct a research study. A special thanks to Joseph Huerkamp for his helps in lending me his laboratory tools during those really urgent times and for helping me with procuring lab hardware. Thanks to Robert Meager, the Linux guru for fixing all those Linux errors in a blink of the eye. A special thanks to MURI summer 2012 team who brought the ignition rig back to life and hence enabling this thesis.

Special thanks to my girlfriend Sakthi Murugan for her never ending love, support and care during this past two years. Without her the end result of this whole effort might not have felt as complete as it feels now. Last but definitely not the least, will be my thanks to my parents for helping me financially and for making those silent sacrifices in the background to give me a peace of mind to carry out this master's program.

TABLE OF CONTENTS

Page

Page

LIST OF TABLES

LIST OF FIGURES

Figure Page

Figure Page

Figure Page

Figure Page

Figure Page

Figure Page

Appendix Figure

ABSTRACT

Chinnathambi, Prasanna. M.S.M.E., Purdue University, December 2013. Experimental Study of Traversing Hot-Jet Ignition of Lean Hydrocarbon-Air Mixtures in a Constant-Volume Combustor. Major Professor: Mohamed Razi Nalim.

A constant-volume combustor is used to investigate the ignition initiated by a traversing jet of reactive hot gas, in support of combustion engine applications that include novel wave-rotor constant-volume combustion gas turbines and pre-chamber IC engines. The hot-jet ignition constant-volume combustor rig at the Combustion and Propulsion Research Laboratory at the Purdue School of Engineering and Technology at Indiana University-Purdue University Indianapolis (IUPUI) was used for this study. Lean premixed combustible mixture in a rectangular cuboid constant-volume combustor is ignited by a hot-jet traversing at different fixed speeds. The hot jet is issued via a converging nozzle from a cylindrical pre-chamber where partially combusted products of combustion are produced by spark- igniting a rich ethylene-air mixture. The main constant-volume combustor (CVC) chamber uses methane-air, hydrogen-methane-air and ethylene-air mixtures in the lean equivalence ratio range of 0.8 to 0.4. Ignition delay times and ignitability of these combustible mixtures as affected by jet traverse speed, equivalence ratio, and fuel type are investigated in this study.

The current study developed the experimental procedure and conducted preliminary studies to establish guidelines for operating the rig with the traversing nozzle arrangement. Combustion is observed through optically accessible windows that are provided on both sides of the rectangular chamber and used in conjunction with high-speed videography and image processing. Fast response dynamic pressure transducers are

mounted flush on the top wall to record the pressure time history in the main chamber. The nozzle is traversed across the main chamber entrance by spinning the pre-chamber. The procedures established allowed ignition studies to be conducted up until the pre-chamber rotation speed of 1500 rpm, which corresponds to a jet traverse time of 4.1 ms.

Mixing phenomena due to the traversing jet appears to dominate over chemical kinetics phenomenon in determining ignition delay. The high-speed images revealed the importance of jet dynamics on ignition and flame propagation of the fuel-air mixture. The supporting pressure traces highlighted the burning rates of the fuel and peak pressure achieved across the equivalence ratios and jet traverse speeds. Ignition delay time for methane-air mixtures is typically a few milliseconds, while ethylene-air mixtures were able to exhibit less than a millisecond delay time across the traverse speeds tested. Blended methane-hydrogen fuel exhibited shorter ignition delay than methane, as well as faster apparent flame propagation speed.

All the fuels tested exhibited the lowest ignition delay for a jet traverse time of 6.1 ms. The delay time increased further as the traverse speed of the nozzle increased. The ignitability of the fuel was found to decrease as the traverse time increased past 6.1 ms. Ignition failed for methane-air mixtures at the minimum nozzle traverse time of 4.1 ms.

1. INTRODUCTION

1.1 Background

Hot-jet ignition is a process that utilizes turbulent jets of reactive gases (partially combusted) as an ignition source. These gases are generated by combusting a fuel-air mixture in a separate pre-chamber which is usually slightly rich and spark-ignited. The gases are injected into the main combustion chamber via one or more nozzles. Such ignition finds applications in lean burn internal combustion (IC) engines [1-3], pulse detonation engines (PDE) [4-6] and wave rotor combustors [7-9]. The high energy ignition source provides benefits by its superior ability to achieve ignition and faster combustion rates even in traditionally slow burning fuel-lean mixtures. The penetrating and distributed nature of the jets creates multiple ignition sites, enabling small flame travel distance and thus short combustion durations [10]. The existence of chemically reactive intermediate products (active radicals H and OH) in addition to high levels of turbulence in the jets is reported to cause an energy level more than two orders of magnitude than a spark [11]. In a reported experiment, combustion was twice as fast and with a maximum pressure rise of 10% higher than spark ignition method [2].

The ignition characteristics of these jets is dictated by a combination of chemical, thermal and turbulent effects [12] while the fluid mechanical structure of the jet is characterized by Reynolds number associated with the flow and the main chamber geometry. As the gas flows through the pre-chamber orifice it is accelerated by the effect of area ratio dictated by the nozzle geometry. Counter rotating vortices govern the mixing process which moves across the main chamber geometry [13]. Although jet ignition systems provide additional ignition energy, there are heat losses due to the additional surface area of the pre-chamber. However by combusting lean mixtures there can be an overall increase in engine efficiency [14].

In hot jet ignition studies ignition delay time is a key parameter in characterizing the ignition process. The ignition delay time for a jet-ignited constant volume combustor (CVC) may be defined as the time from jet initiation to the occurrence of rapid, visible, and pressure-generating heat release in the CVC chamber [15].

The hot-jet ignition constant-volume combustor (CVC) rig currently being operated at the IUPUI utilizes a chemically reactive hot jet issued from a converging nozzle of 6 mm exit radius as the ignition source. Schematic of the rig in experiment ready position is shown in Figure 1. Ignition is achieved by injecting the hot jet in the main CVC chamber, which is a long rectangular constant volume combustion chamber with a square cross section. The configuration allows different fuel air mixtures maintained at different initial conditions in each one of the chambers. The nozzle is attached to the pre-chamber, but separated by an aluminum diaphragm. The main chamber and the pre-chamber remains as separate closed systems until the pressure rise due to pre-chamber combustion ruptures the diaphragm that seals the nozzle entrance. The experimental setup allows flow visualization and incorporates instrumentation to study the fundamental physics of the hot jet ignition process.

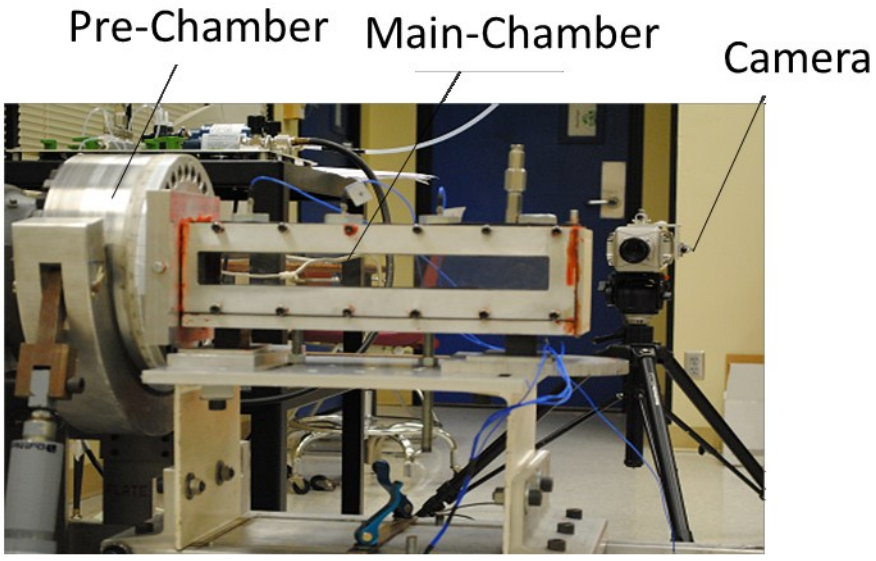

Figure 1. 1 Constant Volume Combustor (CVC) rig

1.2. Applications in Wave Rotor Combustor

An older version of the CVC rig was originally built by Bilgin [16] at the University of Washington to represent a channel in a wave rotor combustor. Wave-rotor CVC (WRCVC), shown in Figure. 1.2 a, is a pressure gain combustor having substantially steady inflow and outflow, although non steady process occurs within the combustor system in order to generate a higher stagnation pressure at the outlet than at the inlet. Figure 1.2 b illustrates the sequence of events as seen during a WRCVC operation in an unwrapped or developed view. . The gas dynamic process of compression, shock and expansion waves plays a vital role in wave rotor combustor's functionality [8].During operation, several combustor channels receive combustible mixtures via the inlet duct. The mixture is later ignited and combustion proceeds under constant volume conditions. The combusted products are expelled as high pressure gas to the turbine.

Proposed ignition methods for wave rotor include a sparkplug device, a laser device, a separately fueled pre-chamber, a crossfire tube that delivers hot combusted gas from a previously burned channel or a combination of these methods [9]. The ignition source should satisfy the requirements of wave rotor to:

1) Develop and use pressure rapidly enough to minimize losses from heat transfer and leakage
2) Minimize nitrogen oxide and other emissions
3) Complete combustion in an equitable fraction of total cycle time.

All these requirements demand faster combustion rates. The wave rotor combustor has to ensure that it is able to ignite the combustible mixture as well as completely combust the channel contents to ensure the combustion process is completed while the channels are closed at both ends. This only leaves the combustor a fraction of the total cycle time to complete the combustion process.

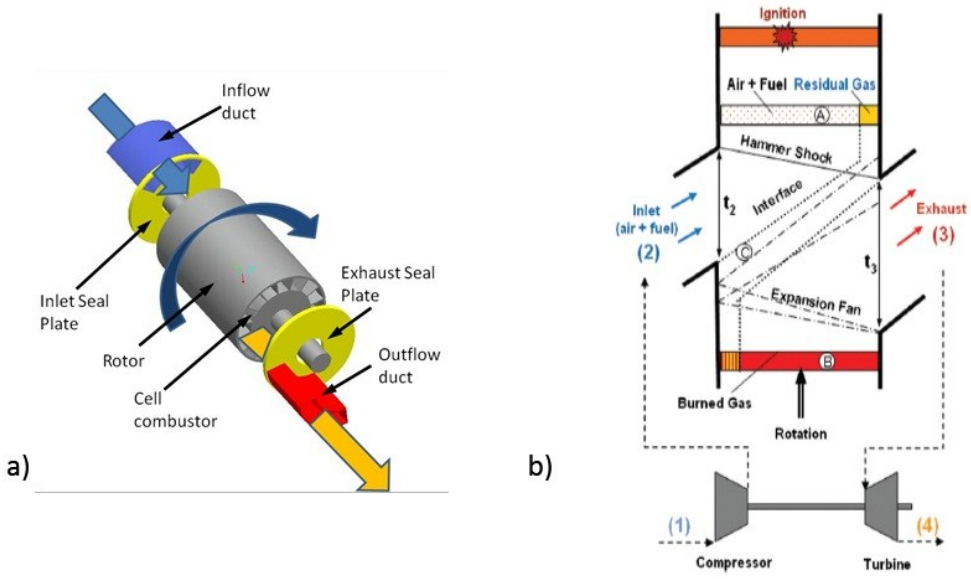

Figure 1. 2 a) Schematic configuration of a wave rotor combustor from the outlet b) Wave pattern in a developed view of a combustion wave rotor [8]

Hot jet ignition is one viable ignition process in wave rotor that can very well satisfy the ignition needs of a WRCVC. Wijeyakulasuriya [17] performed multidimensional CFD simulations on transient gas jets by setting nozzle geometry, chamber geometry and nozzle traverse speed as seen in the WRCVC. The study investigated the ignition potential of the traversing hot jet by exploring the interaction among the counter rotating vortices, interaction of vortices with confining walls and motion of the vortices due to interaction. Combustion was not numerically modelled in that study.

Similarly to the current study, the mixture in CVC chamber of Bilgin was ignited by a jet of hot combustion products from a separately fueled pre-chamber that could be spun to cause the jet to traverse across one end of the CVC [18]. The relative motion reproduces the action of a channel in a wave-rotor combustor and the pre-chamber may be representative of a previously combusted channel supplying hot gas. Bilgin [16] proposed a correlation between the Damköhler number and ignition of a fuel-air mixture in the CVC.

Using experimental data from this CVC rig and a computational fluid dynamics (CFD) code, Baronia [19] numerically simulated the stationary jet (the pre-chamber torch jet axially aligned with the channel axis) experiments using a four step combustion model. Perera [15] carried out experiments on the same CVC test rig for three different fuels – methane, ethylene, and propane by varying the equivalence ratios in the pre-chamber and the CVC chamber. The pre-chamber was set stationary and centered on the channel cross-section in these tests. The ignition delay time and the ignitability limits for both lean and rich mixtures were investigated for all the three fuels in the CVC chamber, for fixed operating conditions. Variation in ignition delay time was observed for fuels with different pre-chamber equivalence ratios and nozzle geometry. Expectedly, methane exhibited the highest ignition delay time while ethylene mixtures had the lowest ignition delay time. Ignition delay time was found to be lowest across all fuels and equivalence ratio range when ethylene was used as a pre-chamber fuel at equivalence ratio (Φ) of 1.1 issued by a converging nozzle with 5 mm exit diameter. Karimi [20] developed a two-dimensional model of the CVC rig to simulate the stationary and translating hot jet ignition process using a CFD code. Combustion was modeled using hybrid eddy-break-up model that considers finite-rate chemistry effects.

1.3 Applications in Pulse Detonation Engines

Several prior works involving intentional hot-jet ignition has been carried out for different applications. One such application was to determine the effectiveness of using a hot turbulent jet to initiate a detonation in short tubes. D.H Lieberman [5] studied the maximum dilution level for which detonation can still be initiated in test section using combustion products of stoichiometric propane air mixture in the driver section issued via an orifice. The schematic of the setup used for their experiments indicating the driver and test section is shown in Figure 1.3. They concluded that limits of detonation were relatively insensitive to driver chamber initial pressure (1-4 bar) and orifice diameter between (3-19 mm) since the nitrogen dilution level in the test section controlled the initiation of detonation in the test section. Similar work was conducted by Ungut and Shuff [21]. Tarzhanov [6]

investigated using hot detonation products to detonate stagnant propane-air mixtures and found that detonation initiation depends on the initial volume concentrations of mixture, mass fraction of hot detonation products, and the energy deposited from the detonation products.

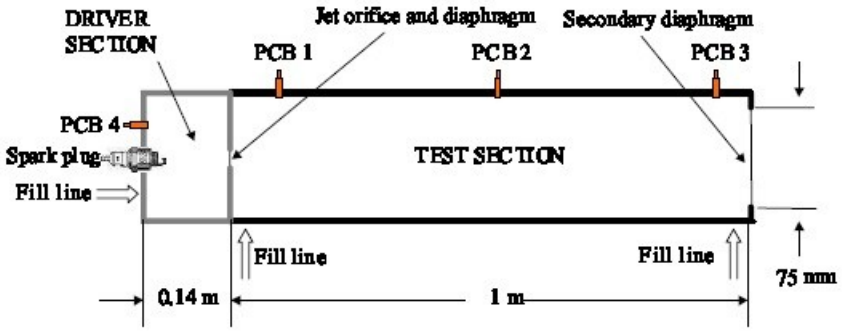

Figure 1. 3 Experiment setup of D.H Lieberman [5] to determine the effectiveness of hot jet ignition to initiate detonation

1.4 Applications Concerned with Accidental Jet Ignition

Studies on avoidance of ignition of hot jets have been carried out in order to understand the hot jet ignition in environments where accidental jet ignition by leaking hot gases needs to be prevented. Sadanandan [22, 23] focused on hot jet ignition process occurring within aviation engines from a safety perspective. Both pre-chamber and main chamber in their experimental configuration are closed cylindrical vessels connected by means of a nozzle. The optical windows in the main chamber along with OH-LIF (Laser Induced Fluorescence) equipment [22], NO-PLIF (LIF with seeded NO) [23] are used to study the re-ignition process of the hot jets in H2-air which was originally ignited in the pre-chamber using spark plug. Tsuji [24] performed analytical studies on ignition of aviation fuels and propellants by a laminar jet of hot gas. Boundary layer equations in aero thermochemistry for constant pressure was used in deriving the governing equations. Effect

of width and temperature of hot jet at the location of the ignition along the mixing region was studied.

Classical jet ignition studies on combustible mixtures by hot gases were studied in relation to safety in mines, where the majority of the research publications were from U.S. Bureau of Mines. These experiments were all conducted with non-reactive hot gas jet issued into a well-mixed quiescent combustible mixture. Wolfhard [25] studied the ignition process by continuous injection of hot gas in a cold explosive mixture, which revealed that the minimum hot-gas jet temperatures required bear little resemblance to spontaneous ignition methods. In fact some of mixtures studied revealed jet temperatures close to limit flame temperatures of the gases used. Nitrogen and carbon dioxide jets have similar minimum jet temperatures, while argon and helium have higher temperatures, respectively. Fink and Vanpee [26] developed an overall rate for describing the ignition of fuel-air mixtures at relatively low velocities by a hot inert gas for methane, ethane and ethylene. Flame jet ignition studies conducted by Mayinger [27] involved study of ignition initiated either by transmission of turbulent flame through or by reacting hot gas jets(flame quenched in this case) depending upon the diameter of the nozzle. The study focused on determining the critical orifice diameter such that ignition in the main chamber fails to occur and several correlations were derived. The main chamber is not quiescent but there exists an induced turbulence and when turbulence intensity exceeds a certain threshold level, ignition ceases.

1.5 Applications in Lean Burn IC Engines

Jet ignition applications on IC engines have a long history and contains several documented studies. Around 1950 studies were conducted at USSR Academy of Sciences Institute of Chemical Physics under the guidance of N.N Semnov leading to development of Lavinnai Aktyvatsia Gorenia (LAG) or avalanche-activated combustion by Gussak [28]. The goal was to develop engines operating without knock at relatively high compression ratio, using gasoline of an octane number around 70. It was Gussak's extensive study that

revealed the importance of active radicals in the jet ignition process. The engine was mass produced and it provided service for decades. Gussak's LAG engine has been often confused with the Honda CVCC (Compound Vortex Controlled combustion) [29], though falls in the category of pre-chamber divided chamber engines however there exists a fundamental difference between two. In the Honda case, a turbulent flame emerges out of pre-chamber and propagates without interruption into the cylinder. In the LAG and other systems to be discussed below, combustion is extinguished by shear at the exit of the orifice. The LAG engine, like the CVCC has been eventually aborted due to troublesome three-valve mechanism and the consequent lack of flexibility.

Ignition enhancement involves increasing the ignition energy in order to improve the burning characteristics of the fuel. Lean burn engines generally require high ignition energy, long duration of ignition and a wide dispersion of ignition source in order to achieve fast burn rates. Initiating combustion at multiple sites is especially important in increasing burn rates due to low flame velocities that occur in lean mixtures. Combustion initiation in pre-chamber cavities in SI engines began in first part of twentieth century with 2-stroke Ricardo dolphin engine [30]. Torch cell engine design evolved in an effort to simplify the design by removing the need for auxiliary pre-chamber fuelling. Unlike torch cells in divided chamber stratified engines there is an additional fuel source in the pre-chamber. Jet igniters are a subset of divided chamber stratified charge concept with notable differences of a much smaller orifices connecting the main chamber and pre-chamber combustion cavities [10]. The smaller orifice size causes the burning mixture to travel quickly through the orifice which extinguishes the flame and seeds the main chamber with active radicals that reignite some distance away from the pre-chamber. To avoid jet impinging on the main chamber wall the pre-chamber volume has to be kept minimal. Similar to homogeneous charge compression ignition (HCCI) with jet ignition chemical kinetics plays a larger role in determining combustion.

Oppenheim [2, 31] developed a pre-chamber system called Pulsed Jet Combustor (PJC) which is a miniaturized version of the valve operated pre-chamber of Gussak. PJC

was twice as fast when compared with a Spark ignition system. It was determined that if the orifice diameter is too small, the jet penetrates with such high velocity that it cannot ignite the lean mixture due to excessive velocity gradient. Maxson [32] showed that PJC process consists of three stages: the jet, the plume and the puff. The first is the formation of a jet plume, a purely fluid mechanical process devoid of the exothermic effects of chemical reaction. The plume is the most active stage of the system where vigorous combustion of entrained charge takes place within the large-scale vortex structures of a turbulent field. The puff is a turbulent cloud of products surrounded by a flame front. The PJC fitting can be accommodated in a 14 mm ignition plug and the pre-chamber is 0.5 mm^3 in volume. Tests results were published for single orifice and triple orifice configurations. The minimum nozzle diameter at which PJC would operate satisfactorily was found to be 2.5 mm.

In the 1990's, Hydrogen Assisted Jet Ignition (HAJI) system was developed by Watson at the university of Melbourne [33, 34]. In the HAJI process a small amount of hydrogen (2% of main fuel energy) was injected next to the pre-chamber so that a rich mixture is formed which is ignited by a spark plug [33] or glow plug [34]. Although HAJI equipped engine had higher thermal efficiency, lower CO and NOx emissions but recorded 3.5 times higher unburned HC emissions than spark ignition engines at all load points. The pre-chamber design and its placement over the cylinder head is shown in Figure 1.4. A further application of flame jet ignition has been in controlling the ignition timing of HCCI engines [35]. During this study since the mixture was leaner than the lean flammability limit, flame propagation from jet did not occur and instead the jet homogeneously ignited following the initial jet penetration.

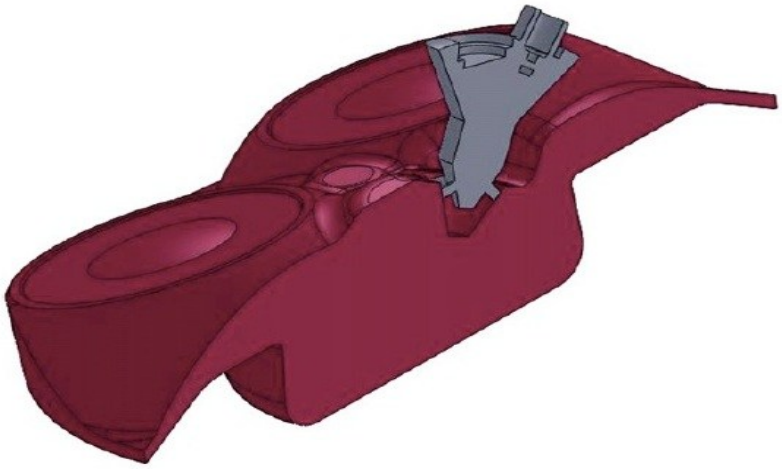

Figure 1. 4 Plane cut of the in-cylinder and pre-chamber indicating placement of volumes of respective chambers [34]

Attard at Mahle Powertrain [36] and Toulson [37] at Michigan State University continued working on TJI till date with a pre-chamber design very similar to one used by Boretti. Borreti's works [34] was directed towards using hydrogen as pre-chamber fuel while Toulson and Attard explored numerous alternative hydrocarbon fuels such as propane and natural gas as pre-chamber fuels. By using a conventional direct injector for the pre-chamber they were able to reliably ignite lean main chamber mixtures and maintained less combustion variability across cycles. The term Turbulent Jet Ignition (TJI) was used to refer the pre-chamber ignition. Attard's recent work focused on operating TJI engine with gasoline leaner than an equivalence ratio of 0.5. Net indicated engine thermal efficiency of 42% was achieved along with NOx emission below 10 parts per million (ppm) while using propane as pre-chamber fuel and gasoline as main chamber fuel.

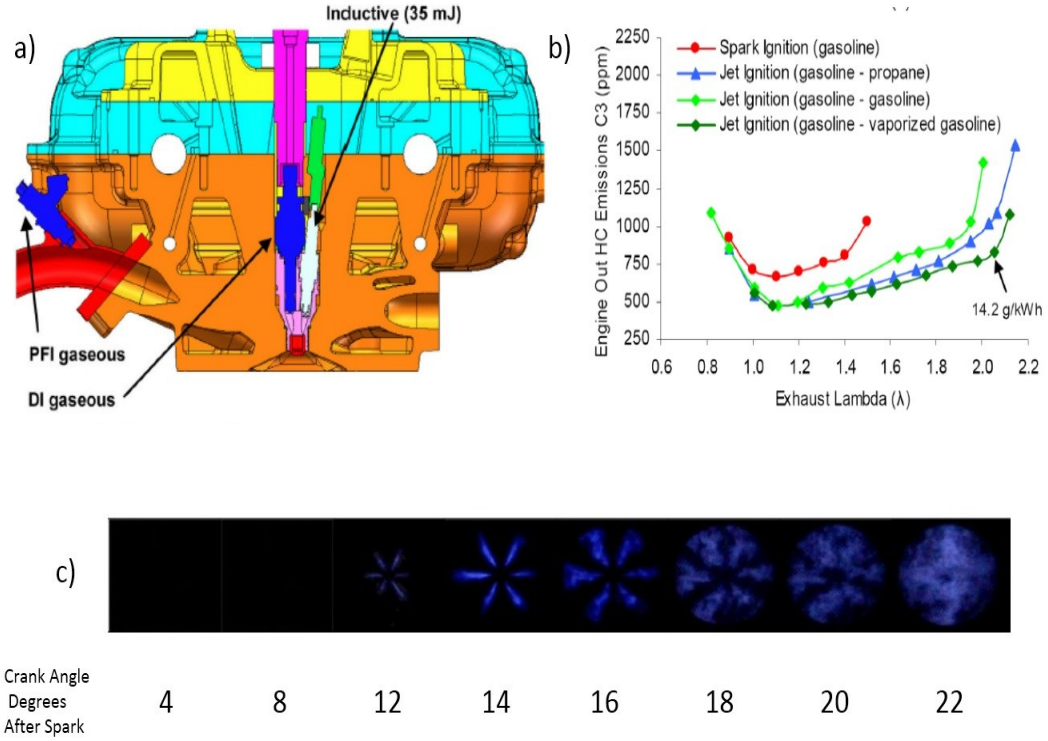

Figure 1. 5 a) Placement of pre-chamber cavity and location of supporting hardware on a cylinder head b) Unburned hydrocarbon emissions (UHC) with different pre-chamber fuel [38] c) Optical visualization of gasoline combustion ignited by turbulent jets issued from pre- chamber (as viewed from bottom of the piston) [39]

Although Kyaw and Watson [40] recognized that gasoline is not an effective pre-chamber fuel due to its narrow flammability limits, Attard [36] investigated gasoline (both in liquid and vaporized form) injected pre-chamber designs to make the TJI technology feasible for passenger vehicle application. Figure 1.5 b indicates the ranges of lambda (inverse of equivalence ratio) possible attained for different pre-chamber fuels in comparison with a spark-ignited engine. It has to be noted that the performance figures for the vaporized gasoline case was higher than the liquid fueled case due to poor mixture preparation in the small pre-chamber.

1.6 Objective of the Current Work

The objective of the current work is to gain insight into the translating hot jet ignition process as observed on the CVC rig and to establish guidelines and limits for future experimental and numerical work. The complex ignition behavior of this vortex controlled combustion process is highlighted by using high-speed images and supporting pressure traces. The current work is continued from experimental procedures and results established by Perera's [15] work on stationary hot jet ignition experiments which were further modified and adapted for translating jet experiments. The initial part of the study (as described in Chapter 2 and Chapter 3) aimed at establishing experimental methodology that can be used to run and record data from the CVC rig with minimum and controllable variation across tests in a configuration where the nozzle was traversing across the main chamber at different speeds.

Ignition behavior study across different fuel types was accomplished by studying two base hydrocarbon fuels, methane and ethylene, representing a wide difference in terms of ignitability and ignition delay limits. A fuel blend of hydrogen and methane (CH_4-60% and H_2-40%) was also studied. Partially combusted products of ethylene is the source of hot gas in the translating under-expanded high-speed jet. The main chamber fuel was kept the lean range and maintained at atmospheric pressure and room temperature respectively throughout the study.

1.7 Chapter Contents

Chapter 1 started with literature review, applications and background for the hot-jet ignition process. In Chapter 2, both numerical and experimental work that has been carried out in the other studies to understand the hot-jet ignition process occurring in a CVC have been discussed in detail with illustration on key results. These results have provided several insights and served as a guideline for this current study. In Chapter 3, the experimental setup at CPRL, IUPUI is discussed along with detailed procedure for conducting the experiments. Chapter 4 discusses the various events observed in the

experiments with their assigned definitions. The chapter also includes the preliminary experiments that were conducted to define and measure these experimental events. Chapter 5 illustrates and discusses on the results obtained by observing the ignition behavior for different main chamber fuels and their corresponding equivalence ratio. The hot jet is traversed at five different speeds and ignition is analyzed using high-speed images and pressure traces. The conclusions, future scope of the work and the recommendations are described at the end of the thesis.

2. PRIOR RESEARCH ON WRCVC AND HOT-JET IGNITION CVC RIG

Key points on prior research conducted in the CVC rig and WRCVC rig were discussed in the previous chapter. These prior works have provided several insights and understanding on the stationary and traversing hot-jet ignition process occurring in the CVC. These studies served as guidelines and provided motivation for the current work. Discussions regarding the traversing hot-jet ignition process will be made in the following chapters using the results obtained from these studies. This chapter covers both the experimental and numerical work illustrating methodology and key results.

2.1 WRCVC Rig

A wave rotor constant volume combustor was designed, built and successfully tested as a collaborative work between Rolls-Royce North America, IUPUI, and Purdue University (Figure 2.1). The rig includes the inlet, exhaust, rotor, seal plates, ignition source, fuel injectors and the electrical motor. The WRCVC used ethylene as the fuel due to its low ignition delay times. The inlet port contains 15 fuel injectors in the circumferential direction. The fuel distribution is controlled by the number and location of active fuel injectors. The rotor consisted of 20 circumferentially located combustion channel at a radius of 9 inches. Selected combustion channels were instrumented with thermocouples, pressure transducers, and ion probes along the flow path.

Initial tests were conducted in 2009 to investigate operational characteristics of the combustor. Successful combustion was achieved at multiple test conditions enabling to assess the effects of fuel-air ratio, and the level of combustible mixture stratification on combustor performance. Pressure response from an experiment for case 1 is shown against

numerical predictions by Elharis [41]. Case 1 corresponded to WRCVC rig operation with an overall equivalence ratio of 1.46 with a recorded rotation speed of 2078 RPM. Pressure transducers P2, P3 and P5 were in channel number sixteen while P10 was in channel number six.

2.2 Numerical Simulation of Traversing Jets in a WRCVC Channel

Numerical simulations performed by Wijeyakulasuriya [13, 17, 42, 43] focused on understanding the behavior and mixing process of translating jets in a confined channel. Such applications exist in a WRCVC where there is a relative motion between the jet and a channel at the time of pilot-fuel injection and during hot-gas injection [13]. The following discussion will be focused on jet dynamics as captured from the two-dimensional numerical simulations where the sweeping motion of a hot-gas injector relative to the confined channel is studied. In Figure 2.3 the injector is seen to slide past a channel in the WRCVC channel frame of reference. The hatched plane shown in Figure 2.3 is considered for the two-dimensional numerical simulations.

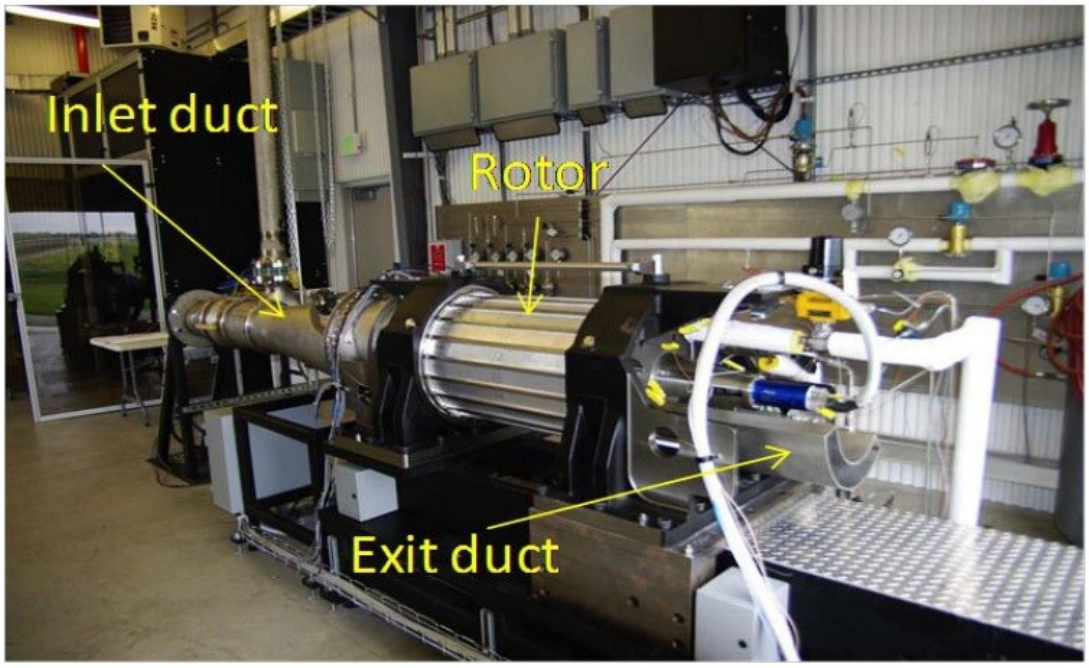

Figure 2. 1 WRCVC test rig [44]

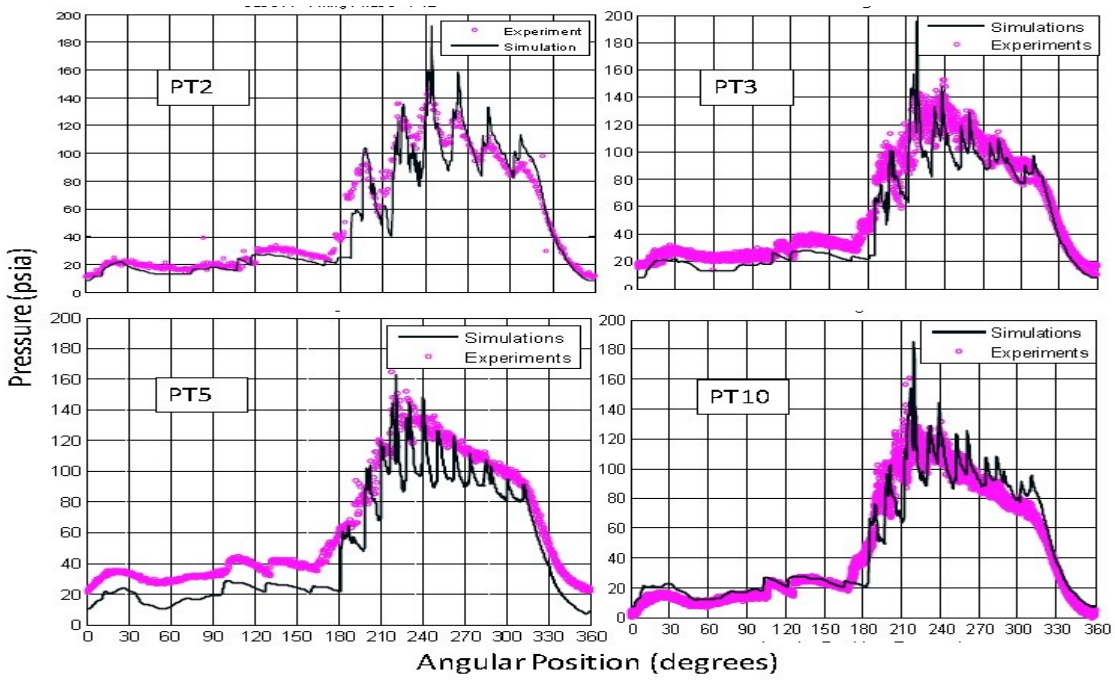

Figure 2. 2 Experimental and numerical pressure traces of case 1 along the combustion channel. The experimental pressure traces plotted were that of 5 consecutive cycles except in PT2, which is for a single cycle to better illustrate the pressure waves [41]

2.2.1 Numerical Model

Numerical simulations for the study were carried out using Star-CD CFD code with sliding mesh arrangement. Turbulence modelling was handled by Star-CD high Reynolds number k-ε method [45]. Combustion was not modelled in the study since the primary focus was on investigating the mixing behavior of the jets with a gas at a different density. Three WRCVC channels were modeled, together with the hot-gas injector nozzle which moves relative to the channels. The length of the WRCVC channel was 774.7 mm (30.5 inches) while the channel width was 63.5 mm (2.5 inches). The rotation speed on the rotor was 2200 rpm. This corresponds to dimensions of a WRCVC test rig constructed at operated at Purdue University Zucrow Laboratories [44] Figure 2.1.

2.2.2 Traversing Jet Vortex Dynamic Behavior

Based on the results from two-dimensional numerical study several key features with regard to traversing jet flow dynamics and mixing process were understood [43]. Jet injection in a WRCVC channel is determined by a complex vortex mixing process, affected by the traversing motion and presence of walls. A qualitative comparison of two simulations illustrating fuel jet injection in a channel is shown in Figure 2.4. Mass flow rate, injection pressure and injector are kept the same for these simulations except for translation of the injector. Fuel is distributed over the combustion channel width near the injector region due to the traverse injection. The axial jet penetration of the translating jet is not very different from the stationary jet along the mid-section of the channel. The traverse penetration is enhanced by the translating jet.

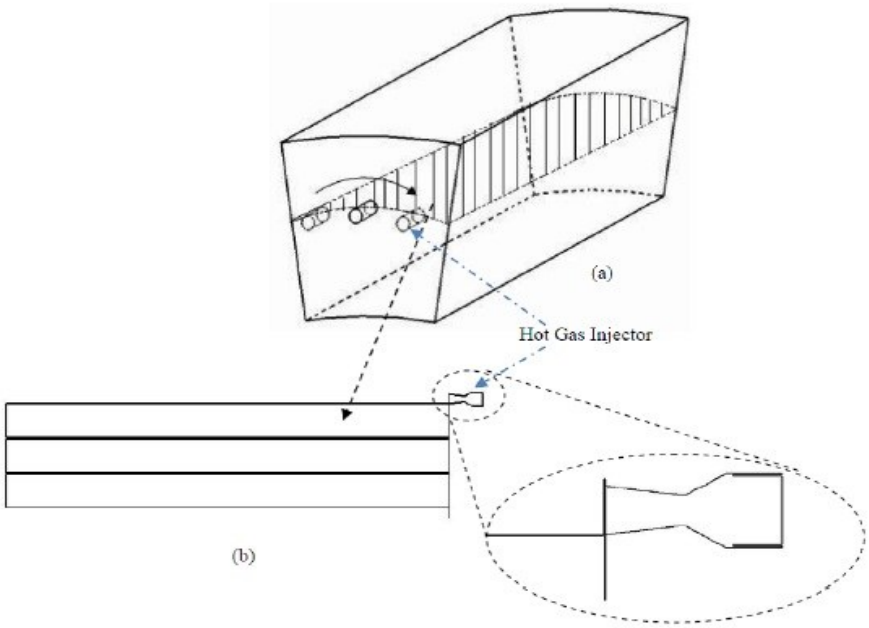

Figure 2. 3 (a) Relative motion of a traversing hot-gas injector in a single WRCVC channel (2D numerical simulations were carried over the hatched plane) (b) 2D representation of the traversing injector (three WRCVC channels are shown) [43]

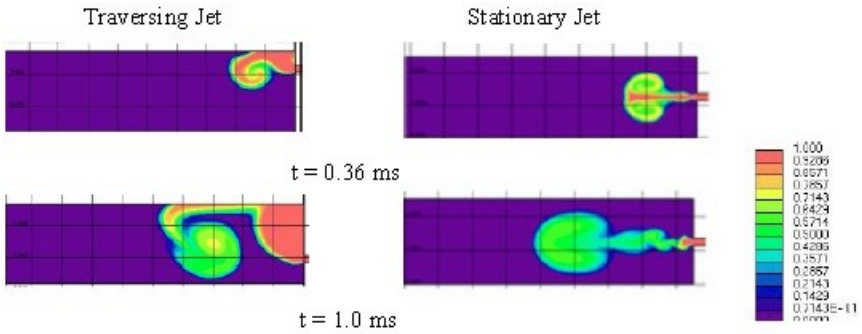

Figure 2. 4 Behavior of a traversing and stationary planar fuel jets [17]

Sketches on Figure 2.5 illustrates the behavior of the main vortices that controls the mixing and ignition in a WRCVC channel. The development of these vortices are strongly influenced by the injection parameters such as nozzle geometry, nozzle position, injection pressure and by the geometry of the channel. It had to be recognized that the dimensions of the channel in the WRCVC is significantly larger compared to the main chamber of the hot–jet ignition CVC rig. It must also be recognized that the onset of

ignition and combustion may result in significantly different flow dynamics than what was learned from simulations of a non-reacting traversing jet.

In Figure 2.5 stream S1 initially feeds two counter rotating vortices labelled as V1 and V2, the inclination being dictated by the path of least resistance. The jet can be later seen to impinge the lower wall and there is a production of a third vortex V3 which is fed by the stream S2. Even after reaching the lower wall, the vortices V1 and V2 are still being fed by the incoming stream S1. Stream S1 is later terminated by the upward movement of the vortex V1 and hence V3 is the only vortex now being fed by the incoming jet. There are also several small scale vortices that are developed and shed during this process which are not shown in these representations. These vortices dictate the formation of ignition location in the channel as it helps to entraps unburned fuel-air mixture in its cores and increase the localized temperature. Interpretation of these vortices will help in understanding the results in this current experimental study since vortex evolution process is not captured with the current optical arrangement. Nonetheless the ignition pattern and observed ignition sites can be easily connected using this illustrated vortex dynamic interactions.

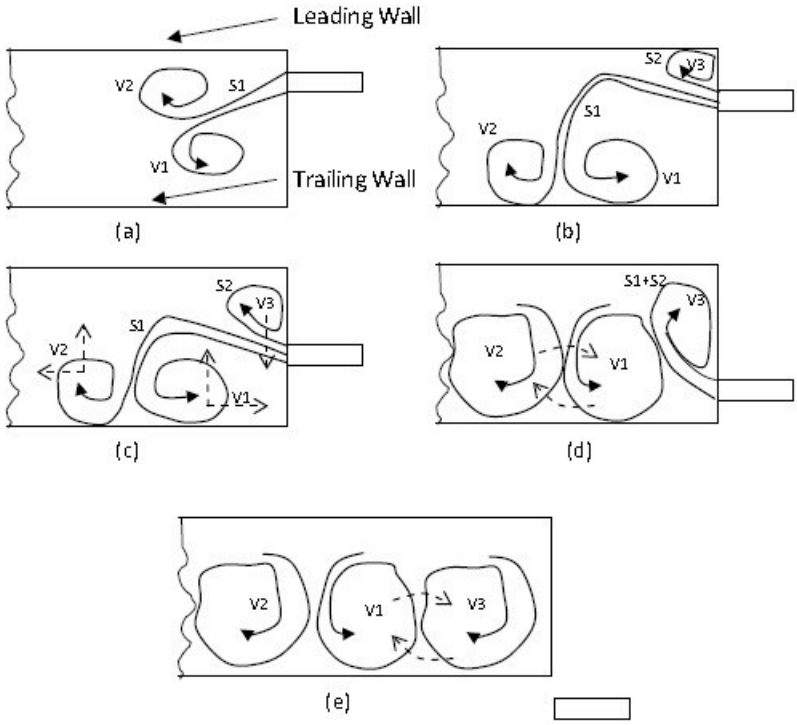

Figure 2. 5 Interaction between the main vortices in a WRCVC channel [43]

2.2.3 Vortex Evolution with Hot-Gas Injection

Figure 2.6 illustrates the temporal development of the injected mass fraction in a 2D simulation of a WRCVC channel. The converging-diverging nozzle injects hot nitrogen gas into atmospheric air thereby injecting lighter gas into heavier gas. The vortices V1 and V2 develops during the earlier injection process and grows along the path of least resistance. When the jet reaches the mid-plane, vortex V3 starts to develop. The interactions between these main vortices and shedding of several small scale vortices can also be seen. Three WRCVC channels were considered in the computational domain for the study. An actual WRCVC will have more channels. A fundamental difference between penetration behavior of stationary and traversing fuel jets is illustrated in Figure 2.4. Wijeyakulasuriya [43] concluded that width of the nozzle relative to the channel dimension was a key parameter in controlling mixing dynamics, while injection pressure was not as important.

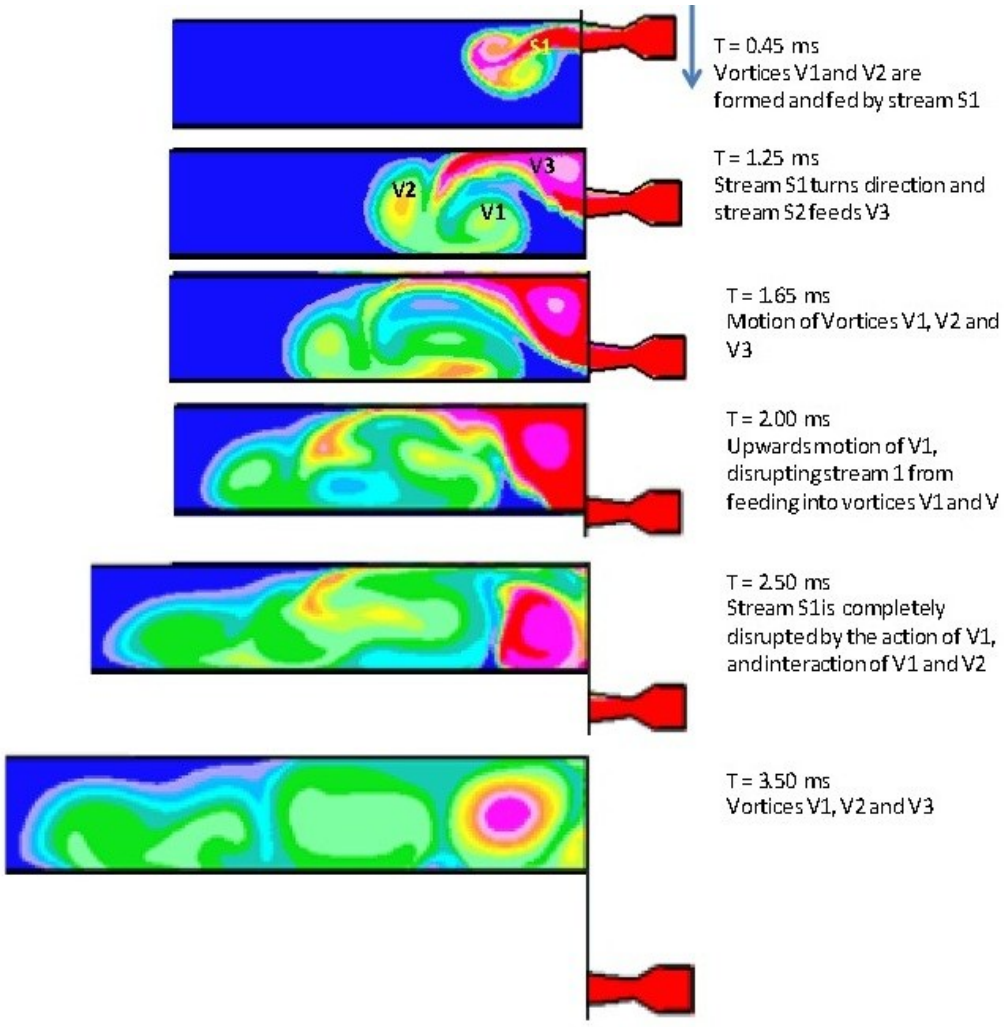

Figure 2. 6 Evolution of vortices from the hot-gas jet and its interaction in a WRCVC channel [13]

2.3 Experimental Study on Hot-Jet Ignition CVC Rig at the University of Washington

In 1998, using a prior version of the CVC rig, Bilgin [16] investigated the jet ignition process at the University of Washington in support of pressure-wave machines. Two pre-chambers, one with an internal volume of 2.6×10^{-3} m^3, and another with internal volume of 8.4×10^{-4} m^3 were used. Both the stationary and traversing hot-jet ignition process was explored to understand the limiting factors on ignition success in the main chamber fuel-air mixture. Video imaging was made using S-VHS video camera at 30 frames per second (fps) and a high-speed camera (up to 500fps) with 16mm film. Pressure history was recorded with dynamic piezoelectric transducers. The nozzles that were used to inject the hot-jet were of converging-diverging type. The 2 millisecond interval between video image frames does not allow for many details of the initial jet entrance, traverse, or ignition to be observed. Therefore many conclusions drawn by Bilgin are based on observations of the combustion process after initial ignition.

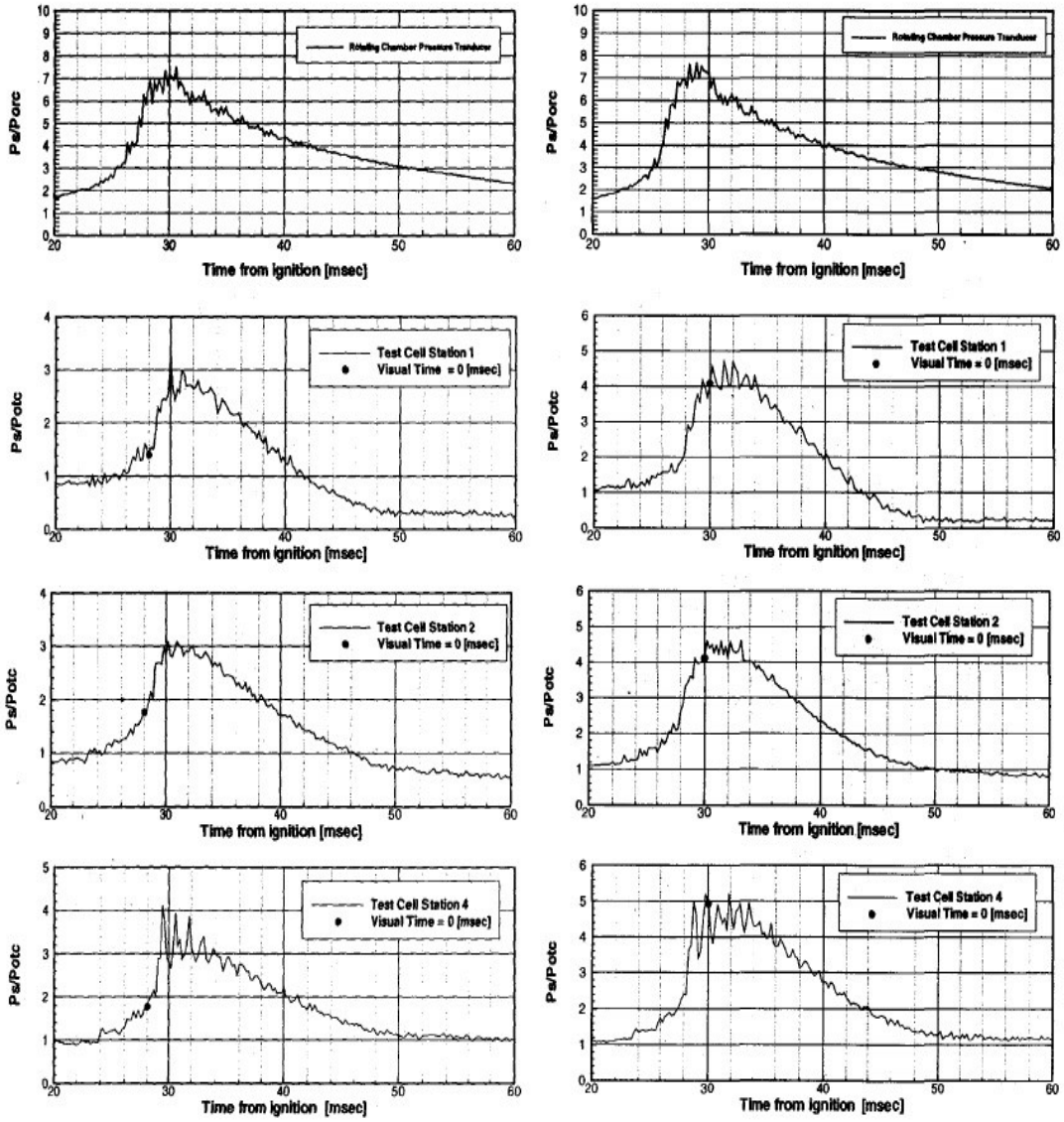

Figure 2. 7 A sample plot of the pressure traces at four locations in the test cell [16]

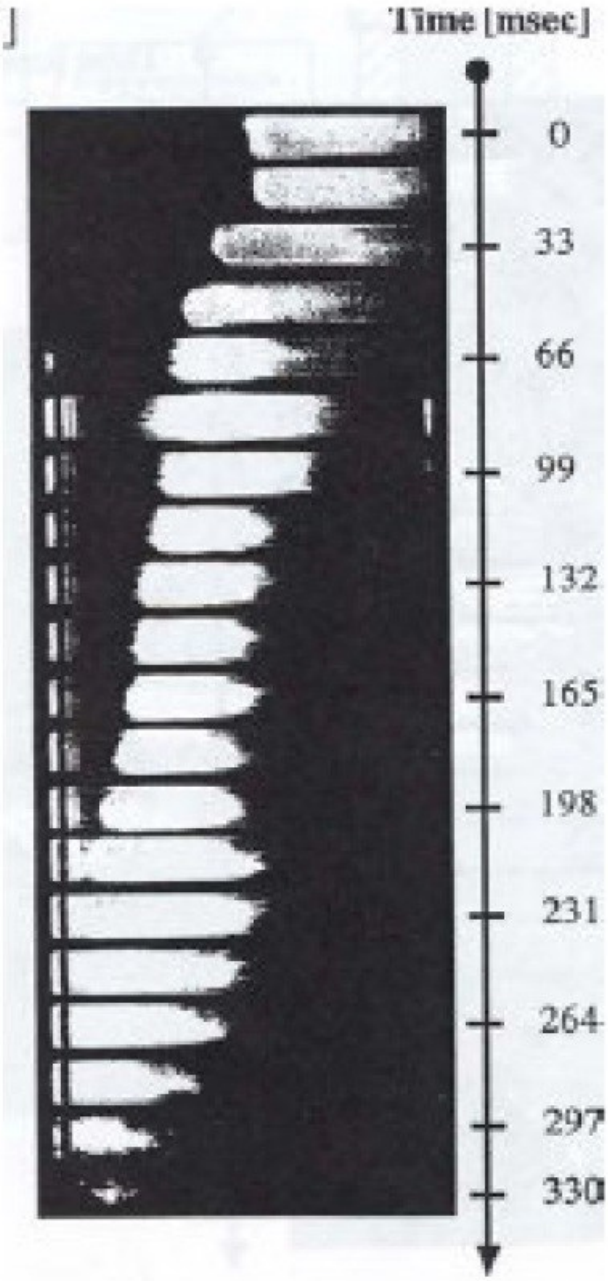

Figure 2. 8 Reported flame propagation inside the channel corresponding to the pressure traces shown above [16]

In this study an attempt was made to measure and define ignition success in the CVC using suitable definitions for the Damkoehler number. Damkoehler number is defined as the ratio of the characteristic vortex rotation time to the chemical ignition delay time. Three different definitions of Damkoehler number were used in the study: Near-field Damkoehler number, Far-field Damkoehler number and Long-pulse Damkoehler number. Detailed formulation and derivation of these different forms of Damkoehler numbers along with the experimental parameters involved can be found in [16]

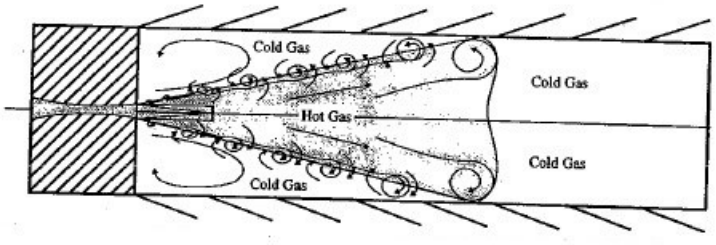

Figure 2. 9 Centered supersonic hot-jet mixing process in the CVC as illustrated by Bilgin [16]

The tested main chamber fuels included propane-air and ethane-air mixtures in varying equivalence ratios. The pre-chamber was fuelled with the same fuel type as used in main chamber and were maintained at either $\Phi = 1$ or 1.5. It was concluded that the far-field and long-pulse Damkoehler numbers were more suitable to predict ignition success for the stationary experiments. It was further realized that more experiments using a variety of mixtures, nozzle exit diameters, and jet injection pressures were needed to refine both far-field and long-pulse Damkoehler numbers and to provide a more precise number for transition between ignition and no ignition. For the traversing hot-jet study, the nozzle traverse time and nozzle flow rate were identified as two important parameters for ignition success. Bilgin [16] concluded that temperature of the jet had major impact on main chamber ignition compared to the effects of nozzle thrust.

2.4 Experimental Study on Ignition by a Stationary Hot-Jet

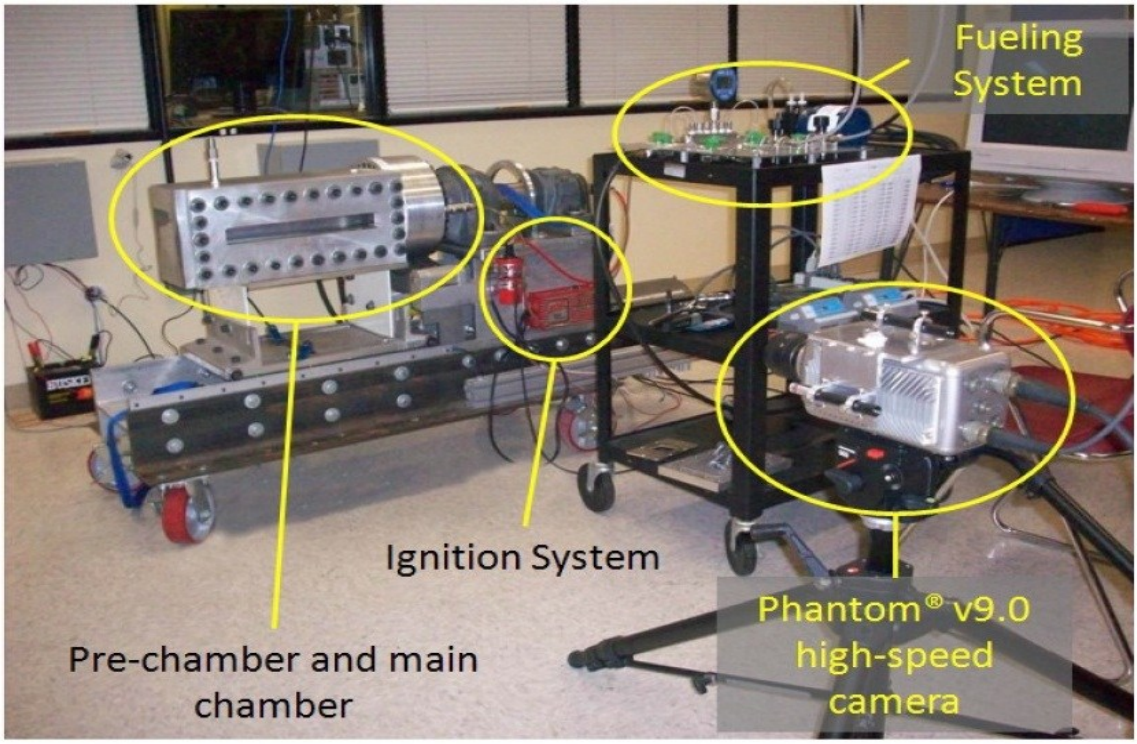

Figure 2. 10 Components in hot-jet ignition CVC rig as used by Perera [15]

The hot-jet ignition CVC rig used by Bilgin [16] was continued to be operated and studied by Perera [15] at IUPUI with modified combustion diagnostics and data acquisition system. The pre-chamber was set stationary and centered on the main chamber cross-section for the experiments. Parameters varied for the study included main chamber fuel and its equivalence ratio, pre-chamber fuel and its equivalence ratio and the pre-chamber nozzle type. Evaluation was made in terms of ignitability limits and ignition delay times with respect to main chamber fuel-air mixtures. Several definitions and experimental methodology used by Perera [15] have been carried over for the current study with suitable modifications made for the traversing jet configuration. Pressure-time history data for the pre-chamber was available due to the stationary pre-chamber arrangement. For the current traversing hot-jet ignition study, pressure measurement in the pre-chamber was not possible due to the rotation of the pre-chamber. Due to this reason the exact time at which the

diaphragm ruptured is not precisely known. Instead for the current study, diaphragm rupture is assumed to have occurred 0.2 ms prior to the first appearance of jet in the high-speed images. Hence it is considered that it took 0.2 ms for the hot-gas to travel from diaphragm at the nozzle entrance to the exit as observed from stationary experiments and numerical simulations.

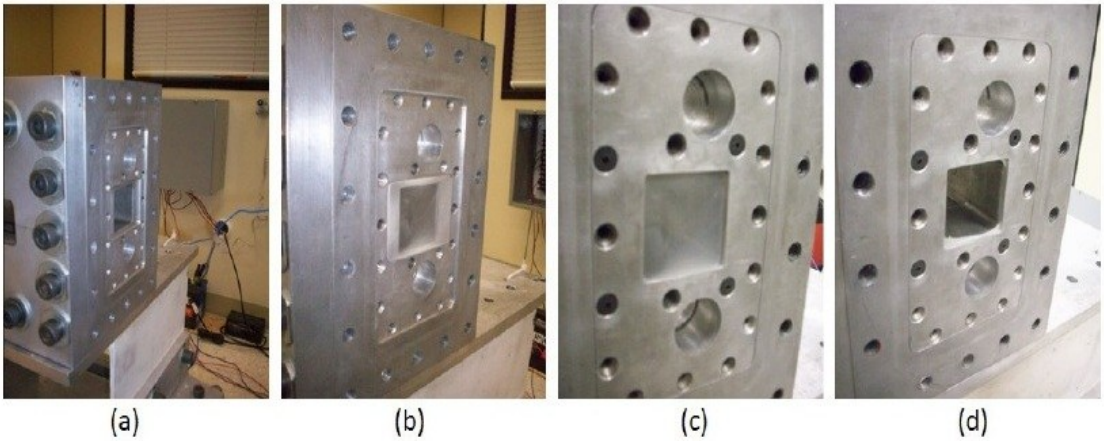

Figure 2. 11 Main chamber entrance and latex diaphragm assembly as used by Perera [15] (a) CVC rig showing main chamber entrance (b) main chamber entrance with diaphragm plate inserted and latex diaphragm stretched over it (c) after clamping the diaphragm backing plate over the diaphragm plate (d) diaphragm assembly after an experiment showing ruptured diaphragm.

Comparing Figure 2.10 with Figure 1.1 the difference between the previous main chamber assembly and the current assembly can be identified. The sealing method used to isolate main chamber mixture prior to the experiment was also different. As shown in Figure 2.11 the main chamber entrance was sealed with a latex diaphragm that was ruptured upon contact with the hot-jet during the experiment. For the present study a modified main chamber was used with a different sealing method. The internal dimensions and the volume of the combustion chamber is identical for both the main chamber designs. The initial conditions in the chambers before the experiments were maintained at atmospheric pressure and room temperature throughout the study.

Perera [15] explored the ignitability limits in the main chamber for rich and lean limits of ethylene-air, propane-air and methane-air mixtures. The pre-chamber diaphragm rupture time was evaluated by spark igniting the ethylene-air, methane-air and propane-air mixtures kept at an equivalence ratio of 1.1. Combustion of ethylene-air mixtures ruptured the pre-chamber diaphragms at a lowest recorded time of 14.4 ms while for the methane-air mixtures the diaphragm ruptured at 39.9 ms. The pressure at the moment of diaphragm rupture was in the range 51.2 to 54.7 psig which was recorded using the pressure transducer in the pre-chamber.

Different nozzle configurations used during this study to deliver the hot jet are documented in Table 2.1. Drawings and dimensions of these individual nozzles are presented in the Appendix. Nozzle types A-D are convergent nozzles while E-G were convergent-divergent nozzles. Figure 2.12 compares the ignition delay times for the main chamber mixtures obtained by using these different nozzle configurations. It was revealed that type A nozzle had the lowest ignition delay times. Figure 2.13 reveals the influence on ignition delay times for the main chamber mixtures due to varying pre-chamber equivalence ratios. Ethylene was used as fuel in the pre-chamber for all the cases with equivalence ratio varying from 0.6 to 1.5. The results indicate lowest ignition delay times were attained with $\Phi = 1.1$ at the pre-chamber across all fuels investigated in the main chamber. Hence nozzle type A with ethylene-air mixture at $\Phi = 1.1$ in the pre-chamber was used for conducting further experiments.

Table 2. 1 Different pre-chamber nozzle configurations tested by Perera [15]

Number	Nozzle	A_{exit}/A_{throat}	Exit Diameter d_e (in)	Throat Diameter d_e (in)
1	A	1.00	0.236	0.236
2	B	1.00	0.917	0.197
3	C	1.00	0.157	0.157
4	D	1.00	0.118	0.118
5	E	1.78	0.157	0.118
6	F	2.04	0.159	0.111
7	G	2.03	0.318	0.223

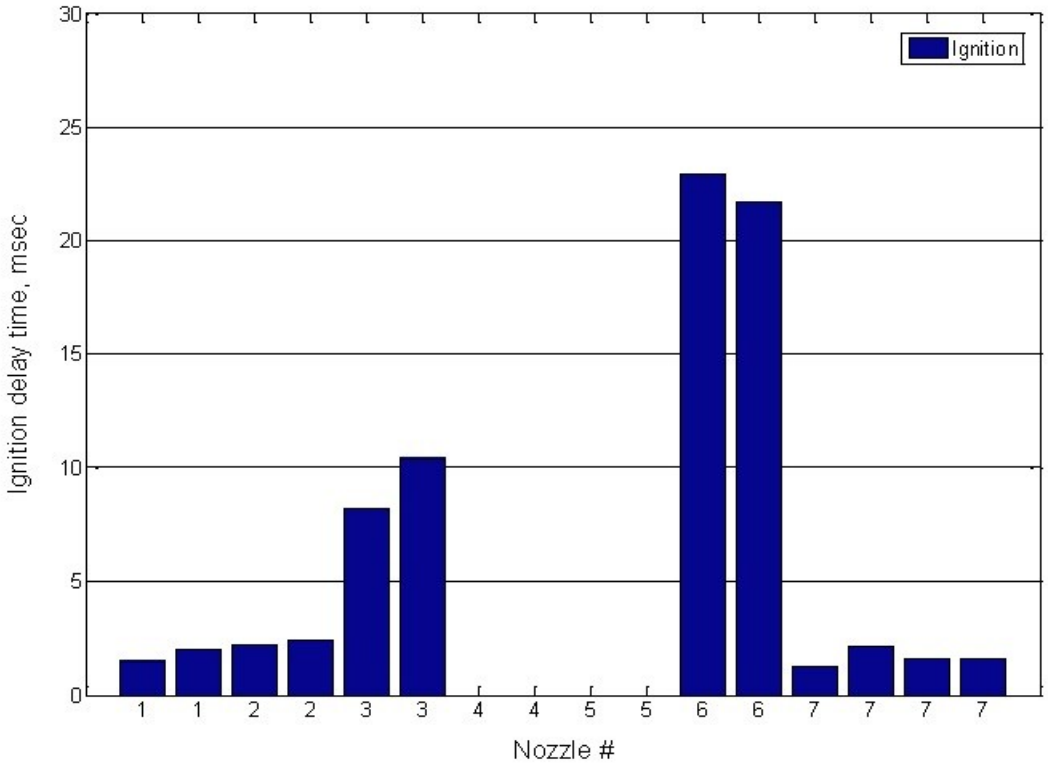

Figure 2. 12 Ignition delay time variation with different nozzles (Main Chamber: Ethylene-air mixture at Φ = 1.0, Pre-Chamber: Ethylene-air mixture at Φ = 1.1) [15]

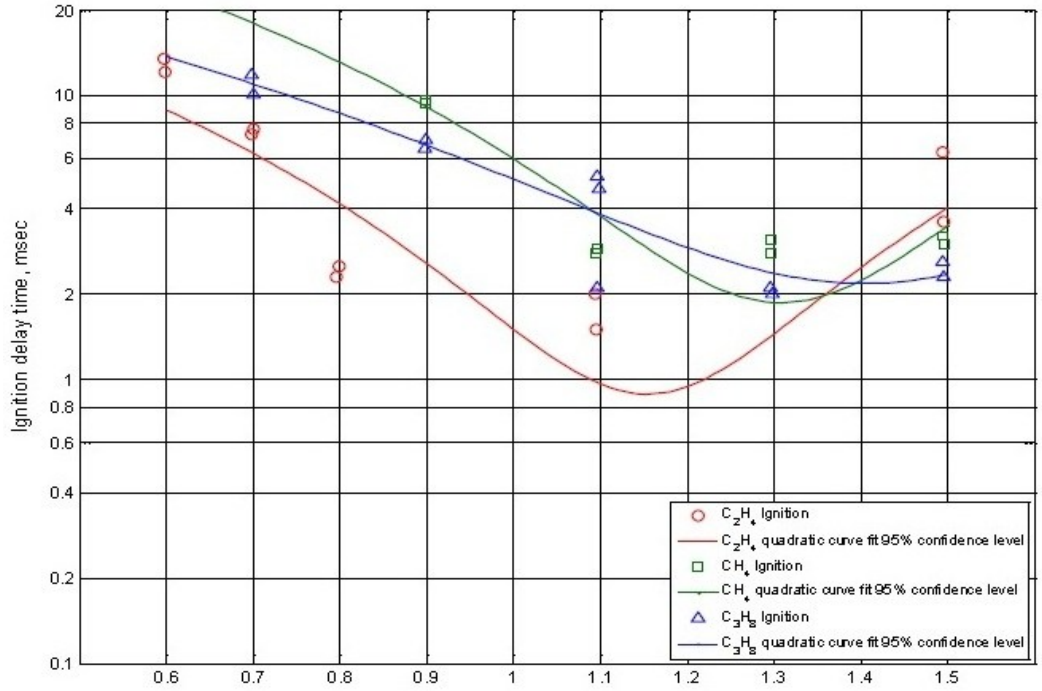

Figure 2. 13 Influence of pre-chamber equivalence ratio over ignition delay times in the main chamber [15]

The variation with type of fuel and equivalence ratio in the main chamber was also investigated. Ignition was recorded for ethylene-air mixtures with equivalence ratio in range of 0.4 to 2.4, indicating the rich and lean limits. Figure 2.14 indicates the ignition delay times for ethylene-air mixtures ignited by the stationary hot-jet. For methane-air mixtures, equivalence ratio was varied from 0.2 to 3.0 in the main chamber. Methane had the narrowest ignitability limits. Methane-air mixtures with equivalence ratios leaner than 0.4 and richer than 1.4 were not ignitable by the hot jet as observed in Figure 2.15. A comparison between three cases of methane combustion in the main chamber is shown in Figure 2.16 in the form of high-speed images. All these cases had similar initial conditions except for variation in ignition delay times.

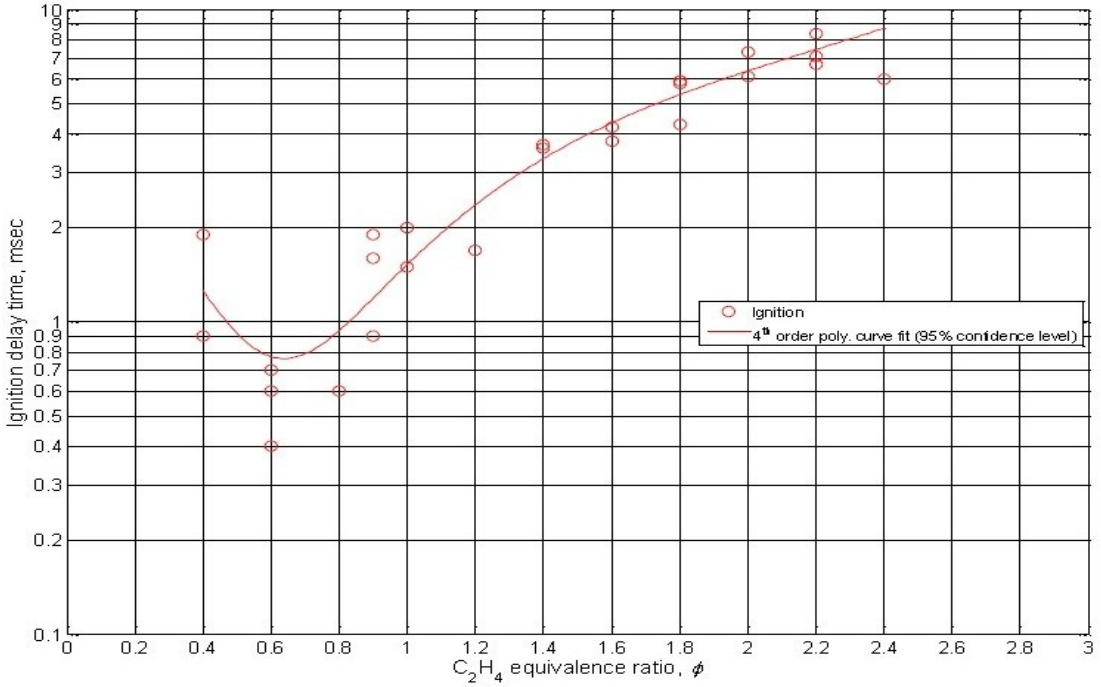

Figure 2. 14 Ignition delay times of different equivalence ratios of ethylene-air mixtures [15]

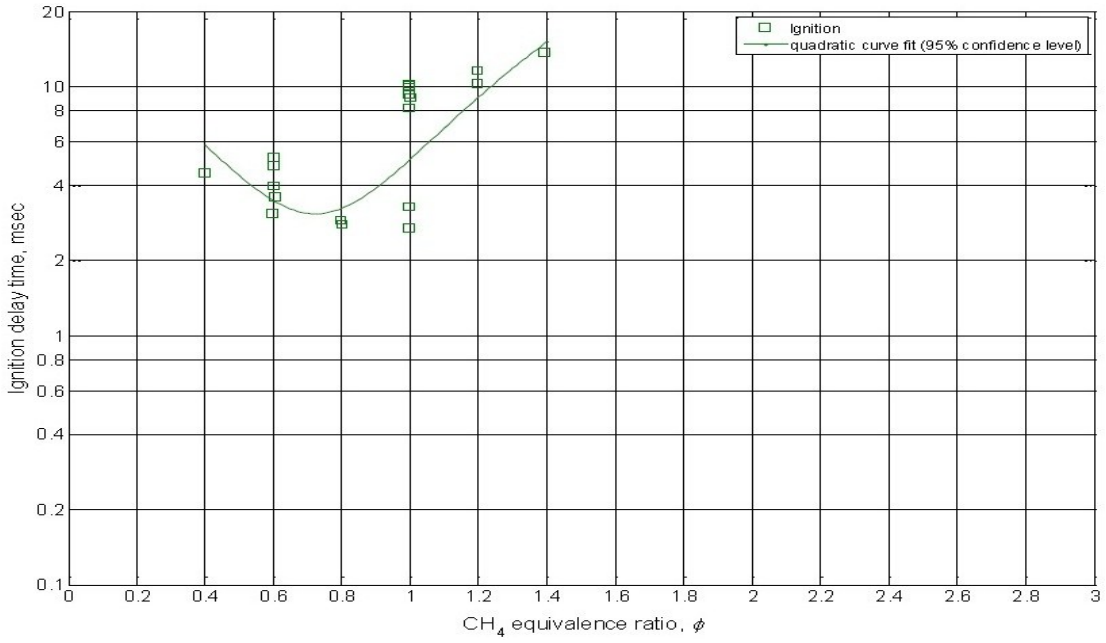

Figure 2. 15 Ignition delay times of different equivalence ratios for methane-air mixtures [15]

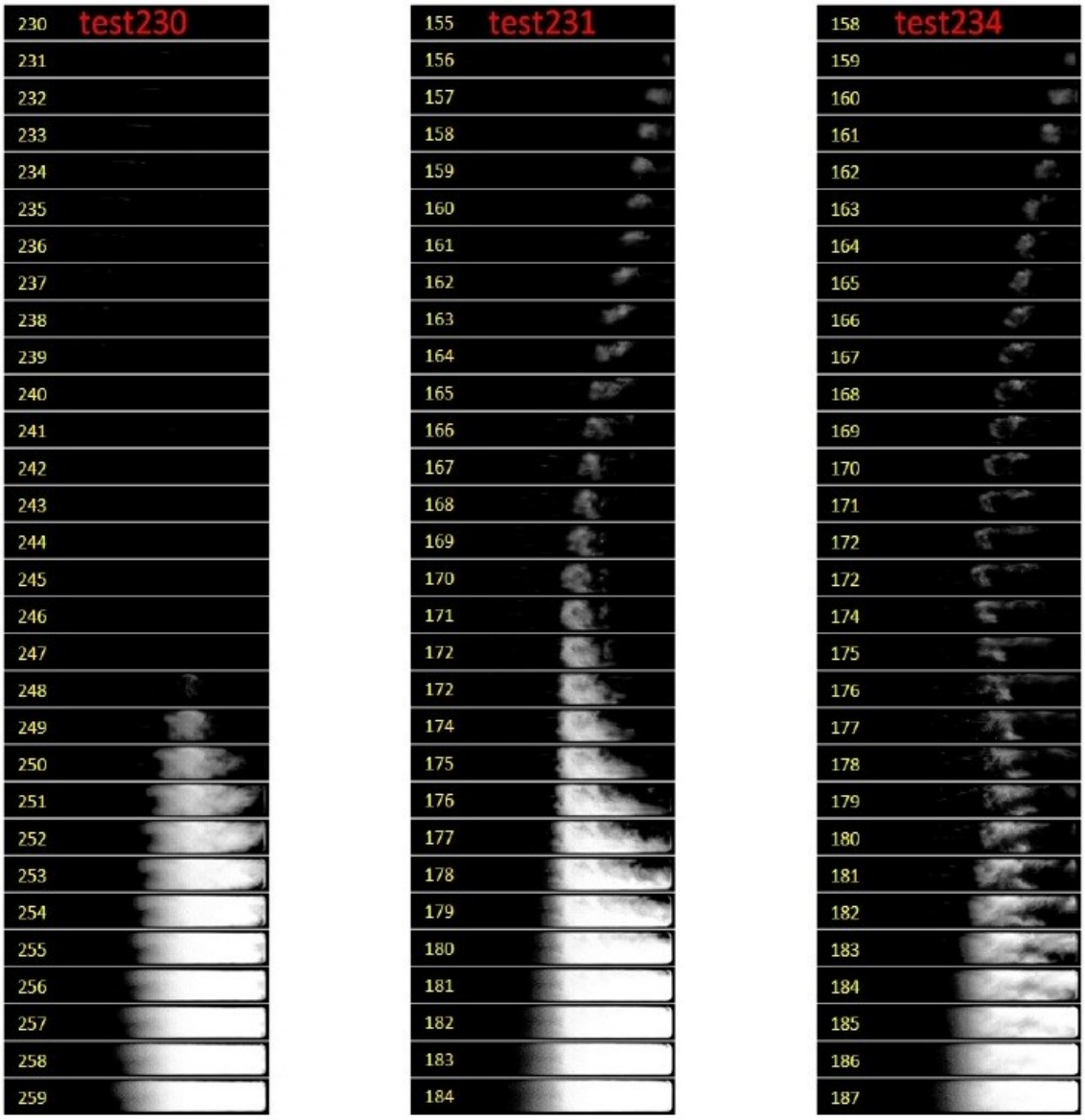

Figure 2. 16 High-speed images for Φ = 1 methane-air mixtures with pre-chamber Φ = 1.1 [15]

2.5 Numerical Modeling of Hot-Jet Ignition in the CVC Rig

2.5.1 Modeling of Stationary Hot-Jet Ignition in the CVC Rig

An early attempt towards numerical modelling of the hot-jet ignition process in the CVC rig was made by Baronia [19]. The computational fluid dynamics (CFD) code Star-CD was used for this study. Two-dimensional simulation was used due to computational time considerations Propane was considered as main chamber and pre-chamber fuel. The jet was kept stationary and axially aligned along the center of the chamber as maintained by Perera [15] for his experiments. Nozzle type G as specified in Table 2.1 is modelled in the domain to inject the hot-jet. At the start of computation, main chamber contains a stoichiometric propane-air mixture at room temperature. The pre-chamber contains the combusted rich propane-air mixture. Its initial temperature is determined from adiabatic flame temperature calculations while the initial pressure is obtained from experimental data. Hence it can be understood that spark-ignition process was not modelled in the pre-chamber and the simulation is initialized with conditions existing before the rupture of latex diaphragm in the main chamber entrance. The pre-chamber rich combusted mixture initial mass fractions are obtained by using water-gas shift reaction in conjunction with species mass balance.

For the initial part of the study the fuel oxidation process was represented by a single-step global reaction mechanism and the reaction rate was driven by a combined time scale model which assumes that reaction time is a sum of turbulence dissipation and chemical kinetics time scale. A multi-step reaction model considering up to four intermediate steps for propane oxidation was also investigated with reaction rate controlled by finite rate chemistry. Finally a hybrid model along with the four-step reaction mechanism was used for predictions. The hybrid model is capable of switching between finite rate chemistry calculation and combined time scale model based upon a user-defined threshold temperature. Two threshold temperatures of 1200 K and 1500 K were investigated.

Figure 2.17 compares the fuel mass fraction contour predictions at different time steps for propane oxidation with four step reaction mechanism and hybrid model with threshold temperature at 1200 K and 1500 K. Baronia [19] concluded that the results using a threshold temperature of 1200 K should give better predictions compared to 1500 K threshold since an average temperature of around 1300K is observed to exist at the mixing region of hot-jet and the fuel-air during which chemistry effects dominates. For 1500 K threshold temperature, the reaction is driven only by the combined-time-scale rate formulation which predicts a relatively uniform and increased consumption of the main chamber fuel.

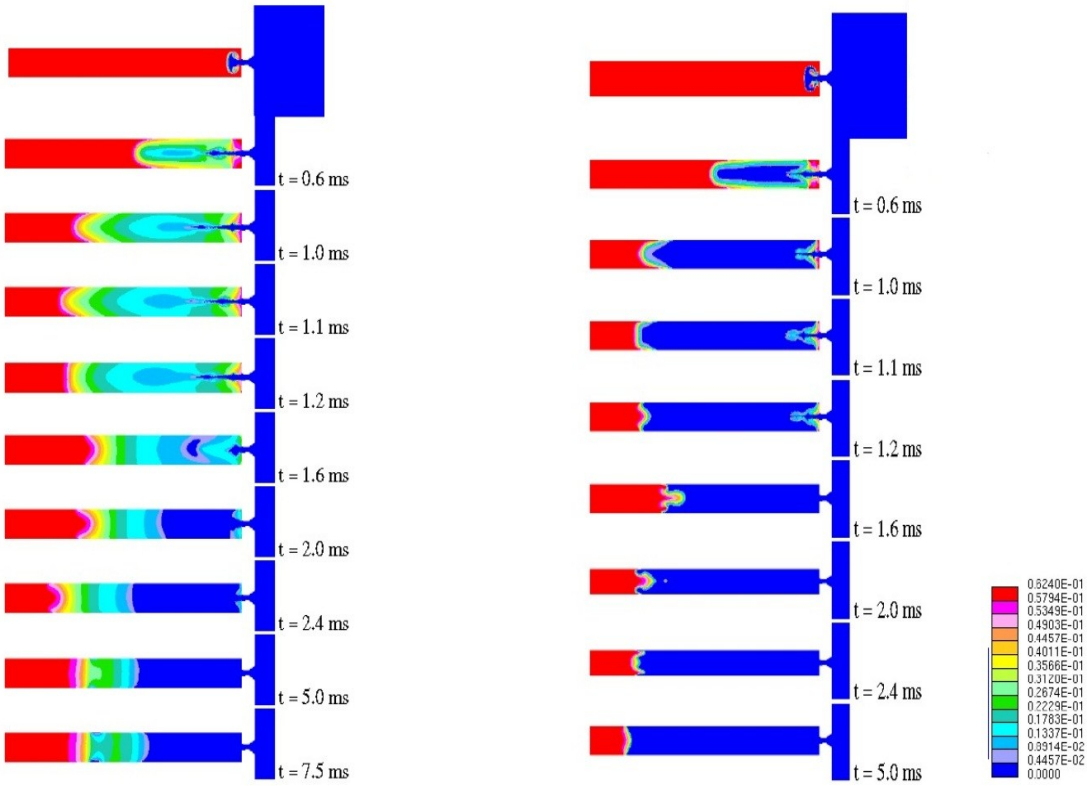

Figure 2. 17 Propane mass fraction contours predicted using hybrid reaction model with 1200 K threshold temperature (left) and 1500 K threshold temperature (right) [19]

2.5.2 Modelling of Traversing Hot-Jet Ignition in the CVC Rig

Karimi [20, 46, 47] modelled the combustion process for the CVC rig using the CFD code Star-CCM+ considering both stationary hot-jet and traversing hot-jet ignition. A two dimensional (2D) model of the combustor and jet were used to simulate the process. The hot-jet was issued by a converging nozzle (Type A) compared to a converging-diverging nozzle used by Baronia [19]. Spark-ignition and subsequent flame propagation inside the pre-chamber was not modelled. The simulation is initialized in such a way that the flow is driven by the initial pressure difference between the pre-chamber and the main CVC chamber at the instant when the diaphragm is broken. Stable species are considered in the pre-chamber domain at the start of the simulation with the initial temperature and composition obtained by chemical equilibrium calculations. Turbulence was modelled using the shear stress-transport (SST) two-equation k-ω model [48]. Combustion was modelled using a hybrid eddy-break-up (EBU) model that considers finite rate chemistry. The EBU model was presented by Spalding [49] and later developed by Magnussen and Hjertager [50]. The simulations employed detailed and skeletal reaction mechanisms to represent the fuel oxidation process.

[20] reports comparison between fuel consumption rate and intermediate species generation history for centered jet against jet traversing in a time of 40.6 ms (near-wall jet), 8.1ms and 3.1ms. Figure 2.18 indicates the temperature history during the combustion process across different nozzle traverse speeds. Penetration of the jet and progress of the combustion changes with change in traverse speed and position of the nozzle. The slow traverse jet was initially observed to behave as a wall jet and later as a wall-impinging jet. Discussions were made based on identifying suitable trends in fuel consumption rate and intermediate species profiles to be used as markers for quantifying ignition delay times. [46] A comparison was made in terms of reactivity of jet consisting of stable species and another radical-laden jet containing intermediate species from partial combustion. Radical species were initialized in the pre-chamber by calculating the composition in a separate kinetics code using a detailed reaction mechanism as input. The fuel consumption rate comparison between these two jets is shown in Figure 2.19. In the study [46], the jet was modelled as a stationary centered jet.

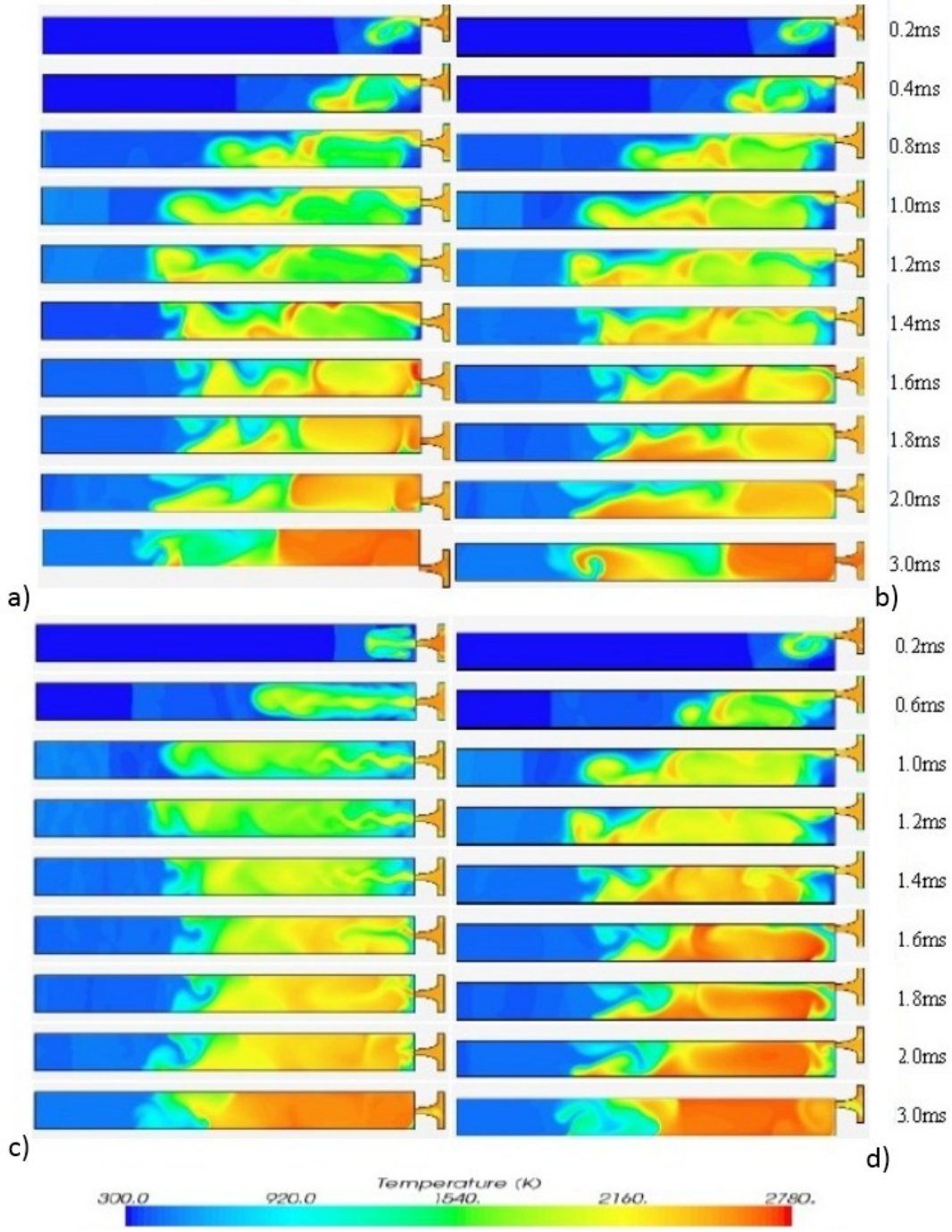

Figure 2. 18 Temperature contour plots for methane-air mixture at Φ = 1(a) 3.1 ms nozzle traverse (b) 8.1 ms nozzle traverse (c) centered stationary jet (d) 40.6 ms nozzle traverse [20]

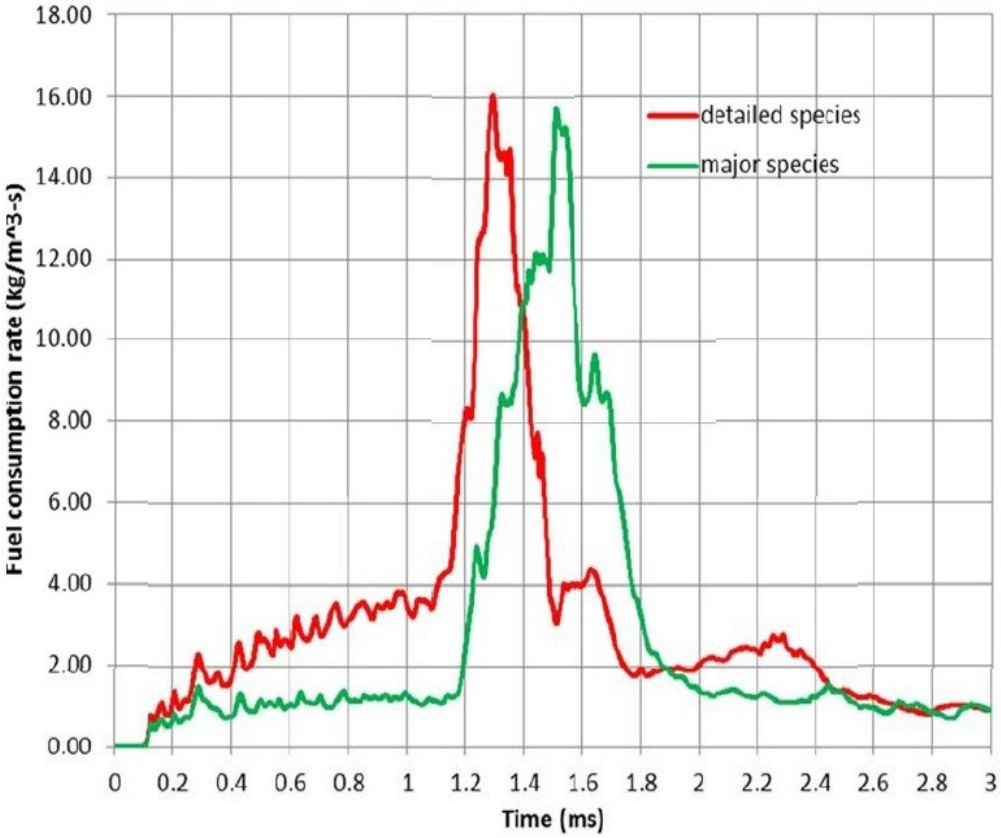

Figure 2. 19 Comparison between main chamber fuel consumption rate for stationary hot-gas jet with stable species and radical species [46]

3. EXPERIMENTAL SETUP AND PROCEDURE

A prior version of the hot-jet ignition CVC rig was originally built at the University of Washington by Bilgin [16] with financial support from National Aeronautics and Space Administration (NASA) Lewis Research Center. The rig is capable of reproducing the translating motion of a gas injector relative to confined ambient gas in a rectangular channel as seen in a wave rotor combustor. The rig was later re-installed and operated at Indiana University Purdue University Indianapolis (IUPUI). In 2009, Perera studied the ignition characteristics of a stationary hot jet issued through various nozzle geometries. For the current study, several modifications were made to the original rig including a complete redesign and rebuild of major assemblies by Murphy [51]. New capabilities were added which allowed the author to study the translating hot jet ignition process at higher traverse speeds [52].

3.1 Experimental Facility

The CVC rig has two main sub-assemblies, the pre-chamber and the main chamber. The main chamber is stationary while pre-chamber can be rotated. For the current study, the pre-chamber rotation speed has been varied from 150 rpm to 1500 rpm. Figure 3.1 illustrates the layout of the experimental facility at IUPUI. Each component and its functionality will be discussed in this chapter. Detailed experimental procedures and operations on individual systems will be discussed in the Section 3.2.

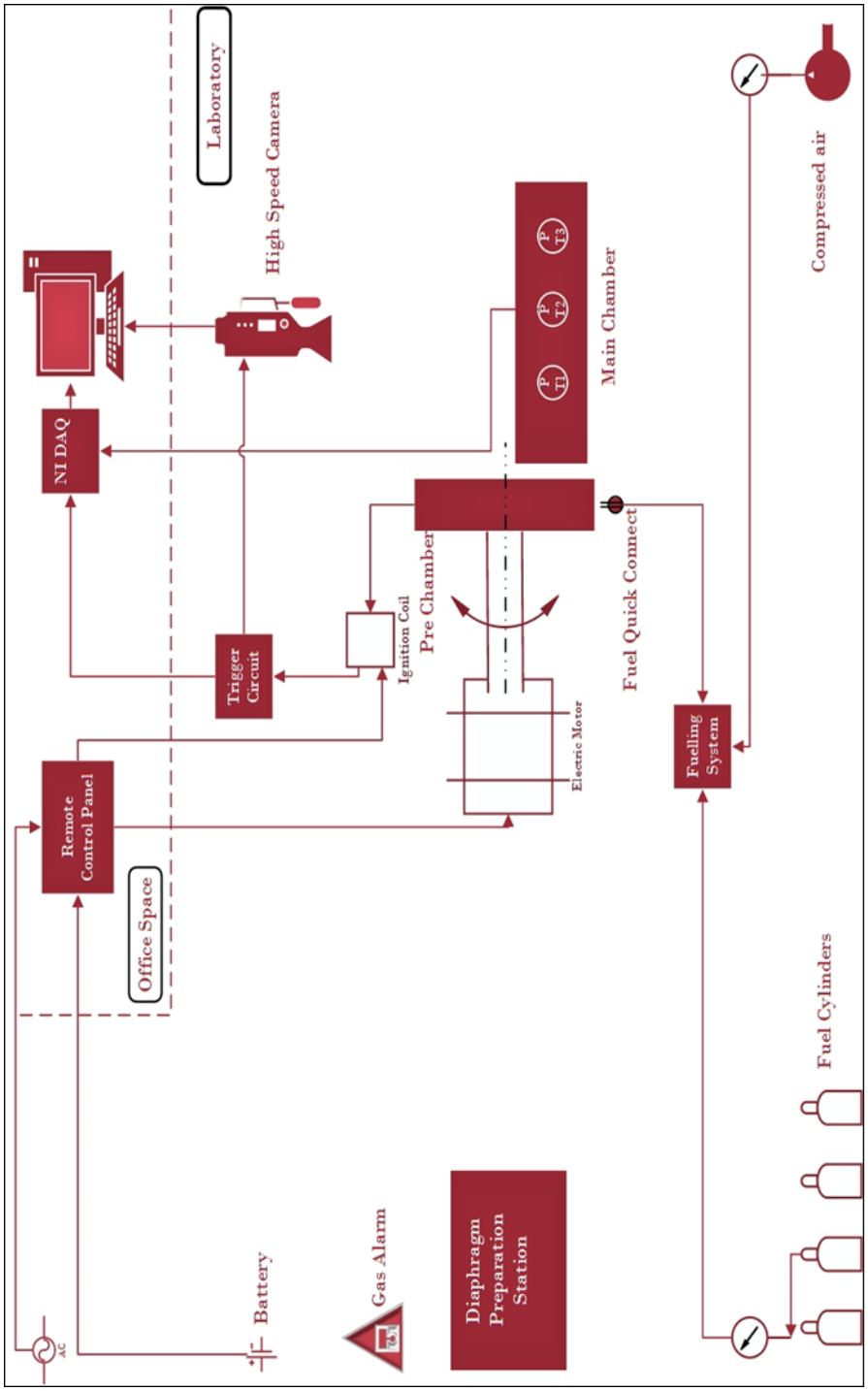

Figure 3. 1 CPRL experimental facility and layout

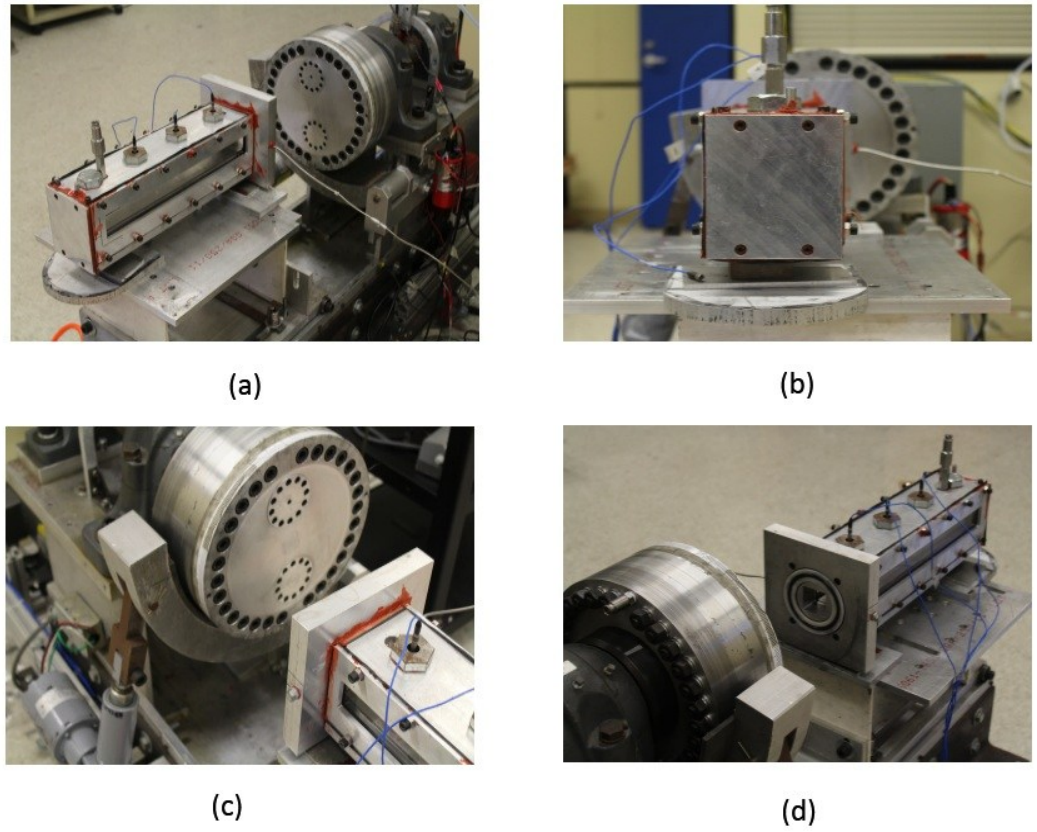

Figure 3. 2 (a) CVC rig showing main chamber side with transparent window with top pressure transducers, sliding bed, rotatable pre-chamber and drive motor (b) rear end of main chamber and fuelling port, (c) pre-chamber face showing nozzle facing main chamber front end, (d) main chamber showing front end with entrance and sealing ring assembly

3.1.1 Pre-Chamber

The cylindrical pre-chamber in the hot-jet ignition rig is used for producing and ejecting the hot jet of partially combusted products either as a stationary or a translating jet. The pre-chamber has a 275.6 mm (10.85 inches) outer diameter which is an assembly consisting of a front plate, back plate, and a middle ring. It encompasses an overall internal volume of 8.4×10^{-4} m^3 (51 cubic inches), a part of which is also occupied by the bolts heads used for the assembly. The pre-chamber can be filled with a fuel-air mixture by using either of the two fuelling ports located on the back plate. Mounted on the shaft, the pre-chamber

can be rotated to high speeds by an electric motor via a belt drive transmission. A Champion spark plug, model RC11ZYC4, with a spark gap of 0.045 mm is located on center of the back plate and is used for igniting the pre-chamber fuel-air mixture. The front plate has two large identical cylindrical stepped holes placed symmetrically to ensure static and dynamic balance of the pre-chamber under rotary test conditions. One of the pre-chamber front plate holes can be used for the nozzle insert assembly while the other can be used to mount a sealing blank or a pressure transducer (for stationary test only). The inserts used for the current study are shown in Figure 3.3.

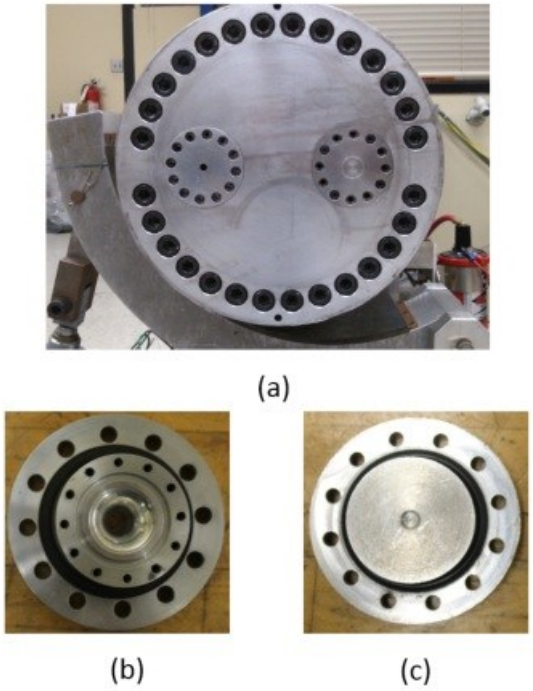

Figure 3. 3 (a) Front view of the pre-chamber (b) type A nozzle insert (c) sealing blank

3.1.2 Main CVC Chamber

The main CVC chamber is a long cuboid assembly that spans an overall length of 432 mm (17 inches) and a height of 103.4 mm (4.07 inches). The combustion chamber has a square cross-section with side dimensions of 39.9 mm (1.57 inches) and is 406 mm (16.0 inches) in length. For combustion diagnostics, optically accessible windows are located on both sides of the chamber across its length and pressure transducers are mounted flush on the top wall. The location of pressure transducers measured from the chamber entrance is listed in Table 3.1. The CVC chamber assembly is mounted on a sliding bed, as shown in Figure 3.2. The sliding bed assembly contains tightening bolts to firmly secure the main chamber when setting up and conducting experiments. By loosening these bolts, the main chamber can be moved to provide adequate clearance to access the pre-chamber.

Table 3. 1 Pressure transducer distance from main chamber entrance

Pressure Transducer	Distance from entrance (in)
PT1	3.25
PT2	7.25
PT3	11.25

Each main chamber optical window is a 1-inch thick Pyrex rectangular cube with a cross section measuring 14.40 × 1.57 inches. For structural reasons, the front edge of the main chamber optical window is located 40.6 mm (1.60 inches) away from the entrance. A fuelling port is located on the top wall at a distance of 108 mm (4.25 inches) from the main chamber entrance. While fuelling and conducting experiments, the CVC chamber is isolated and sealed from the environment using the sealing ring assembly attached to the main chamber entrance. The sealing ring assembly consists of two polyurethra O-rings and a sealing-ring made of Derlin plastic located at the main chamber entrance (Figure 3.2(d)). To create vacuum inside the main chamber, the sealing-ring assembly must be placed flush and the main chamber bolts must be secured. When the nozzle diaphragm ruptures the main chamber entrance is injected with the pre-chamber combustion products through the nozzle. Ignition occurs near the entrance and combustion proceeds simultaneously on both side.

3.1.3 Nozzle Insert

The cavity in the front plate of the pre-chamber can be inserted with one of the available nozzle inserts. The nozzle used for the current study has an area ratio of 1.0 with exit and throat diameter of 6 mm (0.236 inches). This nozzle labelled as Type A was studied by Perera [15] along with several other nozzles as listed in Table 2.1. Experiments performed using the type A converging nozzle recorded the minimum ignition delay times in the tests conducted as seen in Figure 2.11. The tests indicated that as the nozzle exit diameter decreased the ignition delay time increased. One reason for the increased ignition delay time may be the heat loss experienced by the combustion torch jet as it is forced through the narrow nozzle.

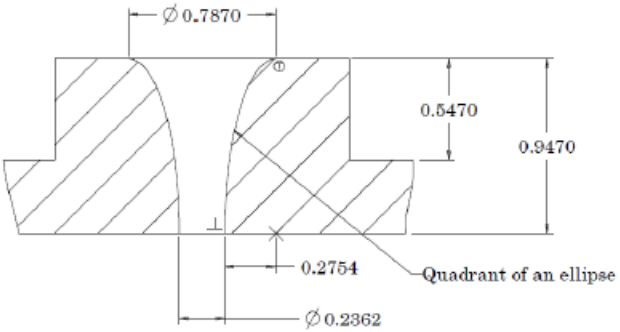

Figure 3. 4 Type A nozzle dimensions

3.1.4 Aluminum Diaphragm

The nozzle insert assembly contains a nozzle plate which can be used to assemble a diaphragm before the nozzle entrance. This nozzle assembly is then fixed into the pre-chamber nozzle cavity. The diaphragm material is full hard temper specification of Aluminum alloy 1100 with a thickness of 0.003±0.0003. The diaphragm is scored as described in the following section. The pressure rise in the pre-chamber due to combustion ruptures the diaphragm. Components that make up the nozzle assembly can be seen in Figure 3.5

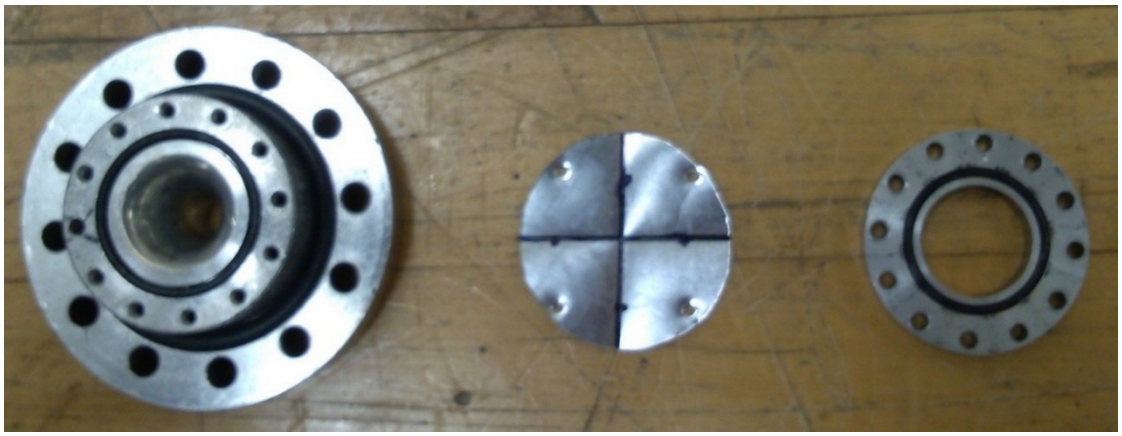

Figure 3. 5 Nozzle insert assembly: nozzle insert, diaphragm and nozzle plate (from left)

3.1.5 Diaphragm Scorer

A 50050 score 1^{TM} glass cutter used by Perera [15] was used to score the diaphragm to facilitate rupturing of diaphragm into four symmetric petals. The diaphragm is guided manually through a sliding bed and scored in horizontal and vertical direction passing through the center of diaphragm. Two complete passes were given in each direction by moving the slider up and down across the cutter. Diaphragm scoring depth can vary from one diaphragm to another due to this manual scoring and is a major variable in the current setup that needs to be controlled.

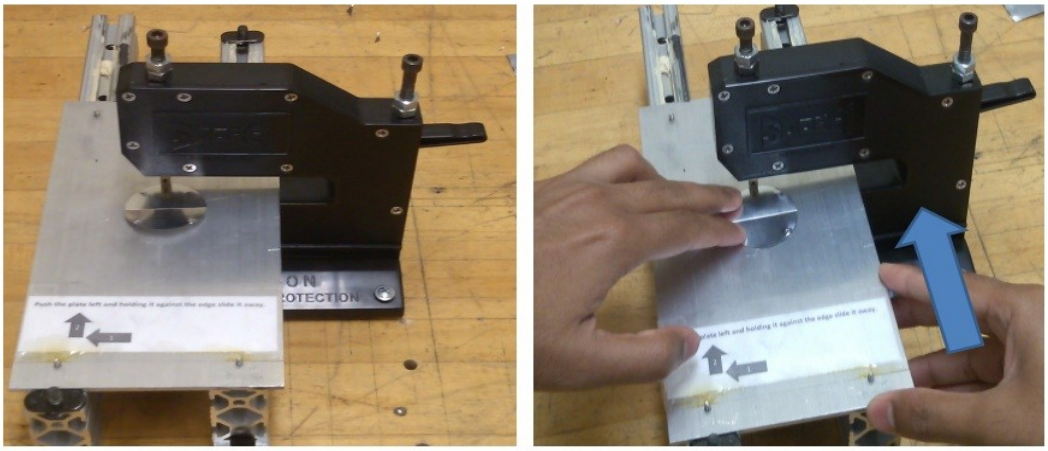

Figure 3. 6 Diaphragm scorer (left), manual scoring method (right)

3.1.6 Pre-Chamber Ignition System

The pre-chamber ignition system is used to initiate the spark in the pre-chamber in a controlled manner for both rotating and stationary experiments. The system used by Perera [15] for stationary tests was modified to facilitate timed ignition as the pre chamber rotates. The system consists of a 12V battery, MSD Capacitive Discharge Ignition (CDI) unit, MSD Blaster 2 ignition coil, MSD Trigger Sensor (PN 8276), and a spark plug. The addition of remote ignition control and MSD trigger sensor are the main modifications done to the existing system. The key ignition switch and battery connect toggle switch are located in the remote control panel which will be discussed in Section 3.1.7. Using these switches the system can be safely powered off. Section 3.2.1 describes the procedure on setting up the trigger sensor arrangement to control the spark timing as the pre-chamber rotates. To allow for pre-chamber rotation the ignition coil high tension cable is connected with the spark plug through a copper-rod that runs through a center hole along the pre-chamber shaft. A plexiglass tube was used to insulate the copper rod and hence avoid sparking with the steel drive shaft. Connection between trigger sensor and ignition unit had to be removed for stationary experiments.

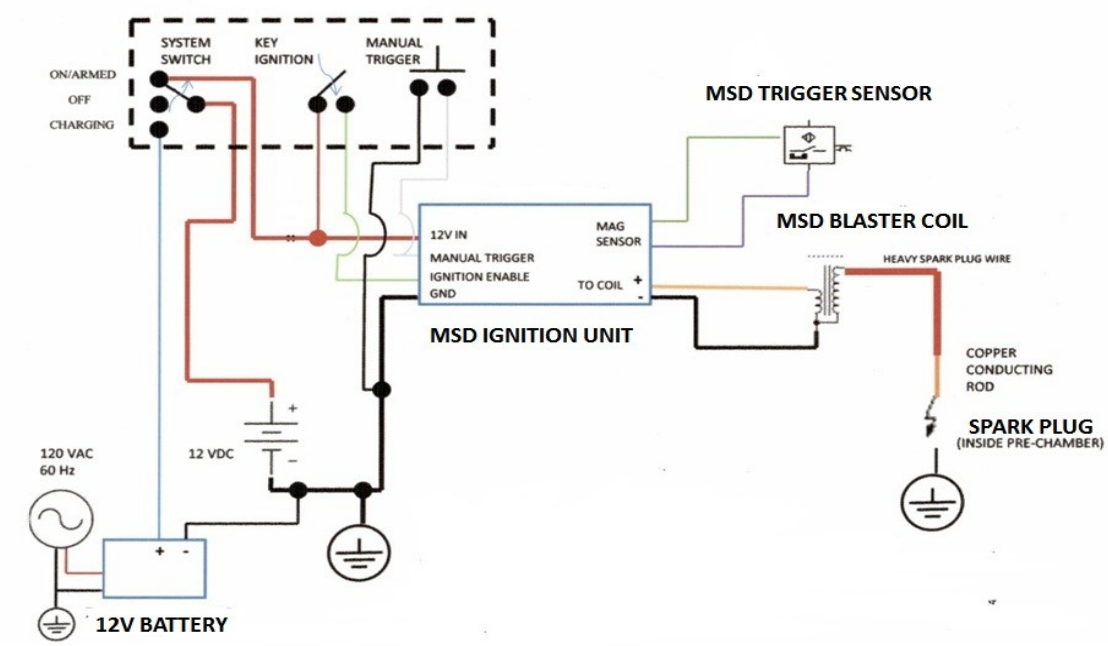

Figure 3. 7 Ignition system connections and components [52]

3.1.7 Remote Control Panel

The control panel consists of switches, keys and buttons required to control and execute the experiments from a safe location in an adjacent room to the laboratory room housing the rig. The panel was designed and fabricated with a sole purpose of bringing all the controls required for the experimentation onto one interface. Figure 3.8 indicates the available controls in the remote control panel. Other important safety features such as pre-chamber brake and emergency stop button is included in the panel. Variable Frequency Drive (VFD) controls mounted in the center allows for control of pre-chamber rotation speed. Manual ignition button is used for stationary experiments where the trigger sensor cannot be used. Detailed operating procedure of the panel can be found in Section 3.2.2.

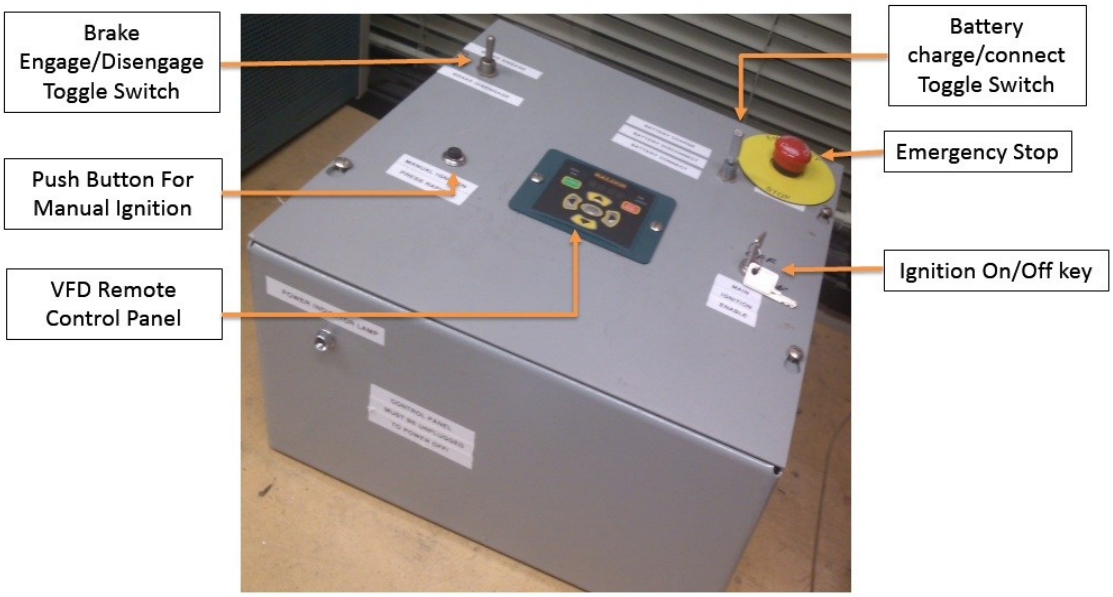

Figure 3. 8 Remote control panel

3.1.8 Fuelling System

The fuelling system used in the CVC hot-jet ignition rig is used to fuel the pre-chamber and main chamber with a single fuel or fuel blend of any equivalence ratio and is capable of producing mixtures at atmospheric or higher initial pressures. The partial-pressure fuel filling method as explained in Section 3.2.4 is used for preparing the fuel-air mixtures. The fuelling system consists of a set of valves, flow lines, pressure gauge, vacuum pump and quick connectors mostly procured through the vendor Swagelok®. The whole system is mounted on a steel cart making the system mobile. Detailed procedure on operation of the system can be found in the section 3.2.5.

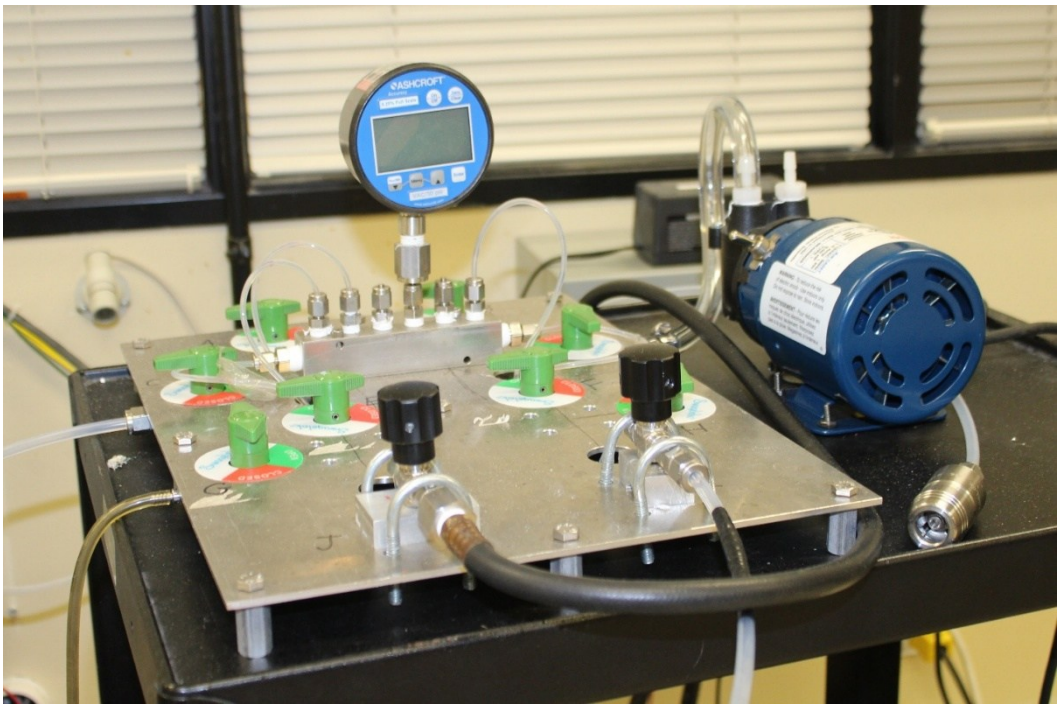

Figure 3. 9 Fuelling system in CVC rig

3.1.9 Data Acquisition System

Data acquisition system comprises of the fast response pressure transducer data acquisition system and the high-speed video camera system. Both the systems are triggered by the falling edge signal from the synchronizing circuit.

3.1.9.1 Pressure Transducer Data Acquisition System

Three PCB Piezotronics^{INC} ICP® (Integrated Circuit-Piezo Electric) 113A32 dynamic pressure transducers were used in the current study to measure the spatial pressure variation along the main CVC chamber. These high frequency general purpose transducers had a voltage sensitivity of 1.029 mv/psi and can be safely used for applications exceeding 5000 psi. The transducers were connected to a 4-channel NI SCXI-1530 signal conditioning module designed for ICP transducers. Only 3 channels were used for this study whereas channel 4 was reserved for the pre-chamber pressure transducer. Each

channel had a 4mA, 24V current source to power the ICP transducers. Figure 3.10 indicates the different components that comprises the data acquisition system. One 111A26 pressure transducer with a higher voltage sensitivity of 9.905 mv/psi was used for the purpose of testing the system and the channel lines using a compressed air source. Pressure transducer specifications are attached in Appendix C.

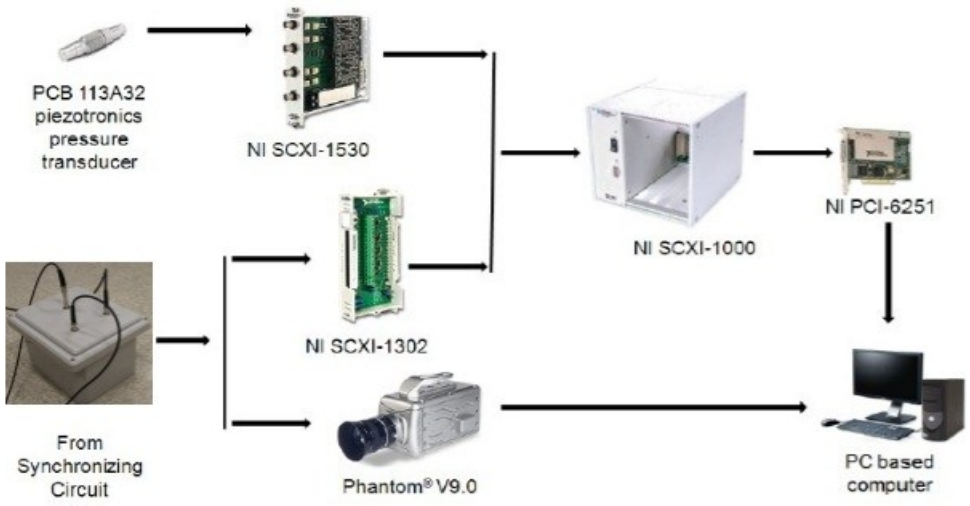

Figure 3. 10 Components in the data acquisition system

3.1.9.2 Labview Virtual Instrument

National Instruments LabVIEW Developer Suite™ 2009 was used to develop a virtual instrument (VI) that controls the hardware in the pressure data acquisition system. The main function of the VI is to recognize the trigger event and start recording the pressure values against time on to a tab delimited text file. The front panel and the block diagram of the VI is attached in Appendix D. The program contains options to modify the number of channels input, sampling rate and source of trigger (trigger signal or manual trigger). The sub functions used in the VI allows further control which can be referred through LabVIEW help manual.

3.1.9.3 High-Speed Video Camera

A Vision Research Phantom v9.0 monochrome high-speed camera was used in this study to record the transient hot-jet ignition process. The camera is used along with a Nikon F-AF Nikkor 50 mm f/1.8 D lens with the f-number 1:1.8. The camera is capable of capturing up to 144,175 frames per second (fps) and a maximum resolution of 1632 × 1200 pixels. The camera's maximum fps is inversely proportional to the desired resolution. For the current study a resolution of 1632 × 104 is used with images captured at 10000 fps. This frame encompasses a rectangular window which covers the optical window in the main chamber and part of the pre-chamber so that the angular markings in the pre-chamber will be visible in room lighting conditions. The camera's position is fixed at a safe distance of 5 feet from the main chamber window. In order to align the camera lens vertical and horizontal symmetric lines with the vertical and horizontal lines of the optical window, two mounted laser targets were used in the camera. The procedure for aligning the camera using the laser targets is detailed in the previous study done by Perera [15].

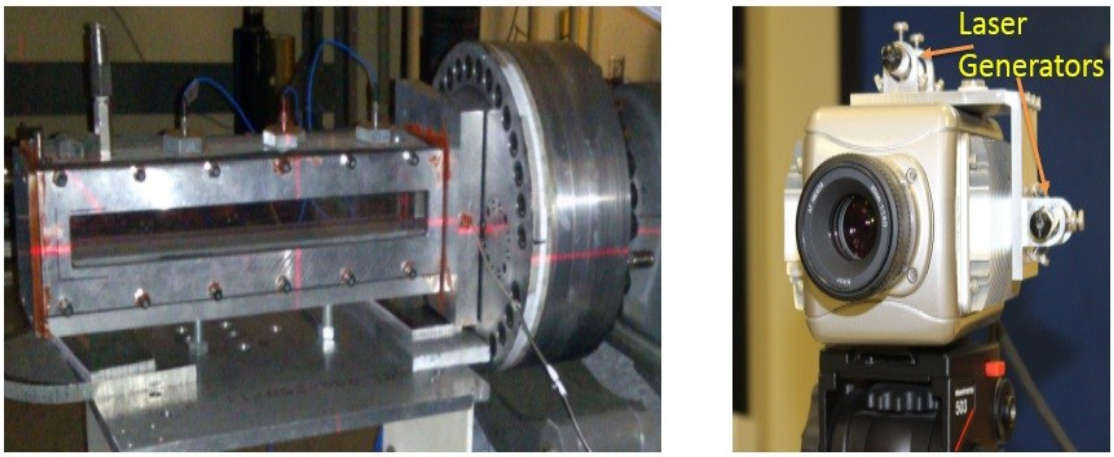

Figure 3. 11 Projected laser lines on the CVC rig (left), camera mounted with laser targets (right)

Phantom camera control software revision 675 was used to control and adjust various settings. The exposure was maintained at 96.75 μs (maximum exposure allowed at 10,000 fps) and EDR (Extreme Dynamic Range ™) exposure of 0 μs. EDR can be used to adjust exposure on pixel level to reduce over-exposure at certain regions due to bright spots. Setting EDR exposure time to 0 μs, the exposure level at the time of triggering the camera remains unchanged for the entire series of captured images. Exposure time is the effective length of time a camera shutter is open. Hence for the current setting the camera's sensor is exposed to the object for 96.75 μs every 100 μs. Exposure time can have dramatic impact on appearance of moving objects. The reason for using a high exposure level was to expose the camera to the slightest illumination possible from the luminosity emitted by the gas mixture in the main chamber for detecting ignition accurately.

3.1.9.4 Spectral Response of Phantom V9.0 Camera

Light is an electromagnetic radiation and it comprises a wide range of wavelengths. The photodiodes used in the camera produces a corresponding voltage in response to the incident radiation or light or photons through photoelectric effect. The sensor in the camera is exposed to the objects radiation for the specified time defined as the exposure time and this creates a useful voltage. The percentage of photons hitting the camera's sensor that produces this useful voltage is called Quantum Efficiency (QE). The QE differs for different ranges of incident wavelength. Different cameras have different ranges of sensitivity towards the incident wavelength. This is specified as the camera's spectral response and the range is specified by the manufacturer. The camera's spectral response is shown in Figure 3.12. The curve indicates the variation in quantum efficiency with respect to incident wavelength. Phantom camera had a spectral response in the range of 400-1000nm. This covers the visible range and a portion of infrared range (700-1000nm). Combustion researchers may use different ranges of wavelength for their study. Attard [53] observed the chemiluminescence emitted near the blue portion (450 – 495nm) of the visible spectrum which corresponds to radical species such as CH, CH_2O and C_2. Sadanandan [23] used a high reflection filter on a CCD camera that allows radiation only in the range of

275-295 nm. This range corresponds to emission from OH radical excited using Nd:YAG laser cluster.

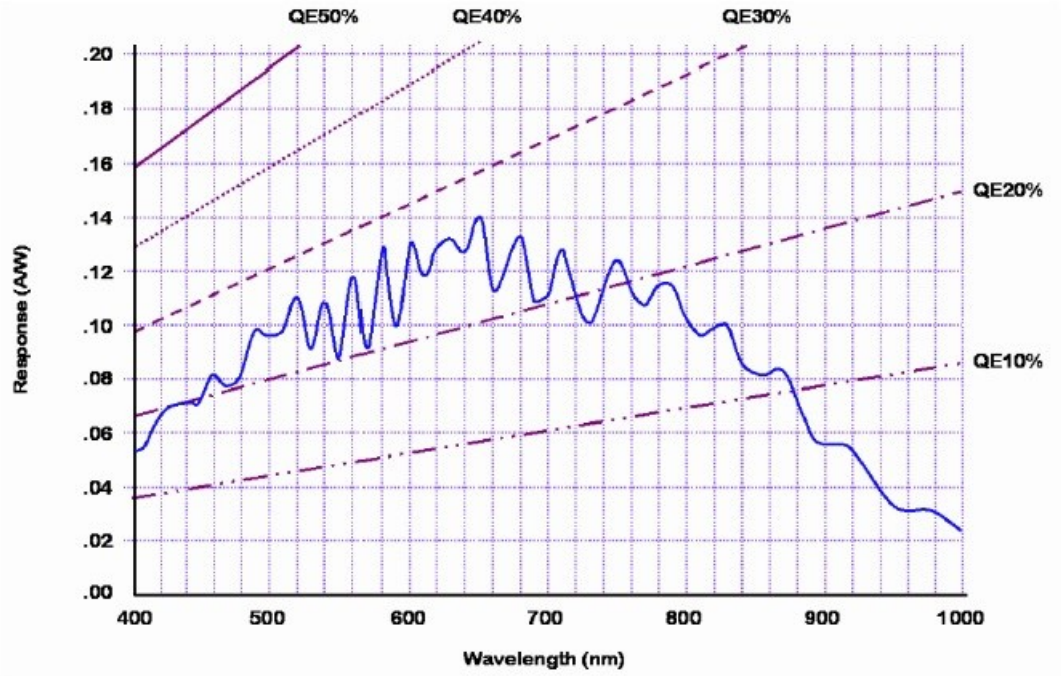

Figure 3. 12 Phantom V 9.0 spectral response curve with quantum efficiency

3.1.9.5 Resolution and Pixel Area

The original images were acquired at a resolution of 1632×104. The images were cropped to 700 × 79 which covers the optical window with a dimension of 365.8 mm (14.40 in) × 39.9 mm (1.57 in). This distributes 55300 pixels over an area of 14234.7 mm^2. Every pixel covers 0.3 mm^2 area of the optical window with individual pixels dimensions of 0.5 mm × 0.5 mm. A pixel at every half of a millimeter of physical distance ensures sufficient amount of resolution and detail for further image processing.

3.2 Experimental Procedure

The following section of chapter describes the experimental procedure for studying the traversing hot jet ignition process in the CVC rig. The sections are divided based on individual systems with the operating procedure explained for each one of them.

3.2.1 VFD Control Panel and Frequency Adjustments

The VFD controller mounted on the remote control panel allows adjustments of several motor parameters from a safe distance. Adjustments to operational settings like lower and upper frequency limits, desired operating frequency, acceleration time, deceleration time, methods of initiation, and multiple other parameters can be made from the controller. The speed of the motor is adjusted by changing the operating frequency. Table 3.2 indicates VFD frequency inputs and the resulting pre-chamber speed. The speed of the pre-chamber was measured using a laser tachometer and the measurements were made when the main chamber was not placed flush against the pre chamber. The numbers in the Table 3.2 corresponds to the final setting on the VFD after adjusting the frequency calculated from the angle delay program based upon the speed measured in the tachometer.

Table 3.2 VFD frequency versus resultant pre-chamber speed

VFD Frequency Input (Hz)	Pre-Chamber Speed (RPM)
3.75	150
19.62	750
25.54	1000
31.95	1250
38.36	1500

3.2.2 Spark Trigger Setup

The current spark ignition setup consists of a magnet attached to the rotating steel shaft, which would trigger the spark upon moving past the stationary MSD non-magnetic

crank sensor. This arrangement consists of components used in MSD flying magnet crank-trigger setup preferred for its accurate high voltage trigger signals compared to a conventional crank trigger arrangement. The magnet is adjustably to the steel shaft using a hose-clamp arrangement. The main purpose of the adjustable magnet arrangement is to facilitate variation of spark trigger angle depending upon the pre-chamber's speed of rotation. Figure 3.13 shows arrangement of the crank sensor, magnet and the clamp adjustment. The angular position of the magnet based on the rotation speed and pre-chamber fuel can be determined by using a developed LabVIEW VI called "Angle Delay". After an initial setup the spark trigger angle is further fine-tuned by performing preliminary experiments with the high-speed imaging system. The experiments will be discussed in section 4.1.3.1.

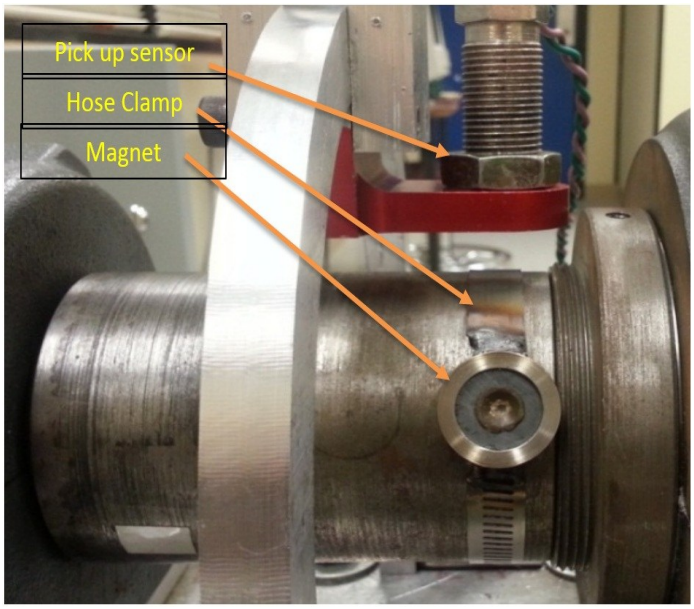

Figure 3. 13 Magnet and hose-clamp arrangement with pick up sensor

3.2.3 Remote Control Panel

Functional layout of the remote control panel is shown in Figure 3.14. The remote control panel needs a separate AC input, which should be disconnected when shutting down the rig's power. The system toggle switch is used to connect the 12 V battery power source

to the ignition circuit or connect it to the charging circuit. Before the start of an experiment it is required to disengage the pre-chamber emergency break using the brake toggle switch. The break is used for stationary experiments and for emergency purpose only. It should not be routinely used to stop the pre-chamber rotation after an experiment. Doing so will introduce unnecessary heat on the pre-chamber walls and will cause variations in experimental initial conditions. Instead the pre chamber is allowed to decelerate using the VFD settings for the motor. VFD control for the three phase electric motor is located on the center of the remote control panel. Detailed procedure on VFD operation is given in the following section.

3.2.3.1 Instructions – Operating the VFD

Set the VFD in the desired frequency and press the start button (green) in the VFD control to spin the pre-chamber. Allow few seconds for the pre chamber to accelerate to the desired speed. Now move the system switch to ON position and turn the ignition key in the clockwise direction to close the spark ignition circuit. The spark will be produced after the ignition coil receives a signal from the magnetic pickup sensor. The manual ignition push button is used for stationary pre-chamber experiments where the pickup sensor arrangement does not apply. The E-stop button is provided for emergency situations; pressing it will activate the pre-chamber brake and kills the power to rest of the system.

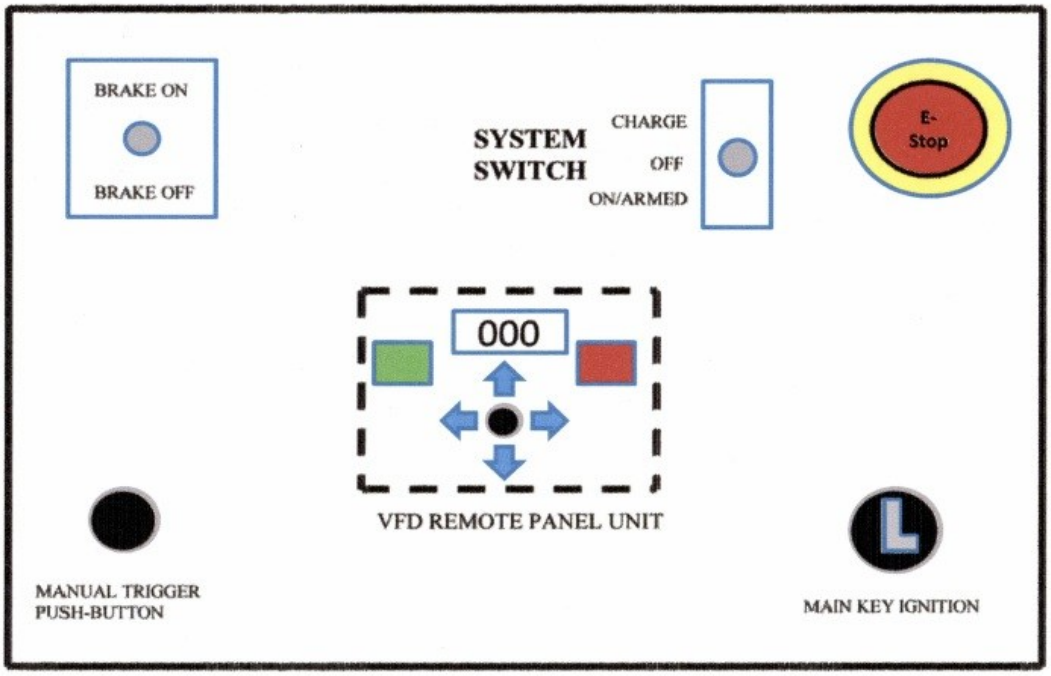

Figure 3. 14 Layout of controls on remote control panel

3.2.4 Partial Pressure Method for Fuelling

The equivalence ratio of the fuel-air mixture in each chamber is controlled by delivering the fuel using partial pressure method via a fuelling system. The fuelling system operation will be explained in the following section. According to Dalton's law of partial pressure, the total pressure exerted by a mixture of non-reactive gases is equal to the sum of the partial pressures of individual gases and is expressed as

$$P = \sum P_i = \sum P\chi_i$$

Where P is the total pressure of the system, P_i is pressure of individual species and χ_i is the mole fraction of *i*th species. The reaction of a hydrocarbon with air in a stoichiometric mixture can be represented by the below step,

$$C_xH_y + \left(x + \frac{y}{4}\right)(O_2 + 3.76N_2) \rightarrow xCO_2 + \frac{y}{2}H_2O + 3.76\left(x + \frac{y}{4}\right)N_2 \quad 3.1$$

Mass fraction of individual components in the reactant side can be represented as

$$\chi_{C_xH_y} = \frac{N_{C_xH_y}}{N_{reactants}} \quad 3.2$$

Number of reactants is represented as

$$N_{reactants} = N_{C_xH_y} + 4.76\left(x + \frac{y}{4}\right) \quad 3.3$$

Overall total pressure in the chambers can be represented as P_{total}, which is usually barometric pressure

$$P_{total} = P_{Air} + P_{Fuel} \quad 3.4$$

Where,

$$P_{Fuel} = P_{total} \times \chi_{C_xH_y} \quad 3.5$$

For rich or lean mixtures number of moles of air constituents remains unchanged as per stoichiometric representation however number of moles of fuel will change. The equivalence ratio is

$$\phi = \frac{\left(\frac{A}{F}\right)_{Stochiometric}}{\left(\frac{A}{F}\right)} = \frac{\left(\frac{F}{A}\right)}{\left(\frac{F}{A}\right)_{Stochiometric}} \quad 3.6$$

$$\left(\frac{F}{A}\right) = \frac{N_{C_xH_y} \times MW_{C_xH_y}}{\left(x + \frac{y}{4}\right) \times \left(MW_{O_2} + 3.76 \times MW_{N_2}\right)} \quad 3.7$$

Usually Φ is specified. Thus $N_{C_xH_y}$ can be found out from the Eq 3.7 and can be used in Eq 3.3 to calculate the partial pressure values.

Reaction of a hydrocarbon and hydrogen fuel blend with atmospheric air can represented by

$$C_xH_y + lH_2 + \left(x + \frac{y+2l}{4}\right)(O_2 + 3.76N_2) \rightarrow xCO_2 + \frac{y+2l}{2}H_2O + \left(x + \frac{y+2l}{4}\right)3.76N_2 \quad 3.8$$

For a stoichiometric mixture where the molar ratio of hydrogen to hydrocarbon is denoted by *l*. Thus total moles of reactants is

$$N_{reactants} = 1 + l + 4.762(x + (y+2l)/4) \quad 3.9$$

Partial pressures of hydrocarbon and hydrogen can be found out individually as described in the beginning of this section.

For all the experiments conducted in this study the total pressure P was equal to atmospheric pressure. A vacuum pressure P_1 is created using the fuelling system. P_{fuel} found from the above relation is used to attain a pressure of P_2 by allowing fuel into the chamber

cavity after which the chamber pressure is brought back to 1 barometric pressure by allowing the atmospheric air inside. Hence

$$P_1 = P_2 + P_{Air} \quad 3.10$$

3.2.5 Preparation of the Fuelling System

Initial step of fuelling (either the pre-chamber or the main chamber) involves connecting the system with one of the fuel main storage tanks. Fuel is supplied into the system from the tank via a single fuel line which connects into Valve 2 shown in Figure 3.15. The fuel line have a quick connector, which can be mated with a fuel main tank outlet through a pressure regulator system. After the quick connector is secured, the tank main valve is opened and the pressure regulator is adjusted to allow 10 to 15 psig in the fuel line. Valve B and Valve 2 is then opened releasing the pressurized fuel to atmosphere. This action purges the fuel line. The line is purged twice before an initial run of experiment or after changing the fuel type. Valve 2 and valve B are closed after purging and a pressure of 10-15 psig is maintained in the line for fuelling the chamber cavities.

3.2.5.1 Instructions - Standard Fuelling

The fuel out line from valve F of the fueling system consists of a quick connector that can be mated either with the pre-chamber or the main chamber. To begin fuelling engage the quick connector in the line to the pre-chamber. Start the vacuum pump and open Valve F, Valve D and Valve E in that order. This ensures that high pressure fuel in the system is removed through the vacuum before entering the pre-chamber fuel line. Run the vacuum pump until a gauge pressure P1 of around -10 psig is reached. Now close Valve F and turn off the vacuum pump. Valve 2 is a flow control valve. Adjusting the valve allows the fuel be admitted in a controlled flow rate into the pre-chamber until the desired pressure P2 is reached as calculated from the partial pressure method. Now close valve D and open the Valve G to allow the pressure in the pre-chamber to equalize with the ambient pressure.

Close all valves in the fuelling system and disconnect the fuel quick connector. Disconnect the fuel line from the main tank by removing the quick connector. Allow five minutes before start of the test for the fuel to diffuse until a homogenous mixture is obtained as established by Perera [15] through experiments. The above method can be used for both pre-chamber and main chamber fuelling.

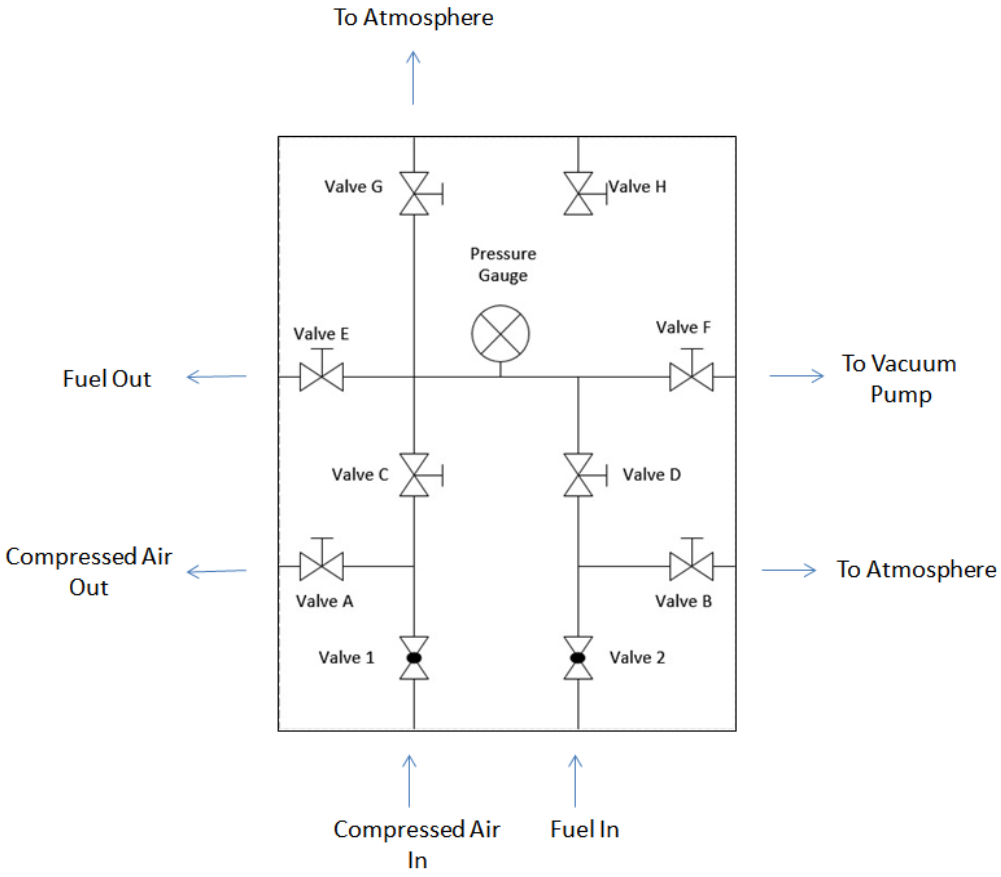

Figure 3. 15 Fuelling system layout

3.2.5.2 Instructions - Pre-Chamber Fuelling

Before fuelling, the pre-chamber is purged with compressed air for five minutes to remove any residual exhaust gases from the previous test. Fix the nozzle insert assembly firmly using the provided screws. Now continue filling the fuel using the standard fuelling pressure. During the vacuum operation if it was found that the vacuum was leaking then check the O-rings in the nozzle inset assembly and continue filling the fuel.

3.2.5.3 Instructions - Main Chamber Fuelling

Before fuelling the main chamber, purge the cavity with compressed air for five minutes. The sealing ring assembly has to be retracted from its crevice before placing it flush against the main chamber. Apply an even thin film of lubricant to facilitate pre-chamber rotation when it is placed flush against the main chamber's sealing ring assembly. After the sealing assembly has been retracted move the main chamber and press it flush against a flat surface on the face of the pre-chamber (If the sealing ring assembly is placed against the nozzle insert then the screw holes might cause leakage). Use a wrench to secure in the main chamber. Now follow the standard fuelling procedure to fill the main chamber. Replace the polyurethane O-ring with a new one after each test.

3.2.5.4 Instructions-Hydrogen-hydrocarbon blend fuelling

Standard fuelling procedure is followed until stagnation pressure P2 is reached for the hydrocarbon fuel. Now close valve E. Open Valve F and start the vacuum pump to evacuate the hydrocarbon fuel from the line. Close Valve 2, Valve D and Valve F. Now switch the quick connector from hydrocarbon fuel to the hydrogen main tank and purge the line as mentioned in section 3.2.5. Open valve E. Adjust the flow control until stagnation pressure P3 is reached. Now close valve D and open the Valve G to allow the pressure in the pre chamber to equalize with the atmospheric air. Close all the valves and disconnect the quick connectors from the system.

4. PRELIMINARY EXPERIMENTS AND DEFINITIONS

The traversing hot-jet ignition experiment involves several consecutive events that occurs on a millisecond scale. Completion of one event triggers the next event in a precise manner. The current chapter discusses the sequence of events observed in the experiments with their assigned definitions. The chapter also includes the preliminary experiments that were conducted to define and measure these events. Definitions of these events were established to allow for quantitative measurement of parameters that allows for description of the hot-jet ignition process. As described in Chapter 3, prior to the spark ignition, the nozzle in the pre-chamber remains closed by the diaphragm. Once the pre-chamber is spun to its desired speed the mixture held is ignited by a spark plug which triggers the pre-chamber events as shown schematically in the Figure 4.1. Timing of the spark-trigger and the relative position of the nozzle across the main chamber entrance should be controlled with a tight tolerance. The current study focuses on pre-chamber speeds between 150 rpm to 1500 rpm. A set of preliminary experiments were required to setup the rig and make it suitable for conducting experiments and acquiring data at different pre-chamber speeds.

4.1 Pre-Chamber Events

Inputs received from the remote control panel during the experiment initiates a series of events hereby defined as pre-chamber events that proceeds in a timely manner until the completion of combustion in the main chamber. This section describes each of the pre-chamber events and its significance. Figure 4.1 indicates the sequences of events as the pre-chamber rotates when viewed from the rear end of the main chamber looking at the face of pre-chamber. Table 4.1 contains the tested pre-chamber speeds in the current study and the corresponding nozzle parameters.

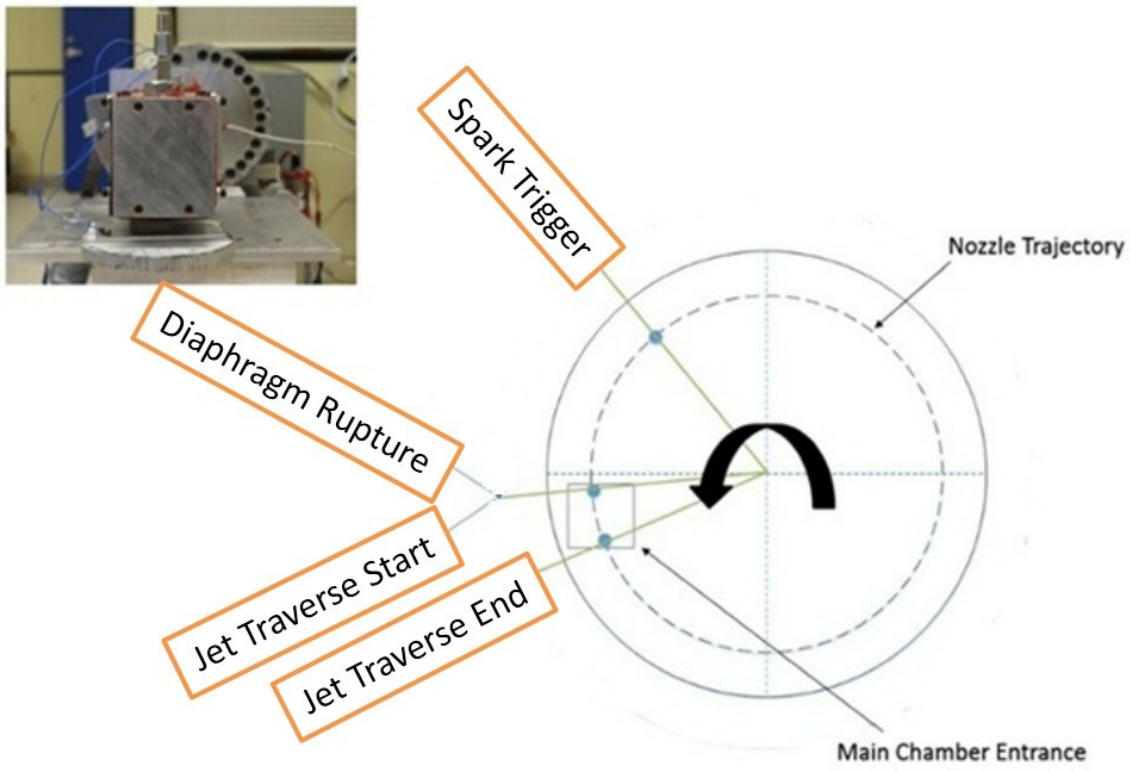

Figure 4. 1 Schematic indicating pre-chamber events in the order of occurrence

4.1.1 Spark Trigger

The angle at which spark is triggered is determined based upon the desired pre-chamber speed. The spark-trigger is controlled and set by the adjusting the magnetic pick up arrangement which is set using the angular markings in the pre-chamber. This angle will be recorded as 'spark delay angle' in the current study. Spark initiation triggers the rest of the pre-chamber events. The experimental parameters will be expressed in terms of milliseconds, which may be converted to pre-chamber nozzle angular position based on the rotation speed.

Table 4. 1 Summary of pre-chamber speeds investigated for the current study

Pre-Chamber Speed (RPM)	Nozzle Traverse Time (ms)	Nozzle Linear Velocity (m/s)
150	40.6	0.983
750	8.1	4.917
1000	6.1	6.556
1250	4.9	8.195
1500	4.1	9.834

4.1.2 Diaphragm Rupture

The onset of spark inside the quiescent pre-chamber sets of a flame that consumes the mixture resulting in pressure rise in the chamber. This leads to rupture of the aluminum diaphragm into 4 symmetrical petals and thereby issuing the high-speed hot jet into the main chamber. Figure 4.2 illustrates the pressure time history recorded by Perera [15] with stationary pre-chamber containing ethylene at an equivalence ratio of 1.1. All the ten test cases plotted are for the same initial conditions. The purpose of this preliminary experiment was to evaluate the variability of pressure rise in the pre-chamber for repeated tests. The diaphragm rupture pressure was recorded as approximately 54 psig. The pre-chamber pressure continues to rise even after the diaphragm has ruptured. A peak value of approximately 93 psig is recorded (Figure 4.2) indicating ongoing combustion in the pre-chamber after the start of jet ejection. The time at which the diaphragm ruptures is an important parameter in the traversing jet experiment and it was measured as described in the following section.

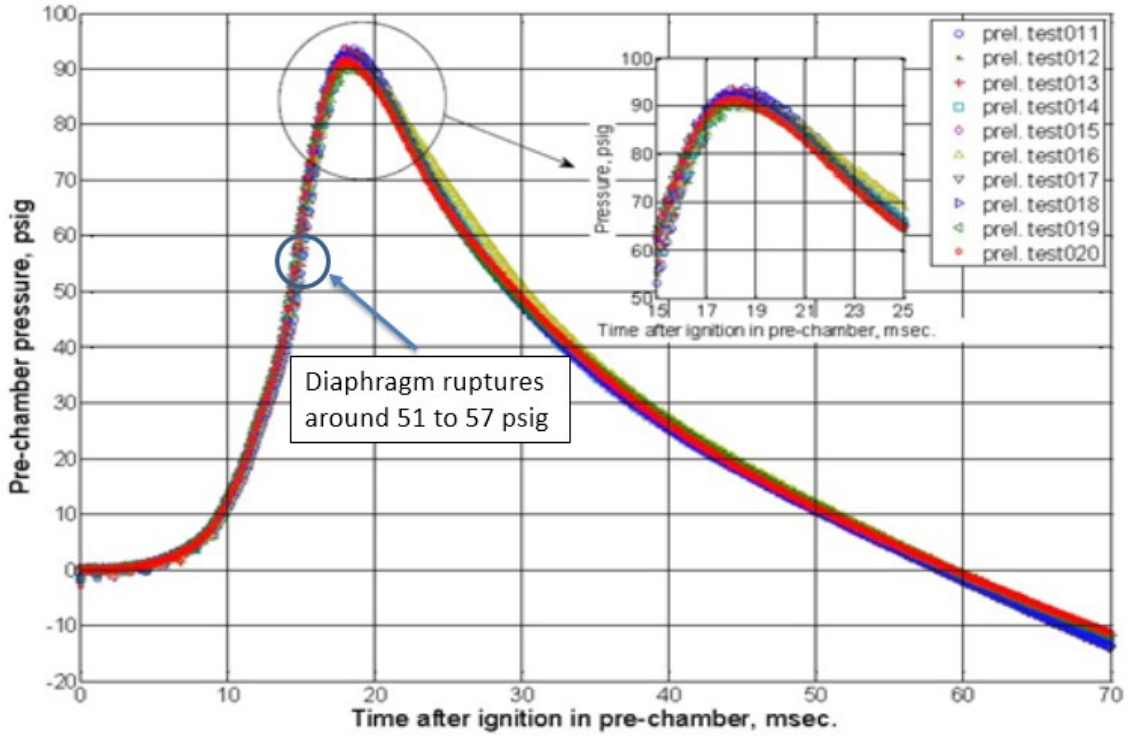

Figure 4. 2 Stationary pre-chamber pressure history measured during ten repetitions at identical conditions [15]

4.1.2.1 Diaphragm Rupture Time Evaluation

The scored aluminum diaphragm setup used in the pre-chamber is intended to create significant pressure difference between the chambers that upon rupture directly affects the penetration length of the hot-jet, the amount of hot gas ejected and other physical properties. The large pressure difference enables sufficient amount of hot-jet mass to be injected into the main chamber in a short duration which becomes critical as the jet traverse speed increases. The diaphragm rupture event is characterized by the diaphragm rupture time, which is defined as the elapsed time from the trigger pulse, to the first appearance of luminosity in the nozzle interior as captured in the high-speed images. The trigger pulse corresponds to initiation of spark in the pre-chamber.

Perera [15] measured diaphragm rupture time by performing several tests on the stationary pre-chamber and measured the variation of the rupture time in each tests. The main source of rupture time variation was attributed to variation in depth of scoring on the aluminum diaphragms. Diaphragm rupture time variation is a crucial aspect to consider in the traversing hot-jet ignition study since it defines the start of the jet ejection and ignition delay time, which will be discussed later. The variation in diaphragm rupture time can lead to pre-mature or late start of jet injection which will affect the next set of events that follow.

Diaphragm rupture time reported by Perera [15] for the stationary pre-chamber was re-evaluated with ethylene-air mixture at $\Phi = 1.1$ and the pre-chamber spinning at 150 rpm. The camera was placed at a safe distance of about 5 m in front of the rotating pre-chamber, and the images were recorded at a 480 × 480 resolution that encompasses the entire pre-chamber within the frame. Perpendicular laser targets were used to identify the axis of the pre-chamber, as the experiments were performed in dark conditions. The video was captured at a frame rate of 6400 frames per second (fps), limited by the set resolution. The lens aperture was set to an f-number of 1:1.8 and the exposure time was 153 μs. Figure 4.3 shows the high-speed camera's field of view in room lighting condition and the jet luminosity observed in dark conditions. The laser targets can be identified as vertical lines in the images representing the horizontal and vertical axis of the pre-chamber. Care was taken to ensure removal of the residual gas left from the previous experiment, hence diaphragm rupture time variation as a result of residual gas fraction in the mixture is negligible.

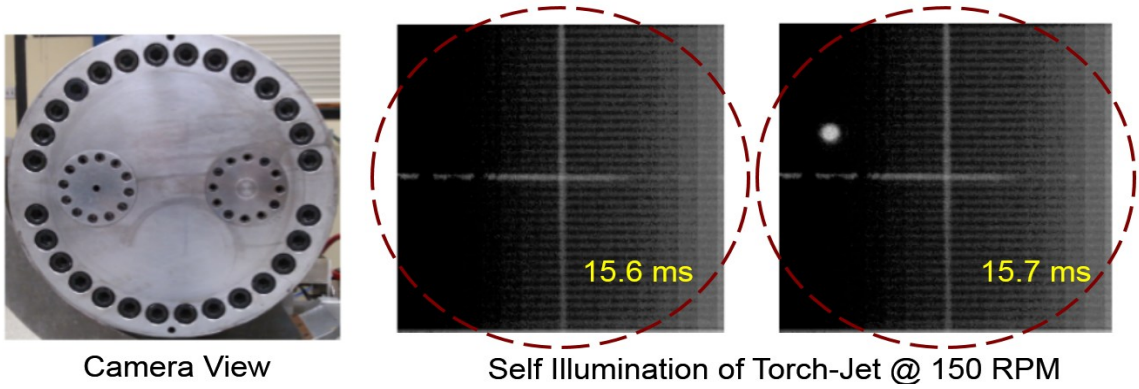

Figure 4. 3 Diaphragm rupture time evaluation using high-speed imaging (Pre-chamber speed: 150 RPM)

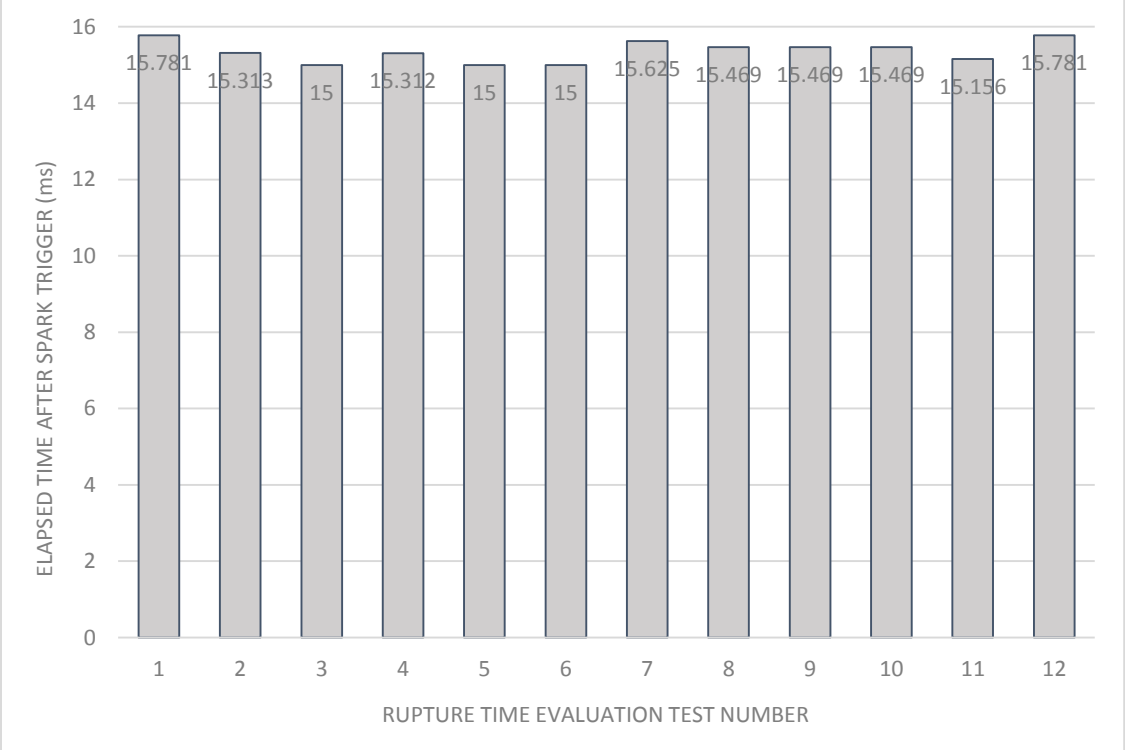

Figure 4. 4 Bar graph with the measured diaphragm rupture time variation across tests conducted

A series of tests were performed in the above-mentioned setup and a mean value of the diaphragm rupture time was measured as 15.4 ms with a standard deviation of ± 0.3ms. This corresponds to 13.2 degrees of rotation at 150 rpm, and 69.1 degrees of rotation at 750 rpm respectively. Figure 4.4 is a bar graph with the measured diaphragm rupture time and the variation observed for each tests.

Perera [15] reported that 15% of the tests conducted failed due to improper diaphragm rupture. During this current study for few preliminary experiments similar unreliability was observed where the diaphragm did not rupture into four symmetrical petals. It was found that root cause of the problem lied in the manual scoring method. When two complete passes were made by moving the glass cutter up and down, sometimes the path of the score did not overlap with each other resulting in reduction in depth of score at certain regions. These areas did not rupture during the test, which manifested as uneven rupturing of petals. Figure 4.5 shows the comparison between a defective diaphragm score and a proper one. The defective diaphragms were eliminated by visual inspection. None of the tests conducted in the current study failed due to uneven rupturing of diaphragm.

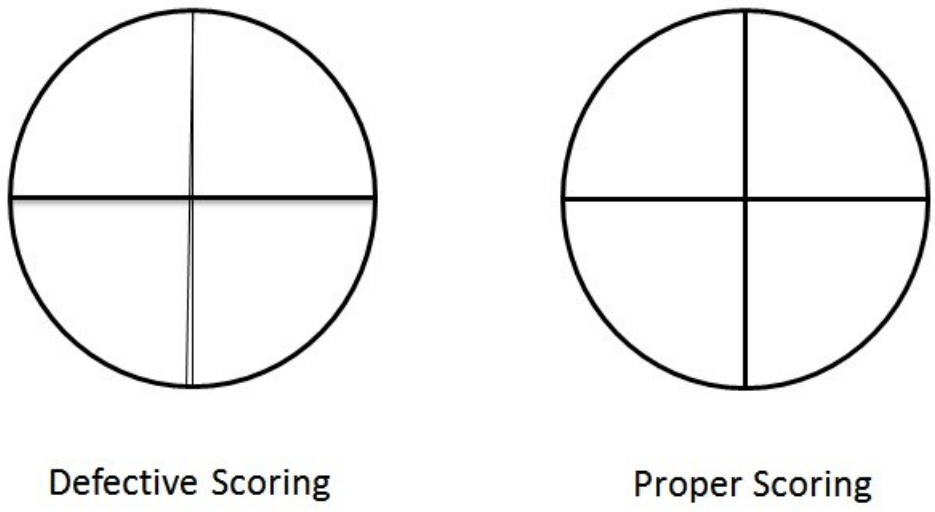

Figure 4. 5 Comparison of diaphragm score pattern after two scoring passes

4.1.3 Jet Traverse Start

The event is characterized by the start of injection of hot gas from the pre-chamber into the main chamber through the nozzle. The diaphragm rupture event starts the jet translation across the main chamber entrance when properly timed. The spark angle delay along with the diaphragm rupture time controls the spatial location of the jet translation start event. After the spark angle delay is set using the 'angle delay' Labview® VI program it is mandatory to fine tune the magnet location to ensure that jet translation starts at the instance when the nozzle becomes completely exposed to the main chamber. Wrong jet ejection location will lead to significant loss of injected hot jet mass at slow nozzle traverse speeds or it can result in a delayed jet start thereby reducing the amount of mass introduced into the main chamber at higher nozzle traverse speeds. Hence, a few preliminary jet alignment tests were performed at every pre-chamber speed setting to ensure the synchronization of diaphragm rupture and alignment of nozzle with main chamber entrance. The jet start alignment experiments are described below.

4.1.3.1 Jet Start Alignment Experiments

A few preliminary experiments were performed to identify the start of jet ejection with respect to pre-chamber angular location using the high-speed images. The recorded high-speed images are analyzed and necessary adjustments were made to the magnetic pick up arrangement. Depending upon the outcome of the jet alignment experiments the spark timing is either advanced or retarded. On an average 3 or 4 tests were performed at each pre-chamber speed to attain the targeted jet ejection location.

The horizontal laser target in the camera which was previously used for camera alignment was switched on and used as reference for locating the angular marking in the pre-chamber. The horizontal laser target creates a line across main chamber and the pre-chamber as shown in Figure 4.11. An intentional mark as shown in Figure 4.6 is made at an angle of 166˚ such that when the marking at the pre-chamber and the laser target coincides, the nozzle becomes completely exposed to the main chamber entrance. A faint light source is used to light the angular markings on the pre-chamber in order to better discern the markings in low light conditions for the high-speed images

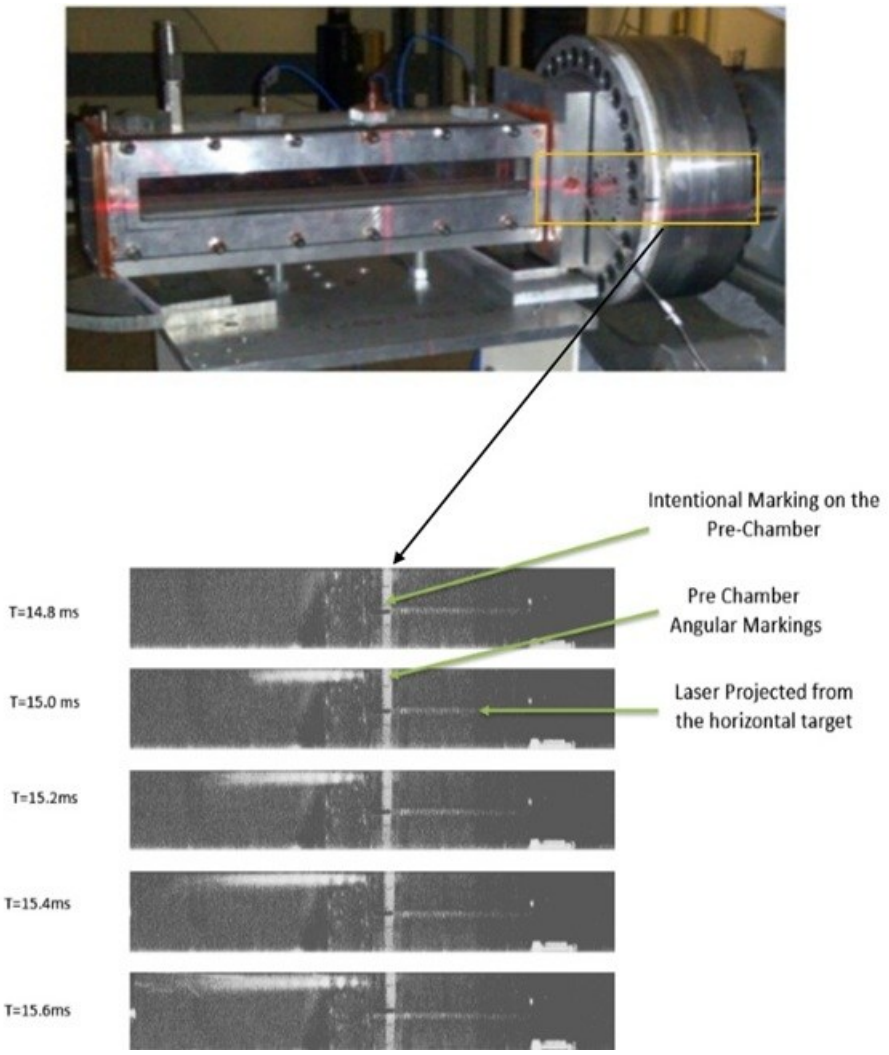

Figure 4. 6 High-speed video images (pre-chamber speed: 150 rpm) illustrating the result of adjustments made to ignition delay angle resulting in jet ejection at the required location. (The images are slightly enhanced for better clarity)

For the jet alignment experiments the exposure time and frame rate is maintained in the same manner as the regular ignition experiments. The location of the magnet in the pickup coil arrangement is varied until a satisfactory jet ejection location is attained. A successful configuration will result in high-speed images showing start of jet ejection when the pre-chamber marking and the laser target coincides as indicated in Figure 4.6. Diaphragm rupture and subsequent jet ejection before the nozzle alignment with the main chamber entrance should be avoided as it will result in loss of hot gas mass before it can

enter the main chamber mixture. The loss of ejected mass becomes significant at lower speeds of 150 rpm where the nozzle traverse speed is almost negligible compared to 1500 rpm.

4.1.4 Jet Traverse End

The event indicates the end of jet traverse as the nozzle sweeps past the main chamber entrance. Figure 4.7 indicates the location of the traversing nozzle at the traverse start and end time. The total time taken for complete traverse of the jet from one end of the main chamber to the other end for various pre-chamber speeds is indicated in Table 4.1. Ignition (when detected) always occurred at some time that fell in between the time of the start of translation and the end.

Figure 4. 7 Schematic illustrating the position of the nozzle at the start of jet traverse and at the end.

4.2 Ignition and Pressure Trace Analysis in the Main Chamber

4.2.1 Ignition and Ignition Delay Time

There are many definitions of ignition delay time used in the literature. Among various experiments, the definition of ignition delay time varies as much as the definition of ignition itself. Some of the variations are due to the measuring equipment and methods used, and some due to the physical variations of the experimental facility. In shock-ignition experiments the ignition time is measured from the instant when the shock wave reflects at the closed end of the driven section to the instant when combustible mixture appears to ignite, with shock arrival measured by pressure transducers [6, 54] and ignition determined using photomultipliers [54, 55] or the emission of specific species [6, 55]. Auto-ignition delay in shock-tube and rapid compression experiments reflect purely chemical processes, while jet ignition and spark ignition also include physical processes. Ignition delay in hot-jet ignition includes time for transient jet vortex development, jet mixing with the gas in the CVC chamber, and chemical induction time. In addition ignition is also affected by reflecting shock and expansion waves generated due to confined geometry of the CVC chamber.

Ignition (or self-ignition) is the onset of rapid combustion, results when a sufficient amount of energy is added to a flammable mixture of fuel and oxidizer [56, 57]. Ignition is also defined in terms of accompanying phenomena as sudden change in pressure, temperature and light emission [58, 59]. In the current study ignition is defined in terms of electromagnetic radiations captured in the visible spectrum caused by the re-ignition process of partially combusted hot-jet in the main chamber. Radiation of visible light was observed as ignition in other hot-jet ignition research conducted by [25, 26, 60, 61]. The ignition delay time for a hot jet-ignited constant volume combustor may be defined as the time from jet initiation to the occurrence of rapid, visible, and pressure-generating heat release in the CVC chamber [15].

Radiation from combustion products including the species and radicals from oxidation of methane, ethylene, and propane in shock tube experiments is emitted in the wavelength range of 185-800 nm. Soot radiation is emitted in the visible and infrared wavelength ranges [62, 63]. There are several other ignition predictors used in ignition delay studies. The CH* emission signal which has been simulated by assuming that it is proportion to the production rate of CH*, formed by the reaction $C_2H+O \rightarrow CH^*+CO$ and then rapidly quenched, is a good ignition predictor. When measured using a linear scale for CH* there is a single strong peak that can be identified with the ignition time. Pressure is a good indicator of ignition at high fuel concentrations. In lean cases, however, there is a small and almost immeasurable pressure rise, which renders the ignition indicator unsuitable for low concentration mixtures. Also signal to noise ratio in pressure measurements prevents its application as ignition indicator over a wide range of conditions [55]. OH is another good indicator of change owing to ignition. For the current study, ignition delay time is defined as elapsed time between the diaphragm rupture event and the detection of luminous region having intensity above a specified threshold limit in the main chamber. The high-speed camera captures luminosity emitted in the wavelength range of 400-1000 nm which also includes emissions by soot radiation during the combustion process.

For the hot-jet ignition study conducted in the CVC chamber, two separate events can be observed. One is the ignition initiation by the hot-jet and second is a self-sustained flame propagation across the main chamber length. Both the ignition and flame propagation events are affected by the reflecting pressure waves that are developed within the confined main chamber volume. Shock flame interaction is another complex phenomenon that affects the flame propagation speed and fuel consumption rate. Figure 4.8 gives a good visual of the various physical processes discussed hereby.

Ignition delay time definition used by Perera [15] included a condition that a visible flame front should be seen following ignition. However that criteria was not considered for this current study for successful ignition, as more emphasis was placed on ignition delay time and ignition locations. Moreover the lean mixtures studied indicated clear ignition

behavior but did not support a strong flame propagation except for slower nozzle traverse speed where the hot jet injection was rather continuous till the end of combustion in the main chamber. From the study conducted by Kito, S et al. [64] it was indicated that addition of active radicals to a leaner mixture had no part in improving the lower flammability limit of the main fuel-air mixture. It was the turbulent nature of the hot- jet that initiated ignition and burned the mixture at multiple points. Hence it is expected that past the ignition zones the flame would not sustain for a longer time and length for very dilute mixtures.

4.2.2 Image Processing

The temporal development of the hot-jet ignition process was studied using high-speed imaging. Video images of the jet in the main CVC chamber taken through a side window were captured at a resolution of 1632 × 104 at a frame rate of 10,000 per second (time interval between frames is 100 μs) with the lens aperture set to an f-number of 1:1.8. The exposure time is 96.75 μs, which was the maximum allowed for the set frame rate. EDR (Extreme Dynamic Range ™) exposure was turned off and set to 0 μs. EDR option is used to adjust exposure on pixel level to reduce over-exposure at certain regions due to bright spots. By setting EDR exposure time to 0 μs, the exposure level at the time of triggering the camera remains unaltered for the entire series of captured images. The high-speed images captured during ethylene oxidation by ignition through a hot-jet traversing at 0.983 m/s is presented in Figure 4.8. The first instance where the jet appears in the high-speed images is assumed as 0.2 ms from the diaphragm rupture time.

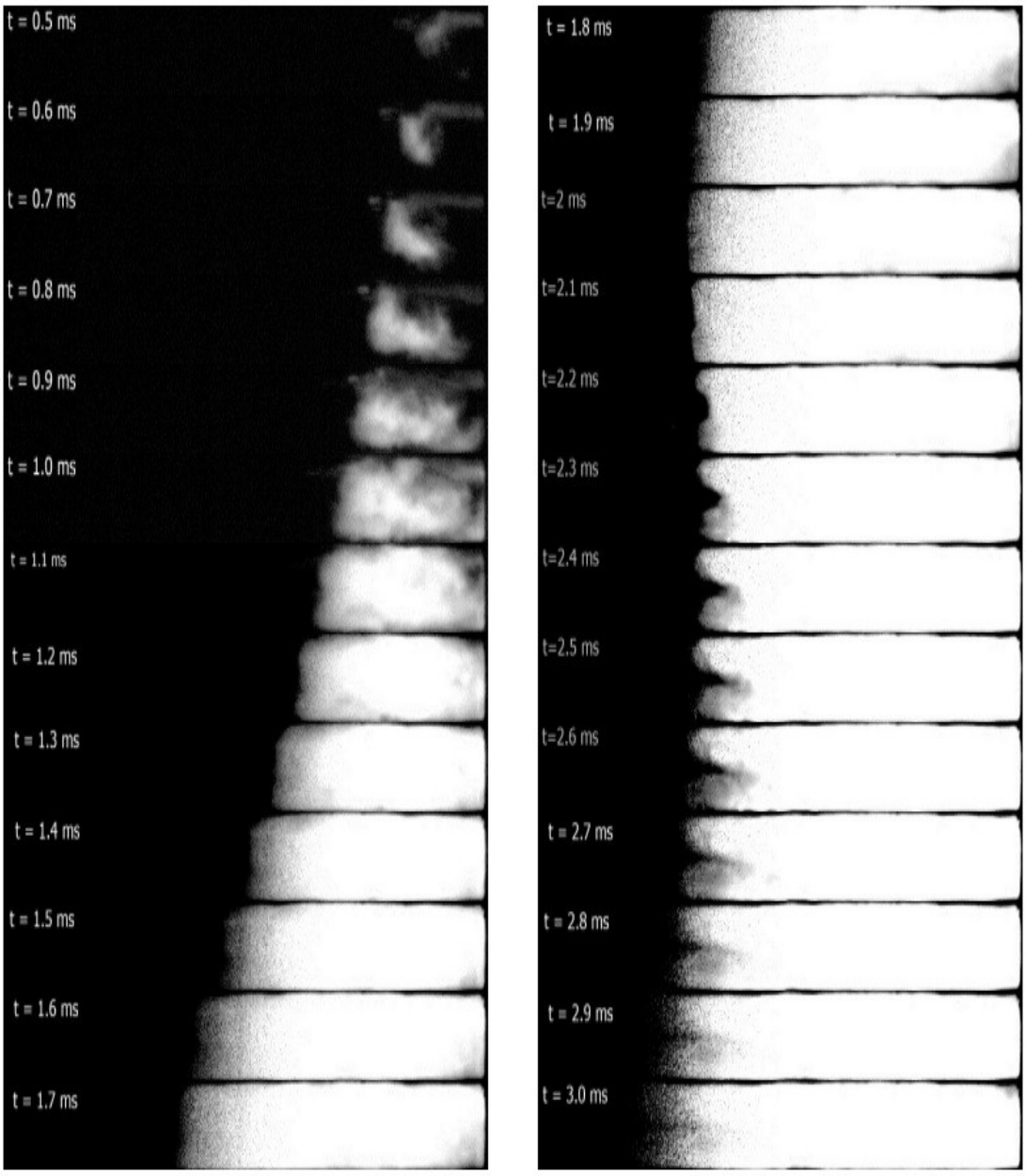

Figure 4. 8 Traversing hot-jet ignition process as observed from the optical window using high-speed imaging (From jet inception to combustion till 3 ms)

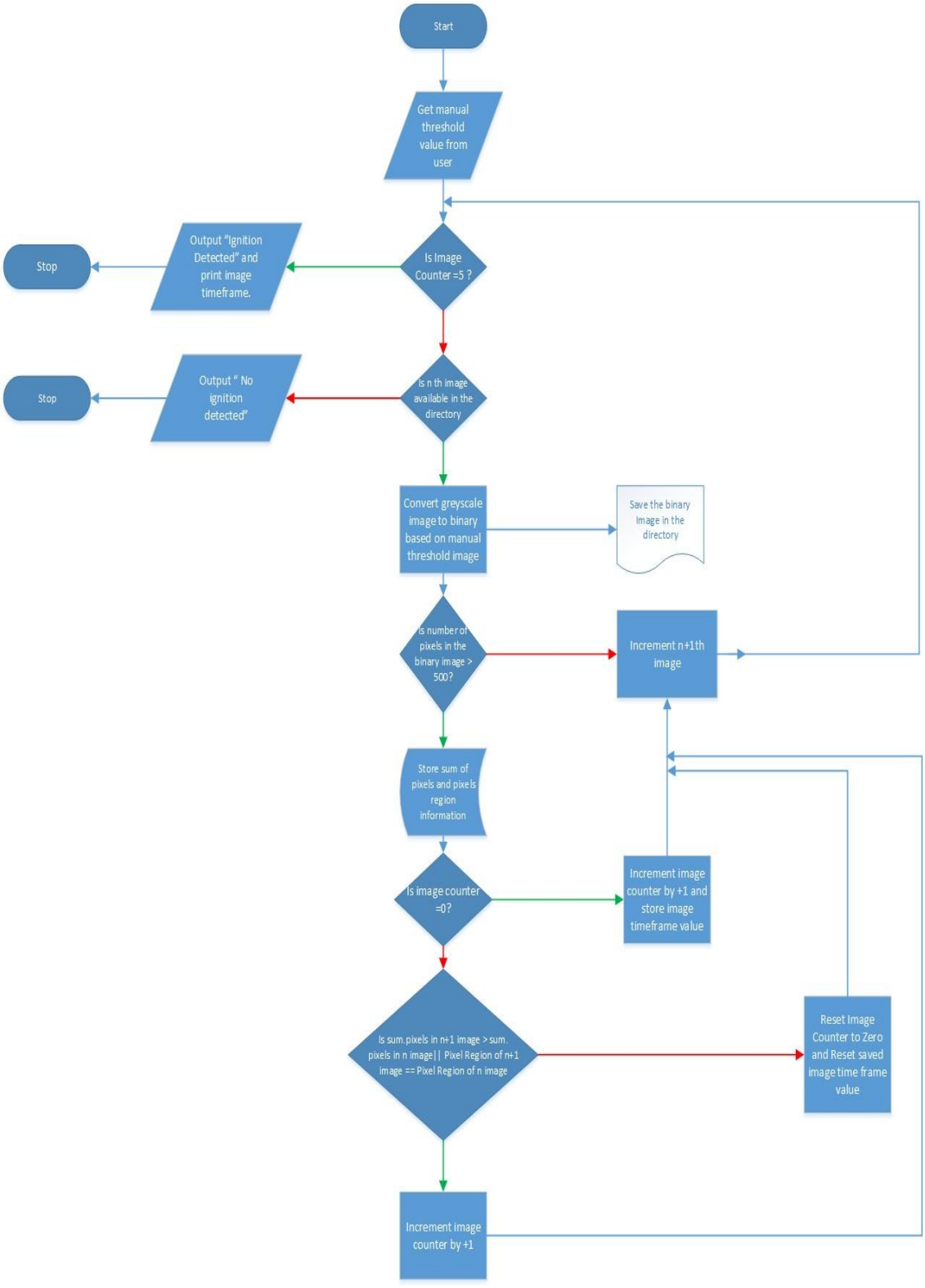

Figure 4. 9 Algorithm used for identifying ignition in the main chamber

An image processing code was written in MATLAB ^{TM} and applied using the Sobel edge-detection technique [65] to provide optimal edge detection for the current study. The high-speed images from each test were analyzed frame-by-frame for luminosity value at each pixel of the frame. The pixel values of the 8-bit monochrome camera output vary from 0 to 255. The threshold value for identification of ignition was set at 50% of the full-scale signal. The threshold value was chosen due to increased chemical activity near the nozzle region in this traversing hot-jet ignition study. The pixel luminosity value, number of pixels above the threshold per frame, and the location of pixels above the threshold were tracked on each frame. The image processing algorithm used is shown in Figure 4.9. The number of pixels and growth of the pixel area is tracked for subsequent frames to detect ignition.

The original grey scale images as captured using the high-speed camera and binary images processed using the code for ignition detection is compared for each test case to detect ignition, ignition sites and measure ignition delay time. In Figure 4.10 images are presented for methane mixture at $\Phi = 0.6$ with a nozzle traverse time of 40.6 ms. The images on the left corresponds to the original grey scale images as recorded by the high speed camera while the images on the right are image processed binary images. Ignition zones were identified at three different locations visible in a frame at t = 4.8 ms in the processed image. It is observed that these ignition zones continue to grow rapidly for the next 0.3 ms. The ignition at multiple regions in the main chamber is an important characteristic of jet ignition and has implications for the rate of combustion [53]. A second set of images corresponding to ethylene mixture at $\Phi = 0.4$ and a nozzle traverse time of 40.6 ms is presented in Figure 4.11. The maximum luminosity observed in the images is lower than that of the methane mixture with $\Phi = 0.6$ (Figure 4.10) due to dilution levels.

The existence of ignition regions above the threshold limit can be better discerned in the processed images when compared to the original images. As the ignition delay time is significantly different for the two fuels, the images have been presented over different time scales. Though the default criterion for successful ignition was set at 50% threshold limit the outcome of successful ignition was not changed when the threshold level was increased to 80%. However, ignition delay time measurements were made using a 10%

threshold as chosen by [15] to enable comparison with other stationary pre-chamber cases. Similarly Allocoa [66] used a 10% threshold limit to study flame pattern that starts after the injection event of E10 and E85 fuels in an IC engine. It has to be noted that for the 50% threshold limit when compared to the 10% limit only altered the outcome of successful ignition but the ignition delay time was not altered.

Figure 4.12 shows high-speed video images that are processed for edge detection indicating the boundary of the reaction zone. Edge detection is required to precisely define the boundary in the original images and can be further used to extract information on flame structures and apparent flame velocity from the captured image.

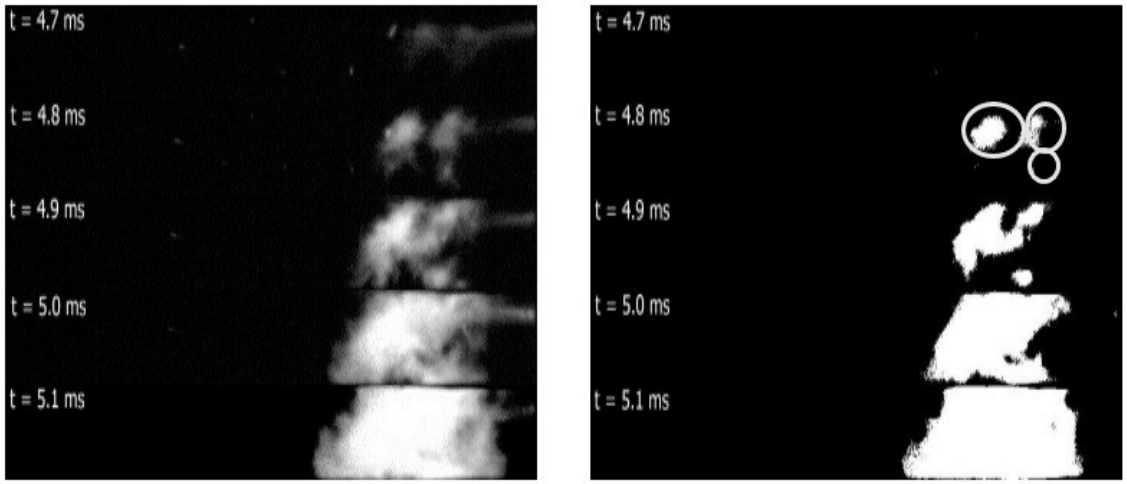

Figure 4. 10 Identification of ignition zones and subsequent growth (fuel: methane at Φ = 0.6, nozzle traverse time = 40.6 ms). Ignition zones are circled at t = 4.8ms.

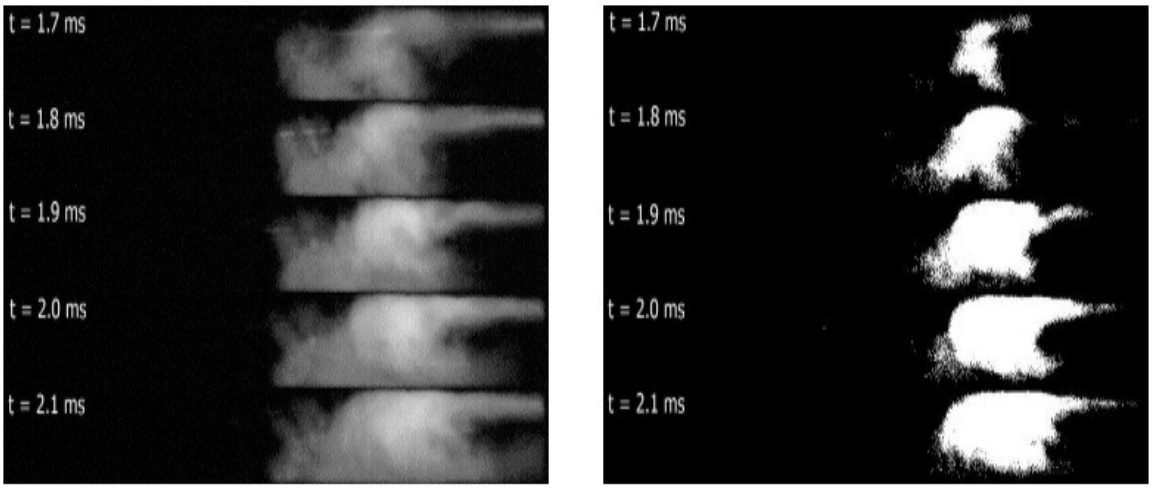

Figure 4. 11 Identification of ignition zones and subsequent growth (fuel: ethylene at Φ = 0.4, nozzle traverse time = 40.6 ms)

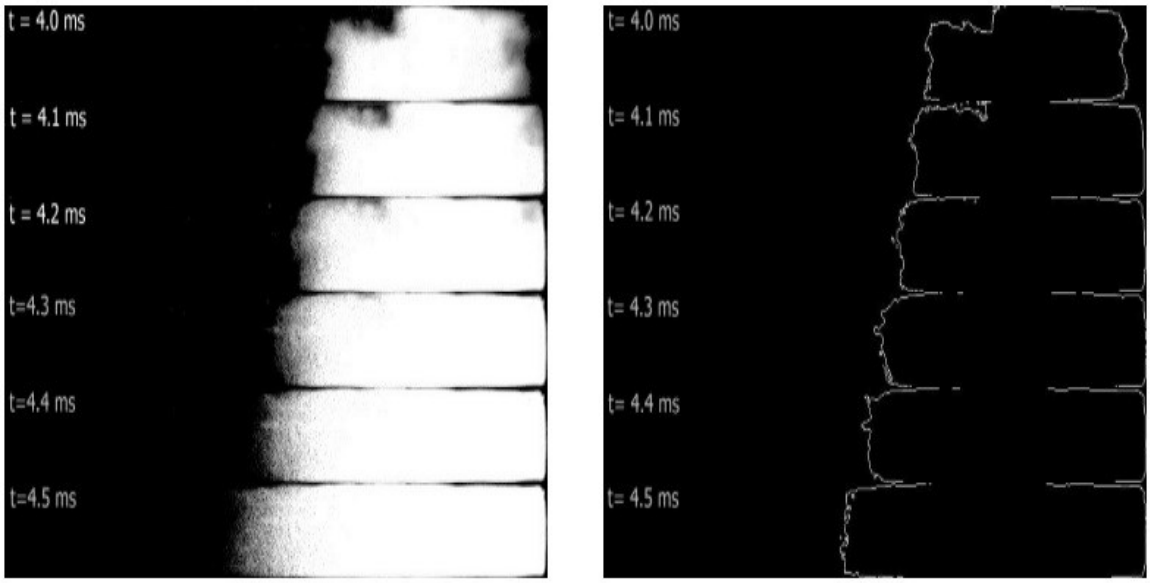

Figure 4. 12 Flame edge detection by image processing for hydrogen-enriched methane mixture at Φ = 0.8 nozzle traverse time of 40.6 ms.

4.2.3 Pressure Trace Analysis in Main Chamber

The ignition pressure rise is determined by the energy release rate of the ignition process. Two preliminary experiments were conducted with a nozzle traverse time of 8.1 ms which corresponds to a pre-chamber rotation speed of 750 rpm. Ethylene was used as a fuel at different equivalence ratios in the chambers as dictated by the initial conditions required. The summary of initial conditions are given in Table 4.2. Test case 2 is a fuelled case as there was fuel in the main chamber while in test case 1 the main chamber was filled with air at atmospheric pressure.

Table 4. 2 Initial conditions of test cases used for pressure trace analysis

Test Number	Pre-Chamber equivalence ratio, Φ	Main-Chamber equivalence ratio, Φ(fuel)	Nozzle Traverse Time, ms	Main Chamber pressure (max) ,psig
1	1.1	0.8(Ethylene)	8.1 ms	50
2	1.1	0	8.1 ms	21

These tests were performed to evaluate the response of pressure transducer PT1, PT2 and PT3 for a case with pronounced ignition and flame propagation and to compare it against a case where was there was no fuel in the main chamber to cause any pressure rise. It has be observed that the pressure history for test 2 is purely due to the effects of issuing a high-speed compressible jet into a closed volume.

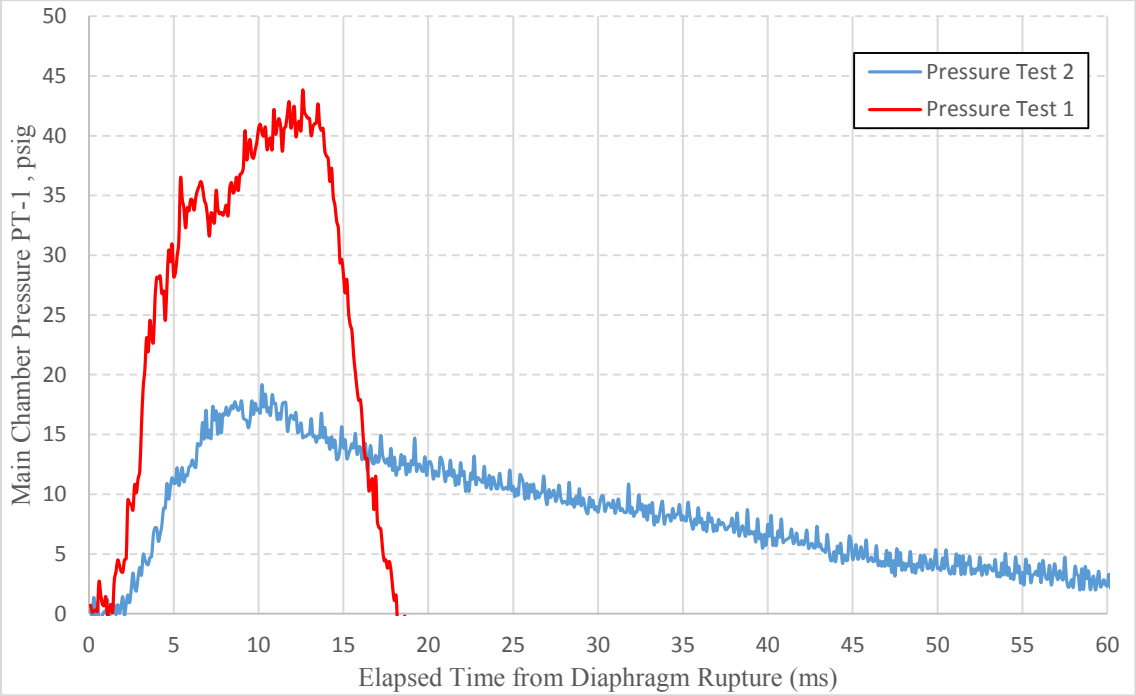

Figure 4. 13 Comparison of pressure traces recorded from PT1 for an ignition (Test1) and no ignition (Test2) case in the main chamber

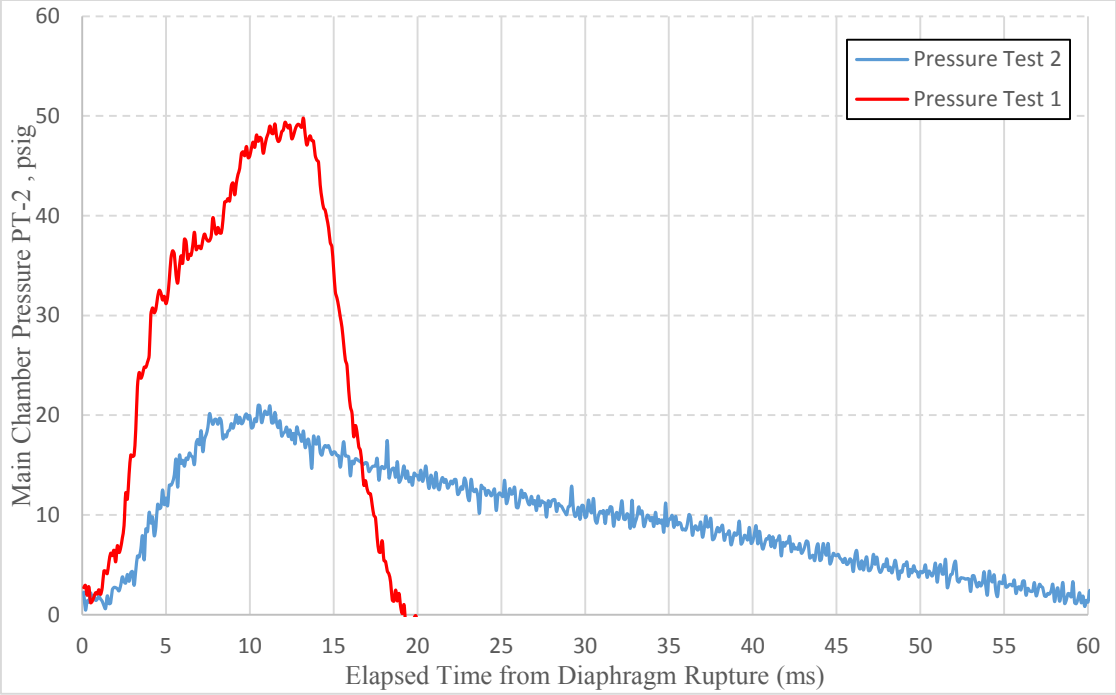

Figure 4. 14 Comparison of pressure traces recorded from PT2 for an ignition (Test1) and no ignition (Test2) case in the main chamber

The change owing to pressure rise due to ignition in the main chamber is clearly captured in the pressure traces in Figure 4.13, 4.14 and 4.15. The transducer responds with a sharp increase in the rate of pressure rise when the ignition occurred while the trace for no ignition case is flat and laid out. The maximum pressure recorded for test case 2 is 21 psig. This limit of 21 psig when there was no fuel in the main chamber can be used to compare the pressure rise occurring due to burning dilute mixtures in the main chamber. The temporal variations in the pressure traces are clear indicators of changes owing to ignition. The only limitation is with respect to the spatial location of ignition that can happen when ignition occurs near or in-between the pressure transducer locations and there could a finite delay in the pressure response before this change can be felt in the location of the pressure transducer. Figure 4.16 and Figure 4.17 compares all 3 pressure transducers response for the same test case.

The PT2 records a higher peak compared to PT1 and PT3 for both the ignition and no ignition case. There can be several reasons for the difference in pressure time history recorded by these transducers. Pressure waves travel at the speed of sound. Assuming high temperature combustion products as air at 1800 K, the speed of sound is estimated as 820 m/s. The distance between the transducers is 4 inches, hence the pressure waves can reach across the transducer locations in one-tenth of a millisecond. From Appendix C, it can be noted that the 'rise-time' which is the interval required by the output signal of a pressure sensor to display a change in the applied pressure, is less than 1 μs. Hence the distance between the transducers or the response time of the transducers is not a limiting factor in the current setup that could have cause pressure disparity after ignition.

In Figures 5.8 – 5.12 it can be observed that as the peak pressure goes higher there is a rapid fall in pressure compared to the pressure trace of the no-combustion case. This can be due to high leakage rate between the pre-chamber face and main chamber entrance due to high pressure generated during combustion. Another important factor to be considered is the effect of thermal shock on piezoelectric transducers. The thermal shock experienced by the transducers is due to the effect of hot combustion gases passing over the pressure sensor's diaphragm. Virtually all pressure sensors are sensitive to thermal shock. When heat strikes the diaphragm of a piezoelectric sensor that has quartz crystals contained in an outer housing, the heat can cause expansion of the housing. This expansion induces reduction in the preload force on the crystals, making it create a negative signal output accompanied with a rapid reduction in pressure curve obtained. The pressure response difference in PT2 could be due to any of these phenomenon or due to a combination of them which requires further investigation.

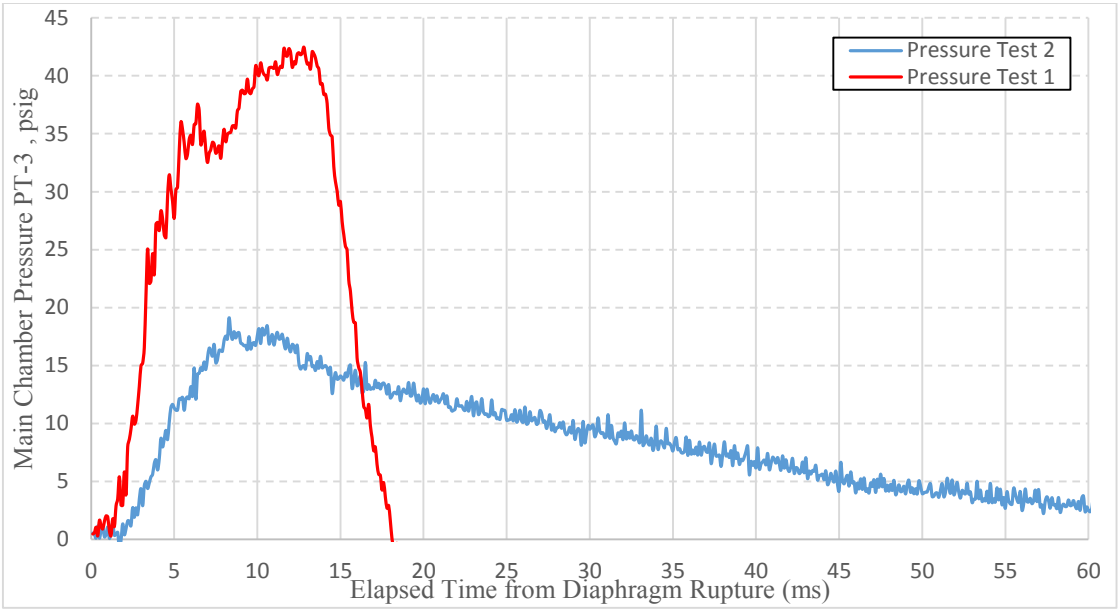

Figure 4. 15 Comparison of pressure traces recorded from PT3 for an ignition (Test1) and no ignition case in the main chamber

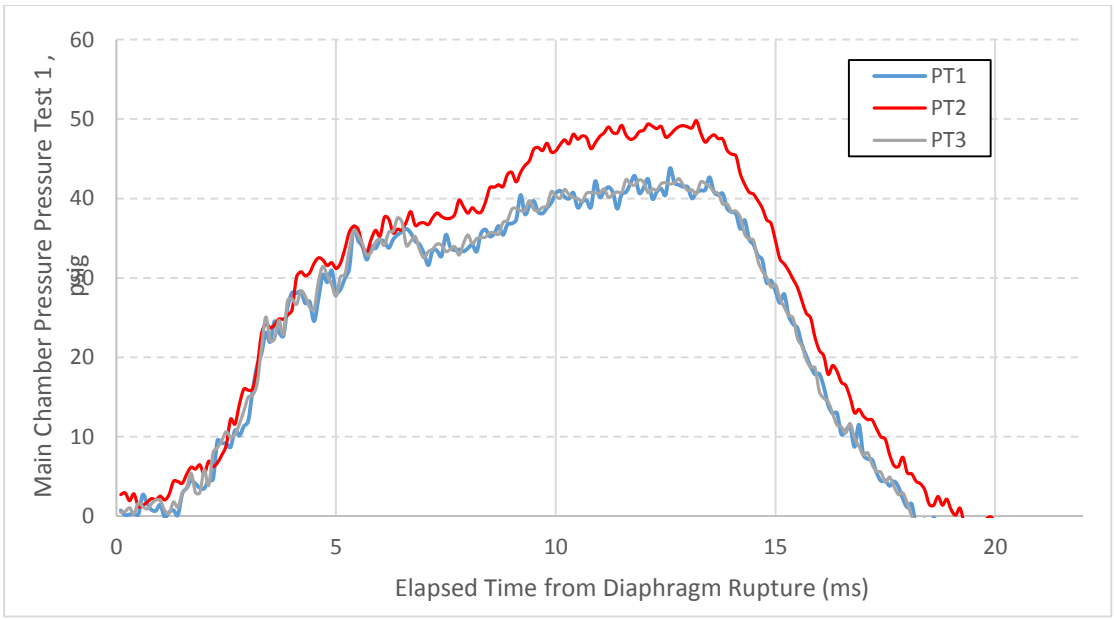

Figure 4. 16 Comparison of pressure traces recorded from PT1, PT2 and PT3 for an ignition case in main Chamber

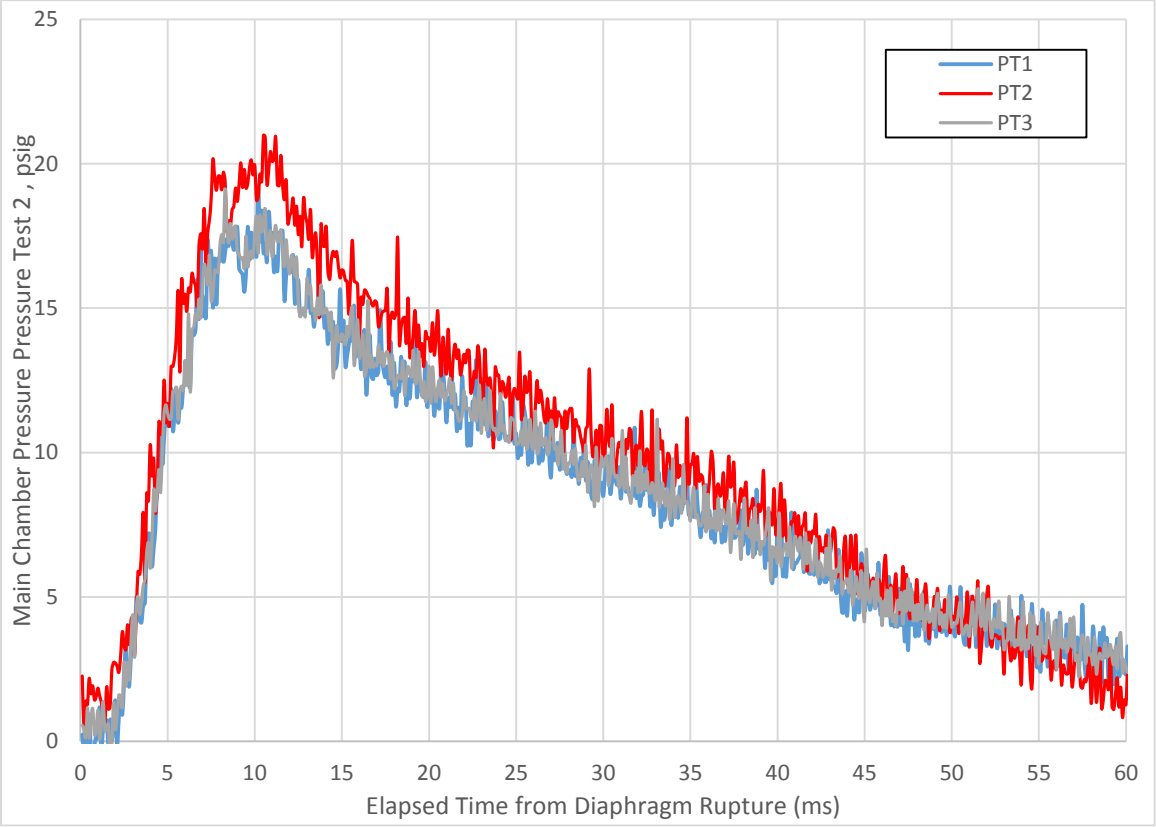

Figure 4. 17 Comparison of pressure traces recorded from PT1, PT2 and PT3 for a no ignition case in main Chamber

5. RESULTS AND DISCUSSIONS

The chapter reports and discusses the results obtained by observing the ignition behavior for three different fuels ethylene, methane and hydrogen-methane blend at lean equivalence ratios of 0.8, 0.6 and 0.4. These mixtures are ignited by a hot-jet traversing at five different speeds as mentioned in Table 4.1. The jet traverse starts from the top wall of the CVC chamber and continues till it moves past the bottom wall. High-Speed images presented in this chapter shows the hot-jet injected from the left side where the nozzle is located as illustrated graphically in Figure 4.7. For low traverse speed (40.6 ms traverse time), the jet remains attached to the wall of the CVC chamber and hence referred to as 'near wall jet' which later behaves as a wall impinging jet as discussed in Chapter 2. As explained with Figure 2.5, the penetration of the traversing jet is mainly governed by the vortices that are generated during the injection process. For the case of 'near wall jet', the injected hot jet initially moves along the top wall. Later the jet turns and proceeds towards the bottom wall of the CVC chamber due to creation of vortices and jet expansion effects, hence taking a path of least resistance. This causes the jet to impinge at the bottom wall which in turn dictates the jet penetration and mixing characteristics. This phenomenon will be illustrated with high-speed images in the following chapter although the vortices are not visible due to the current imaging setup. There is no significant effects expected due to gravity interaction on the jet.

For each test point, ignition is controlled by three parameters: main chamber fuel, main chamber equivalence ratio, and jet traverse speed. Each test case is repeated thrice to get an understanding on ignition delay time variation for same initial conditions in the main chamber. The repeated tests indicated overall consistent jet penetration pattern and ignition behavior. Only few tests were possible at a pre-chamber speed of 1500 rpm due to hardware limitations which will be discussed later in this chapter. The ignition delay time variation with respect to fuel type, equivalence ratio, and traverse speed has been discussed by supporting graphs. Methane-air mixtures exhibited the highest ignition delay time while ethylene-air mixtures had the lowest ignition delay time. Hydrogen blended methane-air mixtures exhibited ignition delay times which fell between the other two fuels investigated. Complete set of tests conducted for this study with the recorded ignition delay data is shown in Table 5.1 – 5.3. The test set numbers are labelled with the format: Fuel - Equivalence ratio - Nozzle traverse time - Test iteration number such that E-0.8-40.6-1 refers to test conditions with ethylene as main chamber fuel maintained at 0.8 equivalence ratio ignited by a jet traversing in 40.6 ms during the first test iteration.. Entries in the table indicating 'NA' are the experimental cases where no ignition was detected.

High-speed images presented in this chapter have unequal time intervals along the sequence while proceeding downwards and while comparing left to right. Frames where there were no significant ignition behavior or no noticeable flow features have been skipped. Generally tests conducted with ethylene as main chamber fuel showed good jet penetration path during the time of jet injection. Cases where methane and hydrogen blended methane were used as main chamber fuel showed no clear jet penetration path, hence images until or before ignition delay times were mostly dark. Thereby only frames closer to the ignition delay time will be presented for methane and hydrogen blended methane. Comparison has also been made across the tested fuels at different nozzle traverse speeds. The high-speed images are supplemented with pressure traces, an important indicator of the heat release process due to fuel oxidation.

Table 5.1 Ignition delay time for ethylene-air mixtures across different equivalence ratio and nozzle traverse time (Test Set Number: Ethylene - Φ - Traverse time - Iteration)

Test Set Number	Ignition Delay Time (ms)	Test Set Number	Ignition Delay Time (ms)	Test Set Number	Ignition Delay Time (ms)	Test Set Number	Ignition Delay Time (ms)	Test Set Number	Ignition Delay Time (ms)
E-0.8-40.6-1	1.9	E-0.8-8.1-1	0.6	E-0.8-6.1-1	1	E-0.8-4.9-1	2.2	E-0.8-4.1-1	2
E-0.8-40.6-2	1.3	E-0.8-8.1-2	1.5	E-0.8-6.1-2	0.9	E-0.8-4.9-2	2.7	E-0.8-4.1-2	-
E-0.8-40.6-3	1.3	E-0.8-8.1-3	1	E-0.8-6.1-3	1.5	E-0.8-4.9-3	1.7	E-0.8-4.1-3	-
E-0.6-40.6-1	1.8	E-0.6-8.1-1	0.8	E-0.6-6.1-1	1.6	E-0.6-4.9-1	25	E-0.6-4.1-1	NA
E-0.6-40.6-2	1.5	E-0.6-8.1-2	2.3	E-0.6-6.1-2	1.9	E-0.6-4.9-2	20	E-0.6-4.1-2	-
E-0.6-40.6-3	1.6	E-0.6-8.1-3	1.6	E-0.6-6.1-3	0.9	E-0.6-4.9-3	20	E-0.6-4.1-3	-
E-0.4-40.6-1	1.8	E-0.4-8.1-1	1.5	E-0.4-6.1-1	NA	E-0.4-4.9-1	NA	E-0.4-4.1-1	NA
E-0.4-40.6-2	1.7	E-0.4-8.1-2	2.4	E-0.4-6.1-2	NA	E-0.4-4.9-2	NA	E-0.4-4.1-2	-
E-0.4-40.6-3	3.8	E-0.4-8.1-3	3.1	E-0.4-6.1-3	NA	E-0.4-4.9-3	NA	E-0.4-4.1-3	-

Table 5.2 Ignition delay time for methane-air mixtures across different equivalence ratio and nozzle traverse time (Test Set Number: Methane - Φ - Traverse time- Iteration)

Test Set Number	Ignition Delay Time (ms)	Test Set Number	Ignition Delay Time (ms)	Test Set Number	Ignition Delay Time (ms)	Test Set Number	Ignition Delay Time (ms)	Test Set Number	Ignition Delay Time (ms)
M-0.8-40.6-1	4.1	M-0.8-8.1-1	3.7	M-0.8-6.1-1	1.5	M-0.8-4.9-1	2.6	M-0.8-4.1-1	NA
M-0.8-40.6-2	4.5	M-0.8-8.1-2	3.6	M-0.8-6.1-2	1.9	M-0.8-4.9-2	3	M-0.8-4.1-2	-
M-0.8-40.6-3	5.8	M-0.8-8.1-3	3.8	M-0.8-6.1-3	1.5	M-0.8-4.9-3	2.2	M-0.8-4.1-3	-
M-0.6-40.6-1	4.8	M-0.6-8.1-1	2.6	M-0.6-6.1-1	2	M-0.6-4.9-1	2.9	M-0.6-4.1-1	NA
M-0.6-40.6-2	3.4	M-0.6-8.1-2	3.4	M-0.6-6.1-2	1.7	M-0.6-4.9-2	2.4	M-0.6-4.1-2	-
M-0.6-40.6-3	4.2	M-0.6-8.1-3	2.9	M-0.6-6.1-3	1.8	M-0.6-4.9-3	2.2	M-0.6-4.1-3	-
M-0.4-40.6-1	3.2	M-0.4-8.1-1	2.7	M-0.4-6.1-1	NA	M-0.4-4.9-1	NA	M-0.4-4.1-1	NA
M-0.4-40.6-2	3.6	M-0.4-8.1-2	3.6	M-0.4-6.1-2	NA	M-0.4-4.9-2	NA	M-0.4-4.1-2	-
M-0.4-40.6-3	3.1	M-0.4-8.1-3	3.1	M-0.4-6.1-3	NA	M-0.4-4.9-3	NA	M-0.4-4.1-3	-

Table 5.3 Ignition delay time for hydrogen blended methane-air mixtures across different equivalence ratio and nozzle traverse time (Test Set Number: Blend (CH_4 - H_2) - Φ - Traverse time - Iteration)

Test Set Number	Ignition Delay Time (ms)	Test Set Number	Ignition Delay Time (ms)	Test Set Number	Ignition Delay Time (ms)	Test Set Number	Ignition Delay Time (ms)	Test Set Number	Ignition Delay Time (ms)
B-0.8-40.6-1	3.6	B-0.8-8.1-1	2.6	B-0.8-6.1-1	2.3	B-0.8-4.9-1	2.2	B-0.8-4.1-1	1.6
B-0.8-40.6-2	2.7	B-0.8-8.1-2	3.1	B-0.8-6.1-2	1.7	B-0.8-4.9-2	2.2	B-0.8-4.1-2	-
B-0.8-40.6-3	2.7	B-0.8-8.1-3	2	B-0.8-6.1-3	1.7	B-0.8-4.9-3	1.7	B-0.8-4.1-3	-
B-0.6-40.6-1	2.6	B-0.6-8.1-1	2	B-0.6-6.1-1	1.5	B-0.6-4.9-1	2.4	B-0.6-4.1-1	NA
B-0.6-40.6-2	2.6	B-0.6-8.1-2	2	B-0.6-6.1-2	1.7	B-0.6-4.9-2	1.5	B-0.6-4.1-2	-
B-0.6-40.6-3	2.3	B-0.6-8.1-3	1.7	B-0.6-6.1-3	1.7	B-0.6-4.9-3	2.4	B-0.6-4.1-3	-
B-0.4-40.6-1	2.4	B-0.4-8.1-1	2.7	B-0.4-6.1-1	NA	B-0.4-4.9-1	2.6	B-0.4-4.1-1	NA
B-0.4-40.6-2	3.5	B-0.4-8.1-2	3.6	B-0.4-6.1-2	1.3	B-0.4-4.9-2	NA	B-0.4-4.1-2	-
B-0.4-40.6-3	3.2	B-0.4-8.1-3	3.1	B-0.4-6.1-3	1.3	B-0.4-4.9-3	2.3	B-0.4-4.1-3	-

5.1 Ignition Behavior of Ethylene-Air Mixtures

Ethylene is a fuel of interest for some propulsion applications and is considered as a model gaseous fuel that has been selected for fundamental combustion studies [54, 67]. Although it is a fairly reactive gaseous hydrocarbon that is not by itself a very practical fuel, it is a significant constituent of certain practical fuels and an important decomposition product of many primary liquid fuels. The ignition of ethylene at room temperature can be considered as a surrogate for ignition of other hydrocarbons at higher temperature. Although the burning velocities, autoignition rates, and detonability of ethylene are less than those of acetylene, they are greater than those of most hydrocarbon fuels, including the more practical liquid fuels.

Tests carried out with ethylene as main chamber fuel provided good insight on jet penetration, jet travel path and related fluid dynamics up until the point of ignition. The quiescent main chamber mixture helped in eliminating any disturbances caused during jet penetration due to presence of gas motion in the main chamber. While richer mixture provided good insight on ignition and subsequent flame propagation, leaner mixtures with higher ignition delay times allowed capturing the jet flow physics. Reaction pathways through which the primary ethylene molecule breaks down is given below in a simplified manner to provide a general idea about the molecules and radicals that can initiate breakdown of the ethylene molecule.

$$C_2H_4 + M \rightarrow C_2H_2 + H_2 + M \qquad 5.1$$

$$C_2H_4 + M \rightarrow C_2H_3 + H + M \qquad 5.2$$

$$2C_2H_4 \rightarrow C_2H_3 + C2H_5 \qquad 5.3$$

$$C_2H_4 + O \rightarrow CH_4CHO + H \qquad 5.4$$

$$C_2H_4 + O \rightarrow CH_3 + CHO \qquad 5.5$$

$$C_2H_4 + O_2 \rightarrow C_2H_3 + HO_2 \qquad 5.6$$

$$C_2H_4 + HO_2 \rightarrow C_2H_4O + OH \qquad 5.7$$

$$C_2H_4 + H \rightarrow C_2H_3 + H_2 \qquad 5.8$$

$$C_2H_4 + OH \rightarrow C_2H_3 + H_2O \qquad 5.9$$

Figure 5.1 provides side-by-side comparison of the ignition behavior of ethylene-air mixtures with an equivalence ratio of $\Phi = 0.8$ at two different nozzle traverse speeds. Test number is indicated in the images since each condition was tested thrice. As seen from the images, the two tests exhibited different ignition behavior and ignition delay times with the only variable being the nozzle traverse time. As could be observed in these images, the ignition usually occurs along the visible edge at the bottom or tip of the jets and then proceeds along the shear layers. The heat transfer along the turbulent shear layers is usually very minimal as indicated by the studies conducted by Broadwell [68]. These ignition sites that are perceived to occur along the tip of jet are controlled by the vortices that develops during the injection process. A discussion regarding the development of vortices was made in Chapter 2. The injection pressure being fairly consistent across tests, the translating motion of the hot jet controls these vortices formation across different nozzle traverse speeds.

Due to the extended ignition delay time for the case of 40.6 ms nozzle traverse time, in Figure 5.1(left) the jet penetrating further is visible. Ignition zone is recorded at a distance of 150.1mm from main chamber entrance. The 40.6 ms traverse time which corresponds to 150 rpm pre-chamber rotation speed is the lowest nozzle speed attempted in this study. Figure 5.1(right) with a faster jet traverse speed indicates ignition as early as 0.6 ms. Here at $t = 0.5$ ms the jet has just started to enter the visible portion of the main chamber. At $t = 0.6$ ms, the jet had started to take a downward path behaving more like the jet with 40.6 ms nozzle traverse time. After ignition; rapid combustion occurs which creates a self-sustained flame propagation event which initially consumes the mixture on the right side of the chamber and then continues to propagate along the length of the tube as is shown in Figure 4.7.

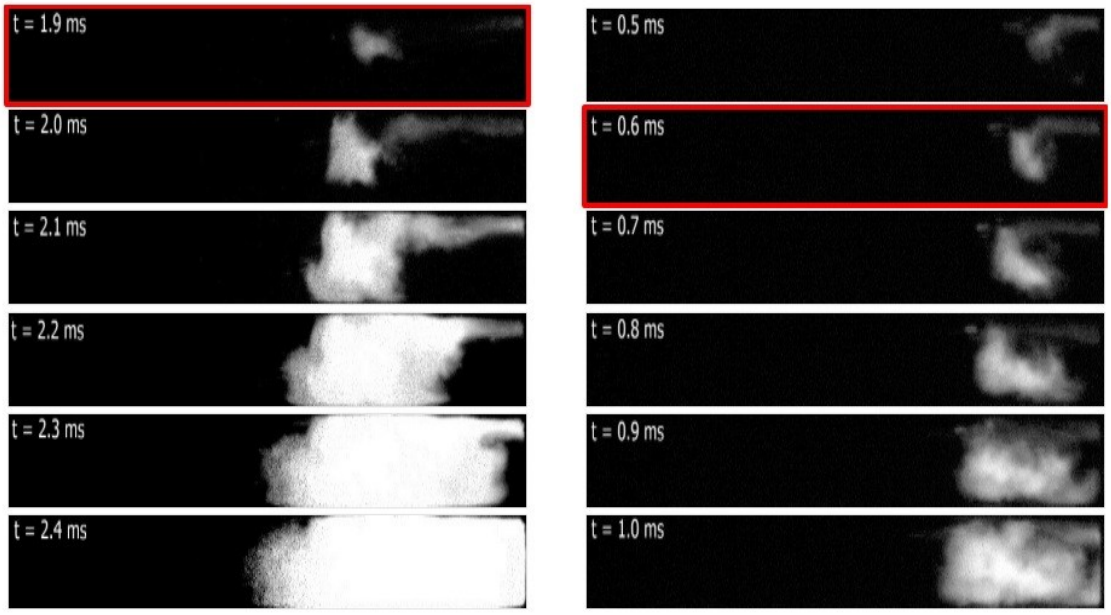

Figure 5. 1 Ignition of Φ = 0.8 ethylene-air mixtures, for hot-jet traverse time of 40.6 ms- E-0.8-40.6-1 (left) and 8.1 ms- E-0.8-8.1-1 (right). Red border indicates frame of ignition detection.

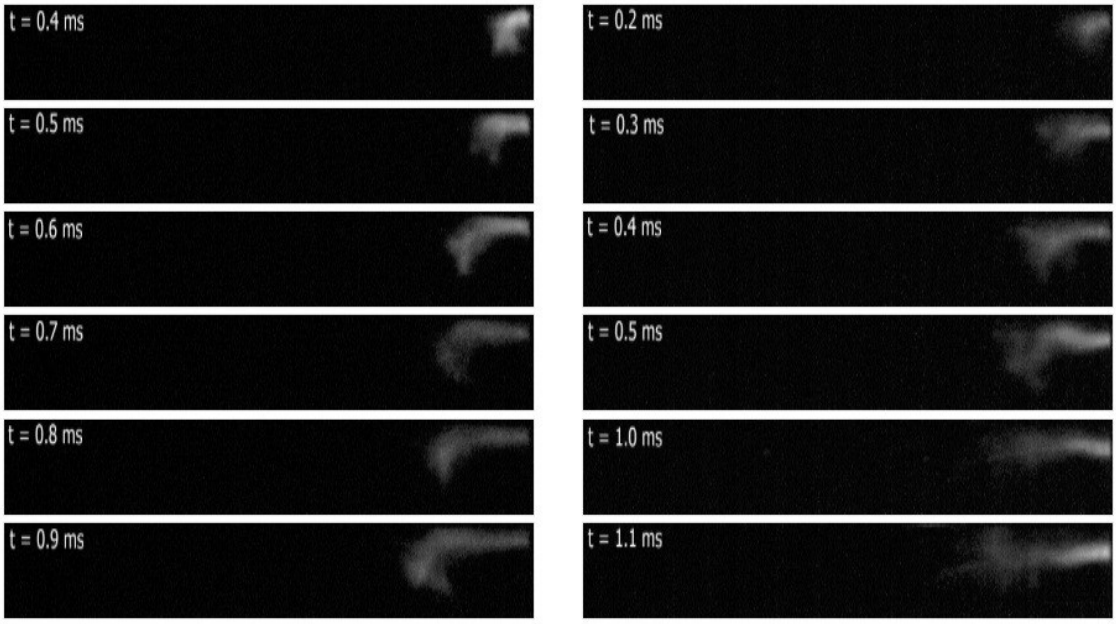

Figure 5. 2 Traversing jet penetration before ignition for Φ = 0.4 ethylene-air mixtures for hot-jet traverse time of 40.6 ms- E-0.4-40.6-1 (left) and 8.1 ms- E-0.4-8.1-1 (right)

Due to the extended ignition delay time for Φ = 0.4 and increased exothermic activity along the jet for ethylene-air mixtures in Figure 5.2 the nature of jet penetration can be observed as the jet traverses through the main chamber. For 40.6 ms nozzle traverse time, the jet barely moves from its initial location and behaves more like a stationary offset jet, which initially travels along the top wall and later impinges on the bottom wall as observed in the results Figure 2.17 d. At t = 0.5 ms, the jet traversing at 8.1 ms penetrates twice as far as the jet traversing at low speed which is due to the restriction for the motion of the jet along the walls and the path taken by the jet during the time frame shown in the images. The penetration achieved by the slower moving jet increases with time to a greater extent since the nozzle location is stationary. Although the 8.1 ms jet path looks straight, all the jets initially takes on the wall impinging path as it moves along the top wall of the CVC chamber. This is because the start of jet ejection is timed to occur at or before the instant when the nozzle becomes completely exposed to the main chamber entrance, and thus the nozzle directs the jet along the top wall at the start of the traverse. This behavior will be revealed and supported by images shown later in the chapter.

Figure 5.3 comparing Φ = 0.6 mixtures at t = 1.6 ms reveals higher penetration distance by the slower moving jet compared to a jet traversing at 6.1 ms. The maximum penetration distance of the jet is controlled by the nozzle position, its traverse speed and the injection pressure. The total mass injected within time of 6.1 ms can be estimated as 1×10^{-4} kg, considering air injected at 1800 K through the 6 mm nozzle exit under choked conditions. Considering an ignition delay time of 1.7 ms the mass of hot-gas injected remains constant for both the nozzle traverse speeds till the time of ignition. Figure 5.3 (left) indicates multiple ignition sites at t = 1.9 ms. It appears as if ignition evolved from sites of a pair of counter rotating vortices that evolved along the edge of the impinged jet as shown in Figure 2.4 . The ignition occurred at a distance of 188.1 mm compared to 139.6 mm for 6.1 ms jet. Figure 5.3 (right) at t = 1.5 ms, the instance when ignition occurs, it appears as if the jet is still taking on a wall impinging path. But subsequent images reveal how further ignition is governed due to the change in jet path due to increased nozzle traverse speed. Apart from the luminosity detected due to ignition, in Figure 5.3 few

particles can be seen further left from the ignition sites. These bright particles are created due to rupturing of aluminum diaphragm. These particles did not interfere in the ignition process as observed from the high-speed images.

Figure 5.4 compares two tests performed at $\Phi = 0.8$ and $\Phi = 0.6$ for ethylene-air mixtures at same nozzle traverse speed. The ignition behavior, ignition time, and subsequent flame propagation remains very similar across the two tests even though the fuel gets leaner. The tests reveal that ethylene is able to combust with very low combustion variability across tests even with a reduced equivalence ratio. It also highlights the hot-jet ignition potential to maintain consistent combustion and tolerance in terms of variation in fuel dilution levels.

Figure 5.5 & Figure 5.6 indicates ignition of $\Phi = 0.8$ ethylene-air mixtures ignited by jet traversing at 40.6 ms, 8.1 ms, 6.1 ms and 4.1 ms respectively. As discussed previously, the jet initially takes on a wall impinging path as the injection starts closer to upper wall of main chamber, hence very similar ignition behavior with respect to ignition zone location is observed across these tests. The last case shown (Figure 5.6 - left) is a 4.1 ms nozzle traverse time case corresponding to 1500 rpm pre-chamber speed, the highest speed attempted in this study. An ignition was barely detected in this case and the positive detection was clearly not due to luminosity of the jet itself (jet luminosity errors were removed by choosing 50% detection threshold limit). Due to the higher nozzle speed and the recorded delay time, ignition occurred near to the lower end of the wall corresponding to the location of the nozzle at that instance. No subsequent flame propagation was recorded after the ignition in this case.

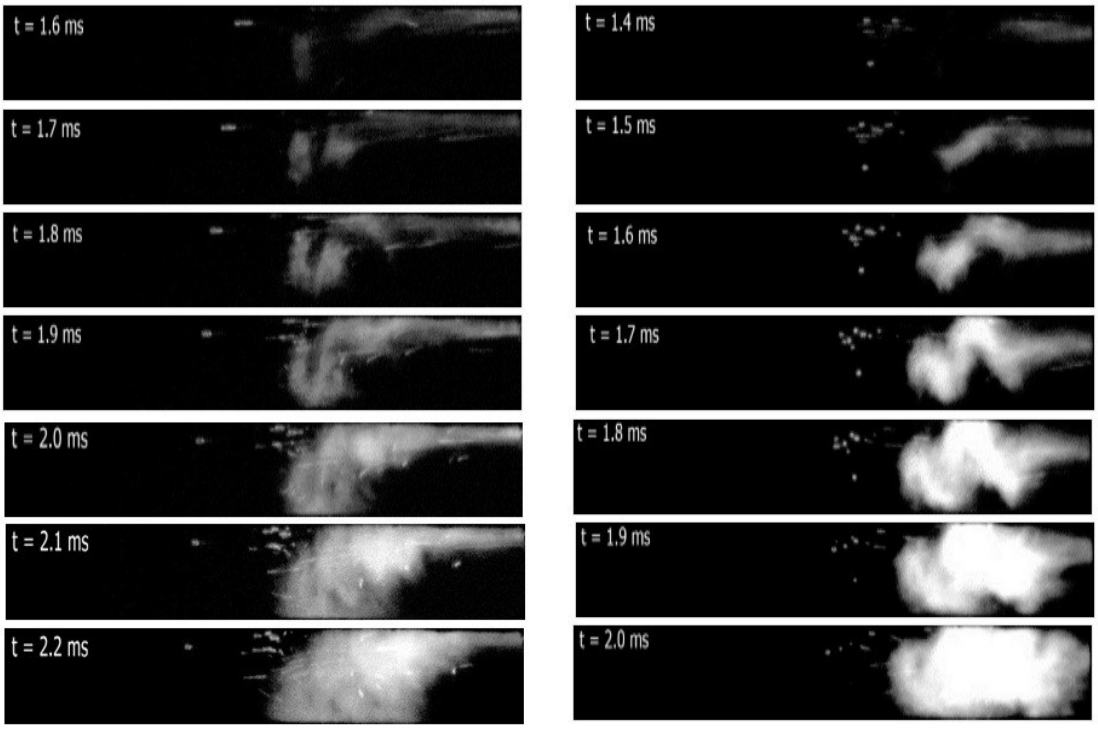

Figure 5. 3 Traversing jet ignition of Φ = 0.6 ethylene-air mixtures for hot-jet traverse time of 40.6 ms - E-0.6-40.6-3 (left) and 6.1 ms - E-0.6-6.1-1 (right)

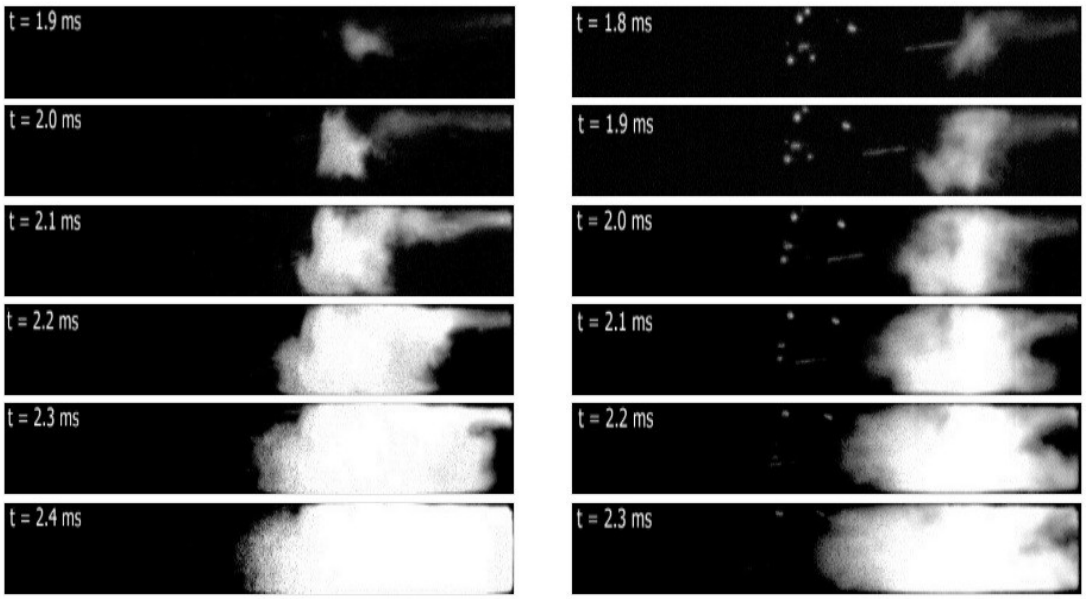

Figure 5. 4 Ignition of ethylene-air mixtures for hot-jet traverse time of 40.6 ms at Φ = 0.8 - E-0.8-40.6-1 (left) and Φ = 0.6 - E-0.6-40.6-1 (right).

For the nozzle traverse time of 4.1 ms the jet traverse time is more than the ignition delay time observed in any of the of the ethylene-air mixtures. Although the amount of hot jet mass injected can be adequate to create a strong ignition for the ethylene mixture at Φ = 0.8, a weak ignition event with no flame propagation was revealed in the high-speed images. Possible reasons for this behavior include that the moving ignition source not being able to create one or more localized zones that have the energy and sufficient entrapped fuel-air mixture to create ignition. The faster traverse speed jets injects less hot gas mass into the primary vortices that are initially created, as the jet moves away and creates other new vortices. There may be a reduction of angular momentum in the vortices generated reducing its capability to trap more mass from the fresh charge. Ethylene at Φ = 0.8 is the most reactive mixture with the least ignition delay time examined in this study and a very weak ignition behavior at for 4.1 ms traverse time indicates that the current CVC chamber does not support ignition past 1250 rpm.

Similarly for an another set of tests conducted in this study where H_2-CH_4 mixture was used as main chamber fuel, ignition behavior similar to ethylene at t = 1.6 ms was observed. Tests where methane at Φ = 0.8 was used as main chamber fuel did not ignite across the test iterations. Injecting hot jet at a higher rate may cause possible ignition at this nozzle traverse speed, but detailed study is required in order to conclude this outcome.

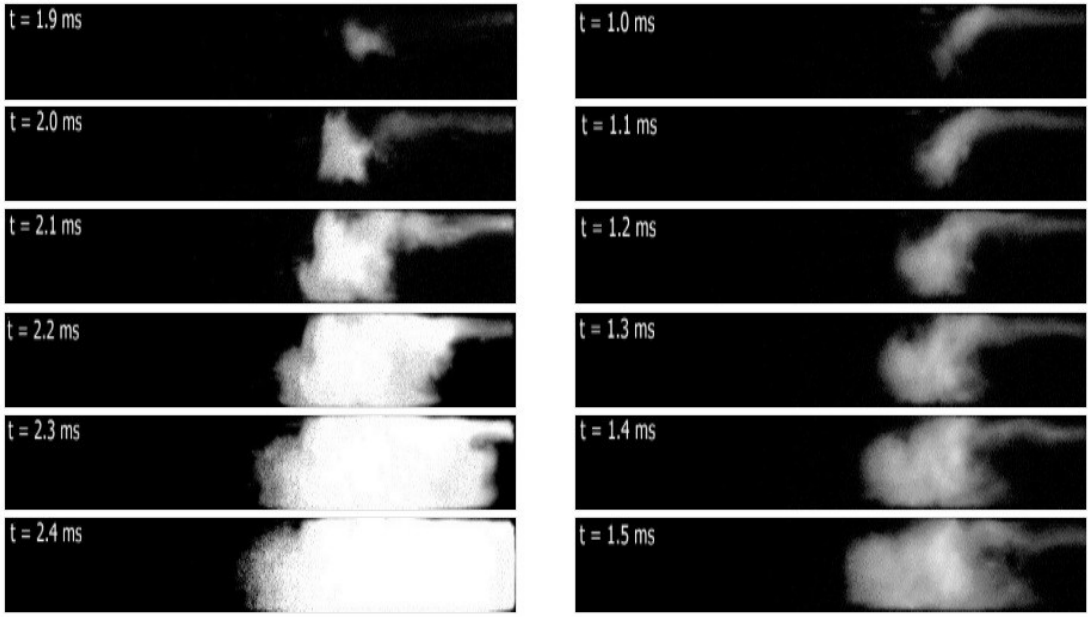

Figure 5. 5 Ignition of Φ = 0.8 ethylene-air mixtures for hot-jet traverse time of 40.6 ms- E-0.8-40.6-1 (left) and 8.1 ms- E-0.8-40.6-3 (right)

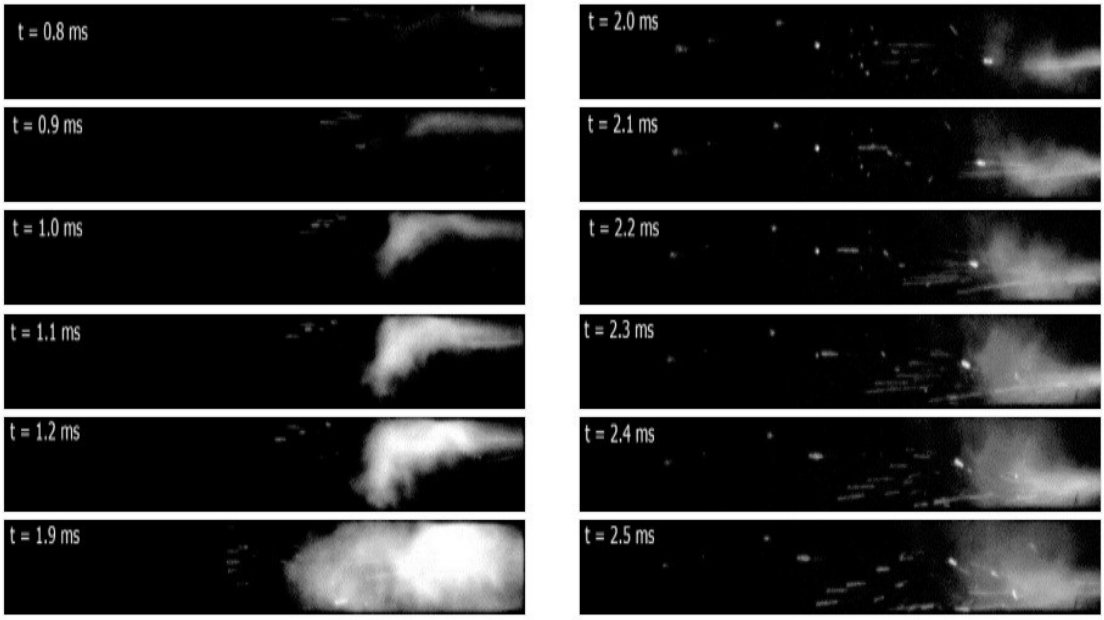

Figure 5. 6 Ignition of Φ = 0.8 ethylene-air mixtures for hot-jet traverse time of 6.1 ms- E-0.8-6.1-1 (left) and 4.1 ms- E-0.8-4.1-1 (right)

Figure 5.7 compares the pressure trace as a result of combusting ethylene-air mixture in the main chamber maintained at Φ = 0.8 in atmospheric pressure and room temperature. These pressure transducers are placed across three different locations in the main chamber as mentioned in Table 3.1. A maximum pressure of 50 psig was recorded at 13.2 ms after the start of jet injection. The maximum pressure was recorded by PT2. For all the studied cases PT1 and PT3 recorded similar pressure traces with subtle difference. The pressure trace from PT2 is seen to follow the PT1 and PT3 until 4 ms.

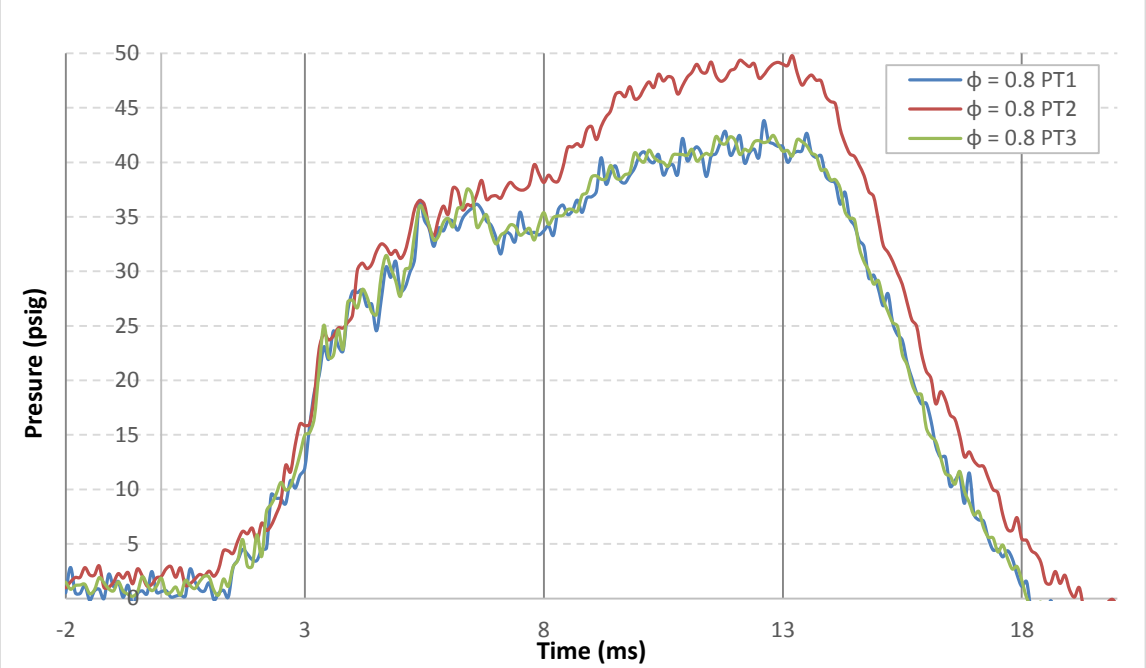

Figure 5. 7 Pressure history recorded at three different transducer location for ethylene at Φ = 0.8 at 8.1 ms (M-0.8-40.6-4)

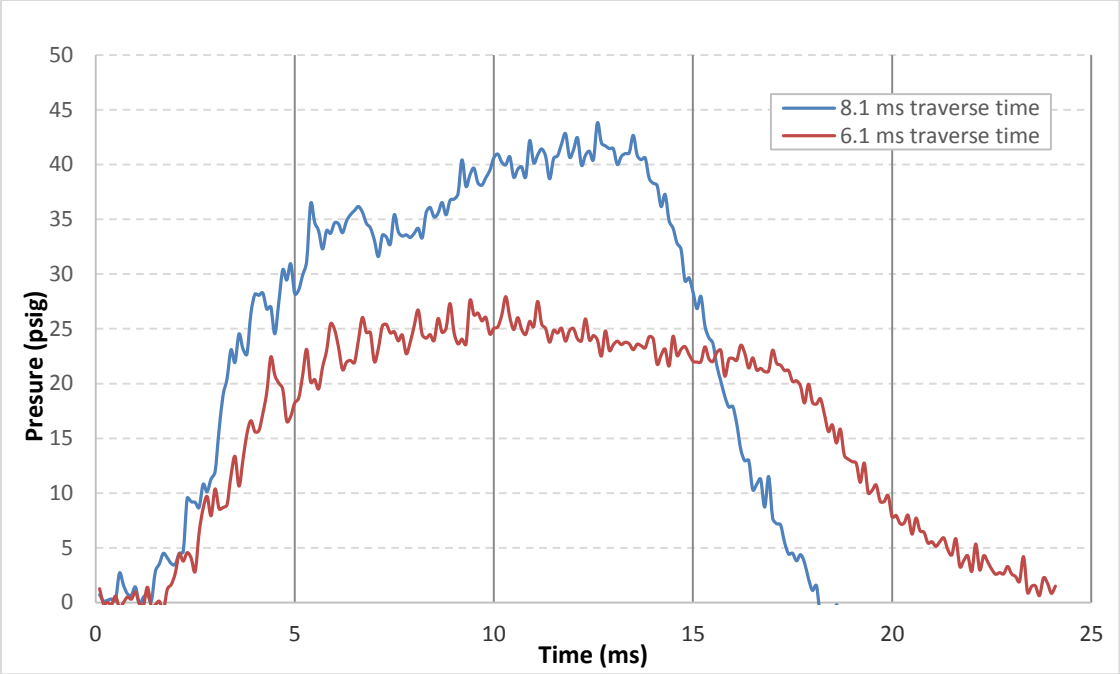

Figure 5. 8 PT1 - Pressure history comparison for Φ = 0.8 ethylene-air mixture at 8.1 ms vs. 6.1 ms nozzle traverse time

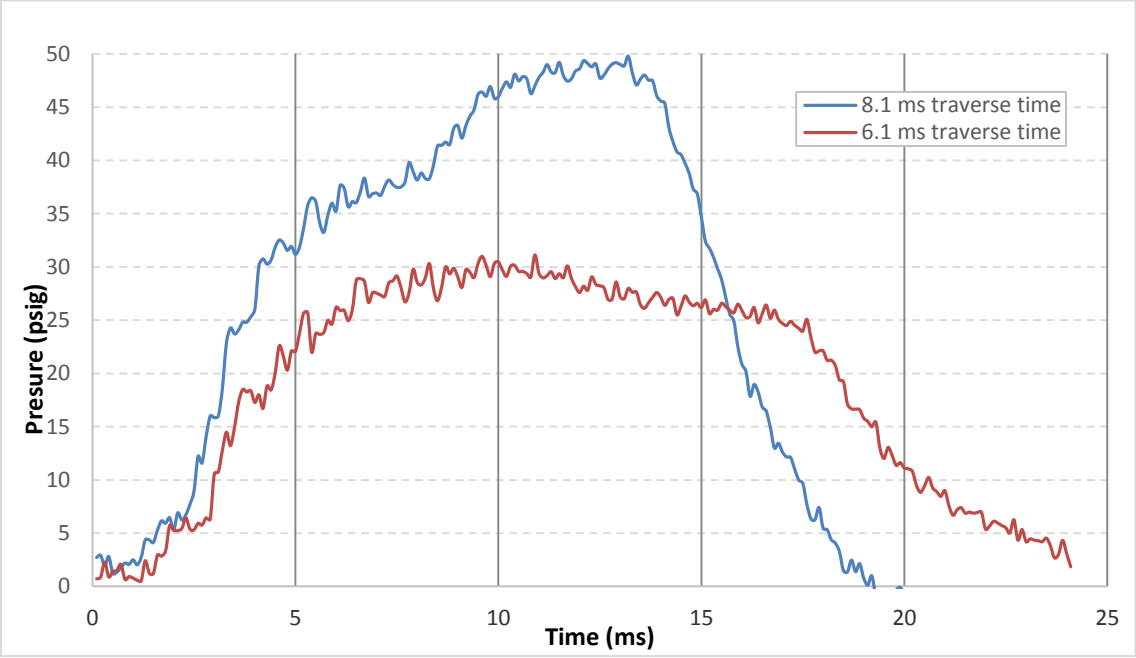

Figure 5. 9 PT2 - Pressure history comparison for Φ = 0.8 ethylene-air mixture at 8.1 ms vs. 6.1 ms nozzle traverse time

A comparison of the pressure traces across two different nozzle traverse speeds for the same equivalence ratio is provided in Figure 5.8 and Figure 5.9. PT3 pressure history is not presented for the brevity. It is observed that the slower speed jet created a strong combustion event. Assuming the amount of mass injected in each fixed time period remains same for both the speeds, the main difference that caused the difference in combustion event was the motion of ignition source. Similar behavior will be seen across other fuels tested supported by further pressure trace evidence in this chapter. It should be noted that past 2.5 ms there is a steep rise in pressure that levels of around 5 ms after which the pressure steadily increases. It has to be noted that past the 0 psig pressure mark, the pressure transducer records negative pressures which is due to the effect of hot gases interacting with the piezoelectric pressure transducers creating a thermal drift effect.

Figure 5.10, 5.11 and 5.12 compares pressure generated by combustion of ethylene at 0.8, 0.6 and 0.4 equivalence ratios for a fixed nozzle traverse time of 6.1 ms. As expected the peak pressure scales itself with the amount of fuel in the main chamber which controls the amount of heat released. It is interesting to note that at $\Phi = 0.4$, where no ignition was detected, the pressure trace looks similar to the case where no fuel was present in the main chamber. Due to absence of any hot combustion products the thermal drift effect is not seen to occur and hence the pressure trace continues to record positive pressure for a longer duration.

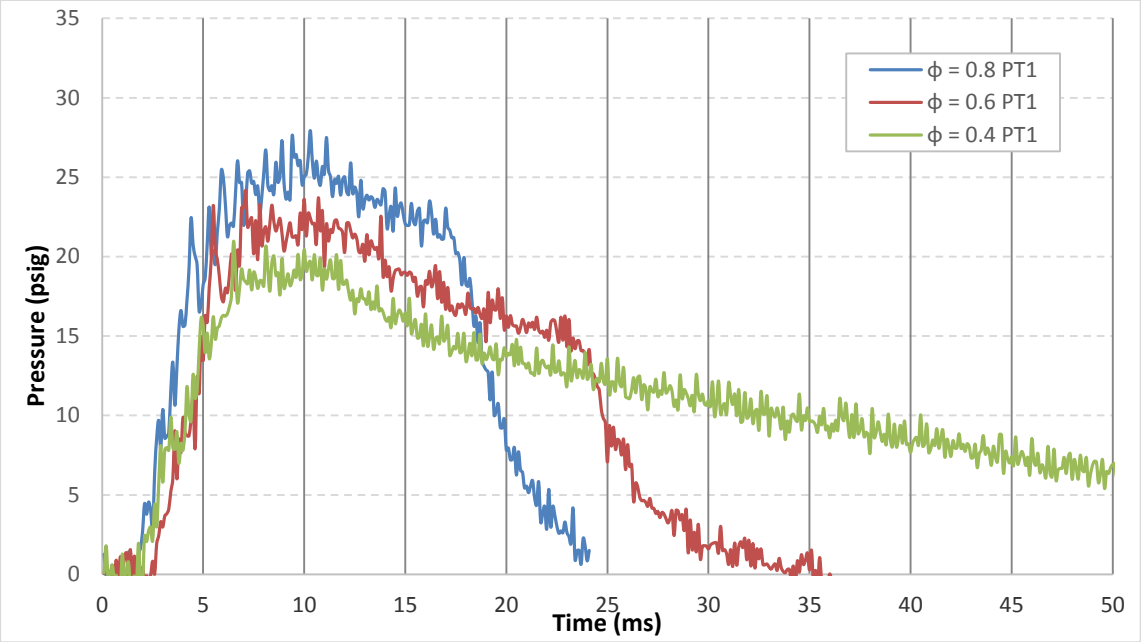

Figure 5. 10 PT1 - Pressure history comparison for ethylene at Φ = 0.8 vs. Φ = 0.6 vs. Φ = 0.4 for 6.1 ms nozzle traverse time

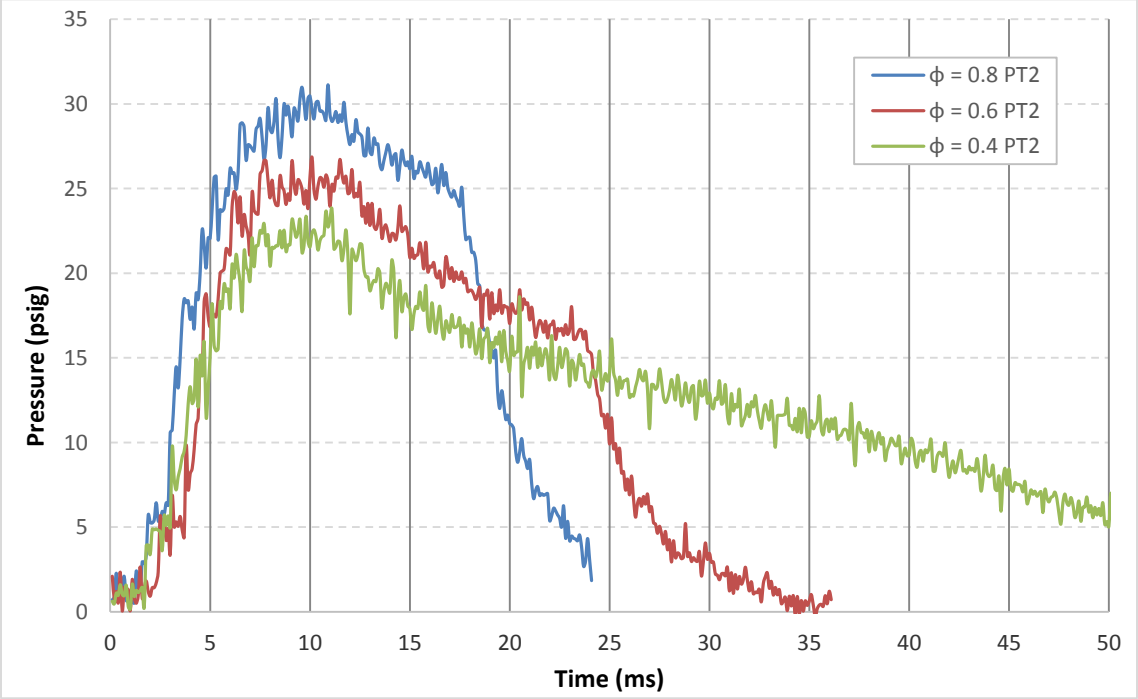

Figure 5. 11 PT2 - Pressure history comparison for ethylene at Φ = 0.8 vs. Φ Φ = 0.6 vs. Φ = 0.4 for 6.1 ms nozzle traverse time

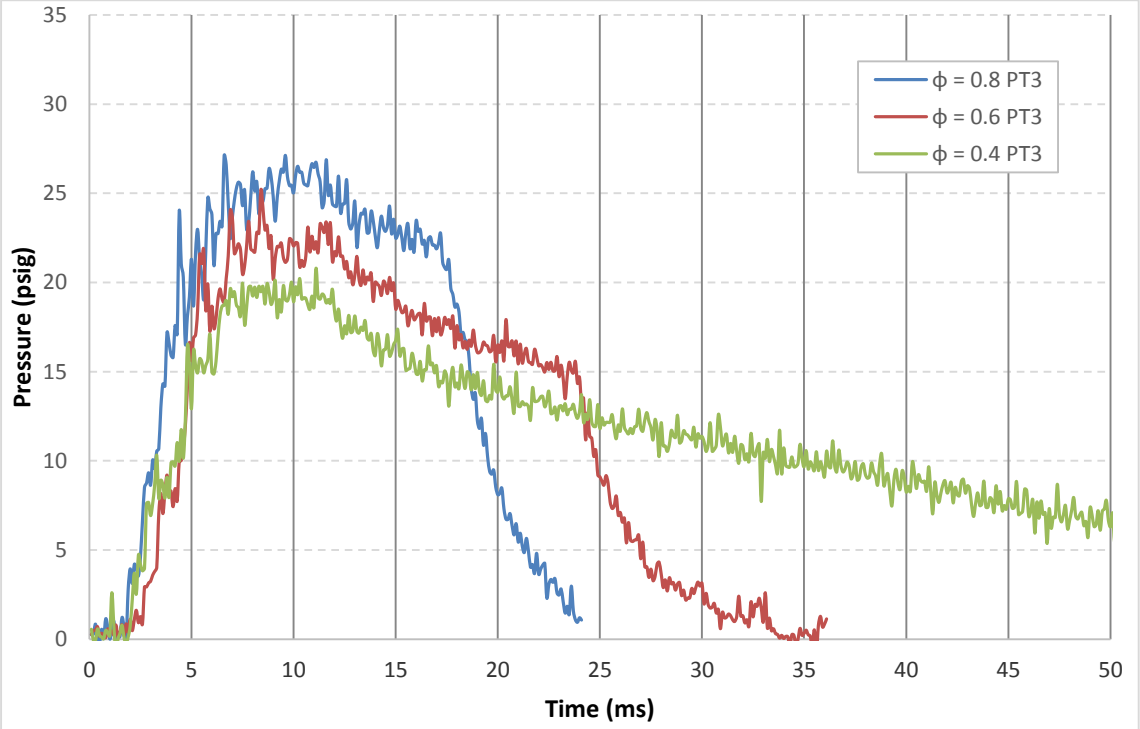

Figure 5. 12 PT3 - Pressure history comparison for ethylene at Φ = 0.8 vs. Φ = 0.6 vs. Φ = 0.4 for 6.1 ms nozzle traverse time

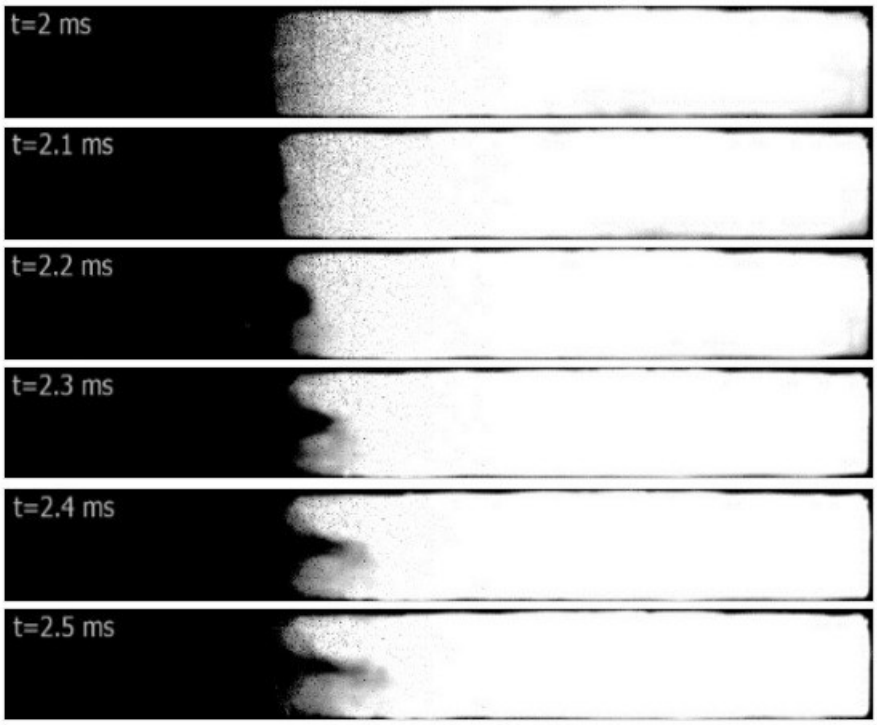

Figure 5. 13 Shock flame interaction observed for ethylene at Φ = 0.8 for 8.1 ms hot-jet traverse time

5.2 Shock Flame Interaction

Within the confined volume of the CVC, the injection of the hot jet and rapid combustion gives rise to pressure waves. The resulting shock wave reflects at the opposite end of the chamber and returns to interact with the incipient flame. The process of shock interaction with a propagating premixed flame is encountered in various physical processes ranging from deflagration to detonation transition to supernovas. The understanding of shock-flame interaction is essential for promoting faster combustion reactions in novel combustion devices such as steady or pulsed detonation engines [4, 69] or wave rotor combustors [70, 71]. In wave-rotor combustor the flame is expected to be within the corrugated flame regime [72], where the major effect is produced by the flame area increase following the shock-flame interaction. Shock-flame interaction leads to a significant increase in total energy release rates; as a consequence, the overall reaction rate increases

due to the baroclinic vorticity production [73, 74]. The high-speed video images from experiments corresponding to combustion of Φ = 0.8 ethylene-air mixture and 8.1 ms jet traverse time is presented in Figure 5.13. Due to the interaction of the propagating flame with the shock wave returning from the main CVC chamber end, the flame front deforms into a mushroom like shape. Numerical analysis of the shock-flame interaction and the reaction rate increase for different traverse speeds has been carried out in another work [20]. Predicted results indicate that shock-flame interaction causes significant increase in reaction rates. The reaction rate increase has been observed to be caused by both flame length/surface increase due to deformation and kinetic amplification [73].

5.3 Ignition Behavior of Methane

Because of methane's tetrahedral molecular structure with high energies in C-H bond, methane exhibits unique combustion characteristics with high ignition delay times, high ignition temperature and low flame speed. Being the primary constituent of natural gas the chemical kinetics of methane have been widely researched and well understood. Although implementing methane as a main stream fuel presents various challenges due to the ignition property of the fuel itself several research efforts are made to understand the suitability of methane in practical combustors and IC engine applications due to benefits in terms of availability, fuel costs and significant reductions in emissions of greenhouse gases and NO_x. Compressed Natural Gas (CNG) has already been adapted and used as fuel for commercial vehicles and for operating gas turbines in energy sectors.

Methane is also produced in intermediate reaction pathways during oxidation of higher hydrocarbons. The chain initiation reaction of methane starts in various configurations as shown below,

$$CH_4 + M \rightarrow CH_3 + H + M \qquad 5.10$$

$$CH_4 + H \rightarrow CH_3 + H_2 \qquad 5.11$$

$$CH_4 + OH \rightarrow CH_3 + H_2O \qquad 5.12$$

$$CH_4 + O \rightarrow CH_3 + OH \qquad 5.13$$

$$CH_4 + HO_2 \rightarrow CH_3 + H_2O_2 \qquad 5.14$$

Some of the important recombination reactions of methane at temperatures close to 1100 K, been reported to exist during hot jet ignition process [18] are listed below. These recombination reactions make methane oxidation different from ethylene oxidation.

$$CH_3 + O_2 \rightarrow CH_3O + O \qquad 5.15$$

$$CH_3 + CH_3 \rightarrow C_2H_5 + H \qquad 5.16$$

$$CH_3 + CH_3 \rightarrow C_2H_4 + H_2 \qquad 5.17$$

$$CH_3 + CH_3 \rightarrow C_2H_6 \qquad 5.18$$

Figure 5.14 compares two identical cases where methane-air mixtures were maintained at $\Phi = 0.8$ in the main chamber and was ignited by hot-jet traversing the main chamber in a time of 8.1 ms. Ignition occurred at a distance of 109.1 mm and 101.6 mm in the main chamber for these test cases. The appearance of the jet, location of ignition and subsequent combustion behavior is different compared to the ethylene images discussed in the previous section. Apart from the increased ignition delay time the two identical test cases exhibited very similar ignition and combustion behavior between each other, suggesting less cycle to cycle variation in a practical combustor operation. Compared to ethylene the variation of ignition delay times across the identical tests performed were quite large with methane as main chamber fuel. For $\Phi = 0.8$ a difference of 1.7 ms in ignition delay time was observed across tests with initial condition of 40.6 ms nozzle traverse time while ethylene only showed a maximum of 0.9 ms ignition delay time variation across 8.1 ms nozzle traverse time tests.

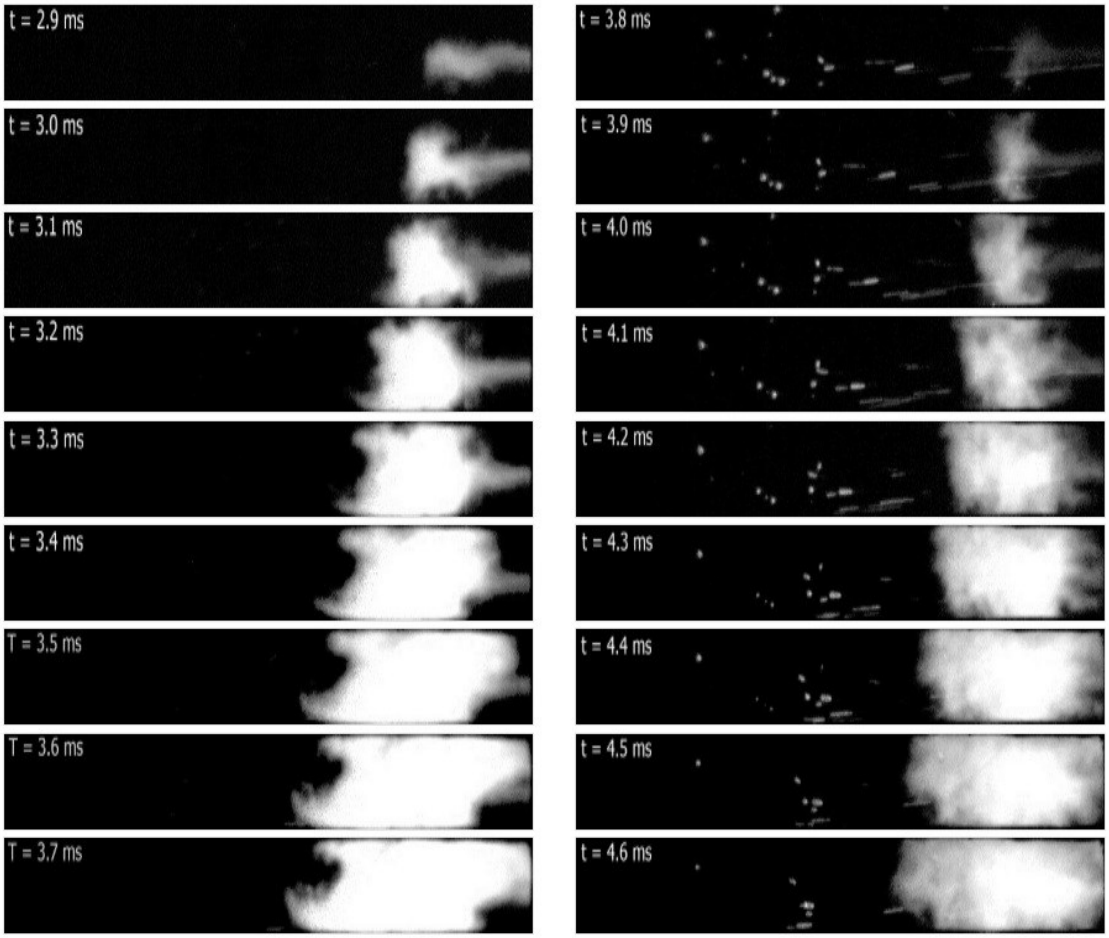

Figure 5. 14 Comparison of ignition and subsequent flame propagation for methane at Φ = 0.8- M-0.8-8.1-1 (left) and methane at Φ = 0.8 - M-0.8-8.1-3 (right) for hot-jet traverse time of 8.1 ms

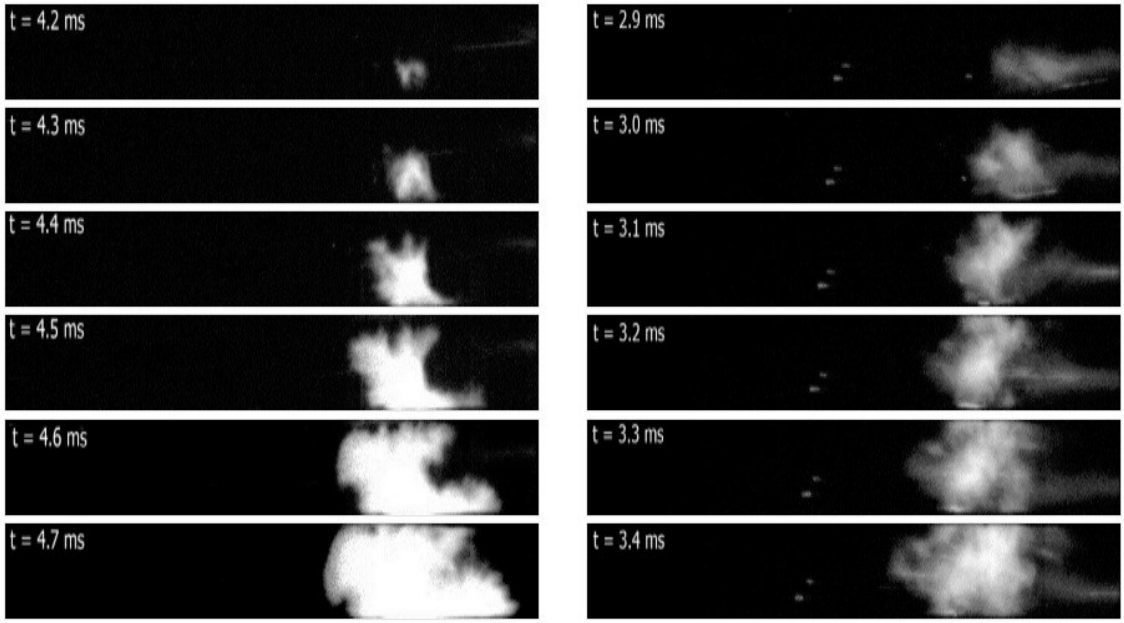

Figure 5. 15 Traversing jet ignition of Φ = 0.8 methane-air mixtures at 40.6 ms traverse time - M-0.8-40.6-1 (left) and 6.1 ms nozzle traverse time - M-0.8-6.1-2 (right)

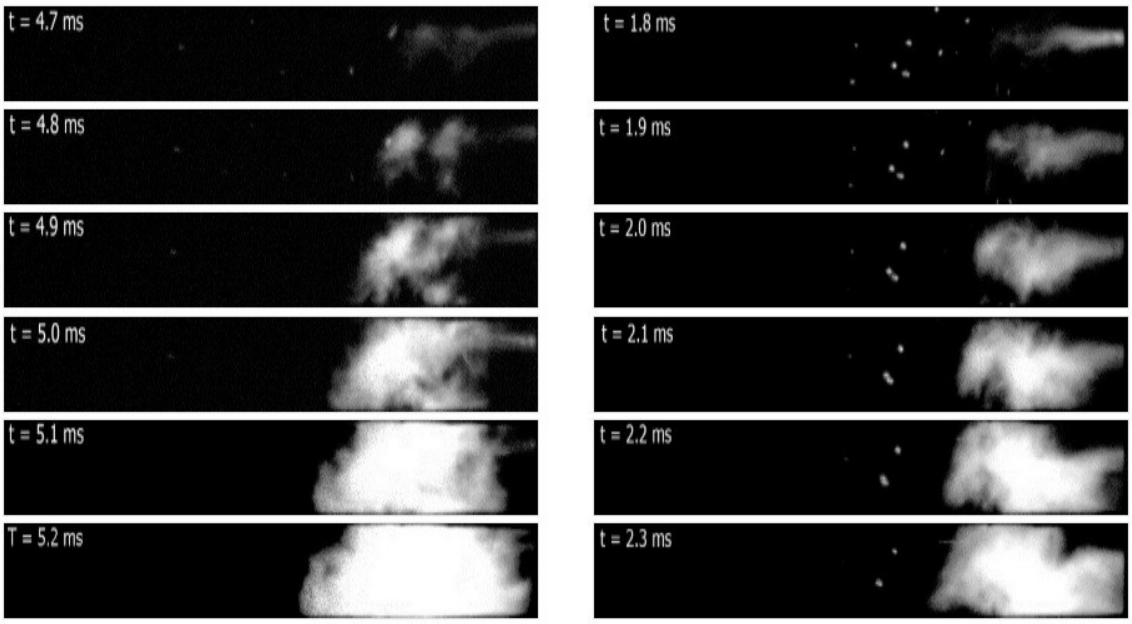

Figure 5. 16 Traversing jet ignition Φ = 0.6 methane-air mixtures at 40.6 ms nozzle traverse time- M-0.6-40.6-1 (left) and 6.1 ms nozzle traverse time - M-0.6-6.1-1 (right)

Figure 5.15 is another interesting comparison of methane ignition behavior. For both the test cases main chamber was filled with methane-air mixture at $\Phi = 0.8$. The sequence of images on the left corresponds to a slower nozzle traverse time of 40.6 ms while the other rotates along with a pre-chamber at a speed of 1000 rpm and hence a nozzle traverse time of 6.1 ms. As could be inferred from the figure for both the cases, ignition starts close to the lower wall of the CVC but the reason for having such an ignition location occurs due to two different physical process related with jet injection. For the case of 40.6 ms traverse time the ignition location is dictated due to the path of the wall impinging jet while for the 6.1ms it is due to the fact that the nozzle has traversed past the mid-point of the main chamber entrance at the time of ignition. Also for the higher nozzle traverse speeds the observed flame propagation speed is not as rapid as seen in the lower speed case which will also be reflected in the pressure traces to be discussed later in this section.

Figure 5.16 compares the effect of two different nozzle traverse speeds as discussed in Figure 5.15 but for an equivalence ratio of 0.6 in the main chamber. For the image in the left although the ignition starts at multiple sites some distance away from the lower wall the subsequent ignition pattern past 4.8 ms highlights the vortices development due to wall impingement of the jet. While comparing Figure 5.16 and Figure 5.15 there is an observable reduction in ignition delay time for the case with $\Phi = 0.6$ compared to $\Phi = 0.8$. Similar ignition delay time reduction as the main chamber mixture gets leaner will be observed will be discussed in this chapter. Comparing Figure 5.15 and Figure 5.16 it is clear that hot-jet ignites in a very consistent fashion across different equivalence ratios while the jet path and ignition remains similar across tests with identical nozzle traverse time mixtures.

As an another example of complex ignition behavior, Figure 5.17 indicates presence of an ignition zone at t = 3.6 ms. Due to turbulent nature of the penetrating jet, the ignition site is transported from an initial location of 114 mm (from the start of optical window to) to 172.4 mm where the ignition zone finally stabilizes and proceeds to flame propagation phase. Note that the images shown are two dimensional representations of

three dimensional ignition and flame development process. The ignition site was moved to a total distance of 58.4 mm from the initial visible location until it could reach an undisturbed region where flame propagation could be initiated. It would have been interesting to observe the vortex evolutions that occurred during this process using advanced flow visualization techniques. Figure 5.18 shows the next sequence of images for this test that precedes the ignition event. Due to long induction time the ignition site was observed a bit further from usual location. As the flame propagation starts from the ignition site the regions along the hot jet penetration path rapidly ignites and consumes the main chamber fuel at t = 5.4 ms. This resembles an auto ignition kind of behavior that is characteristic of a compression ignition engines and other low temperature combustion modes such as Homogeneous Charge Compression Ignition (HCCI) in IC engines.

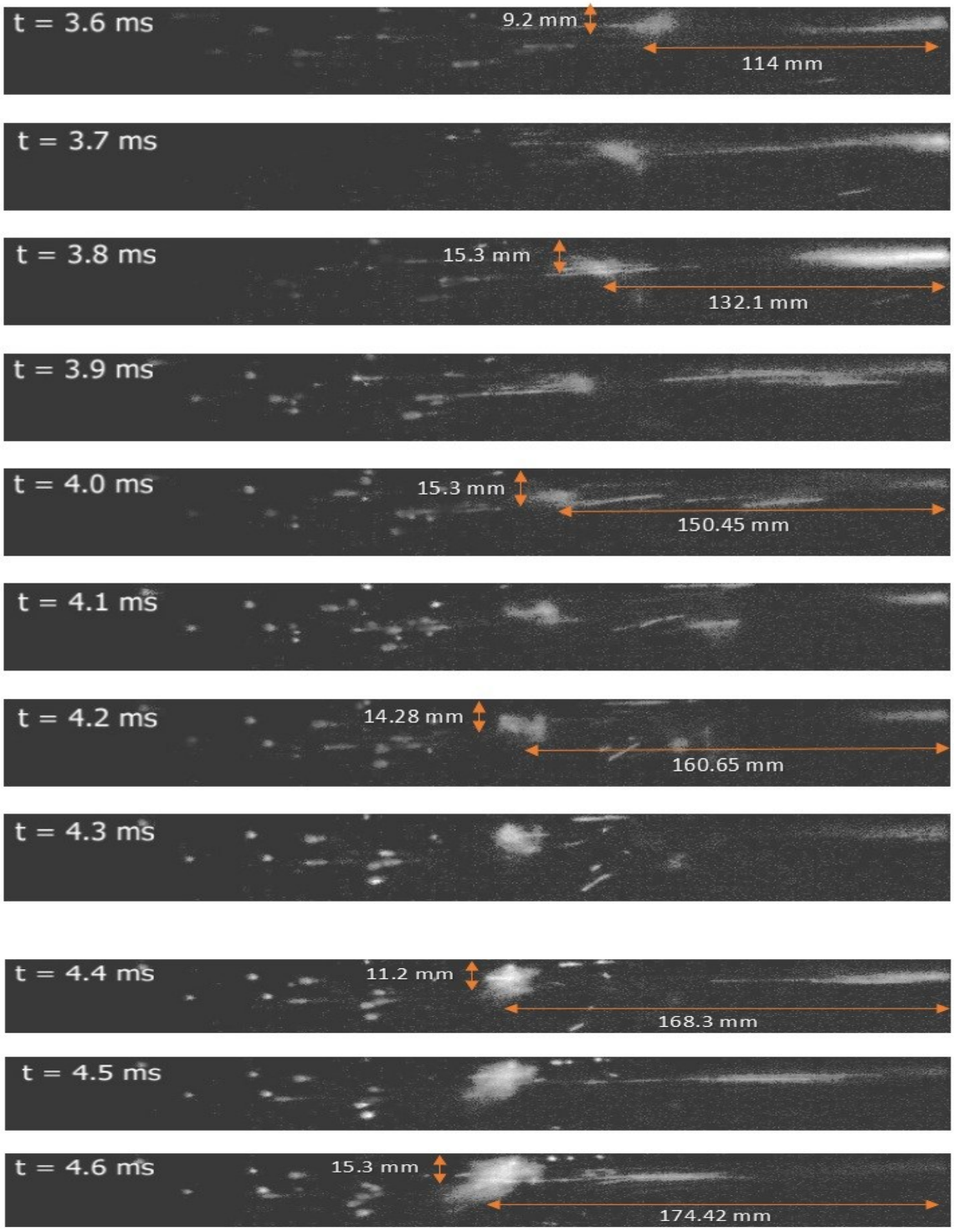

Figure 5. 17 Traversing jet ignition of Φ = 0.8 methane-air mixture at 40.6 ms traverse time - M-0.8-40.6-2. Images are enhanced for better clarity.

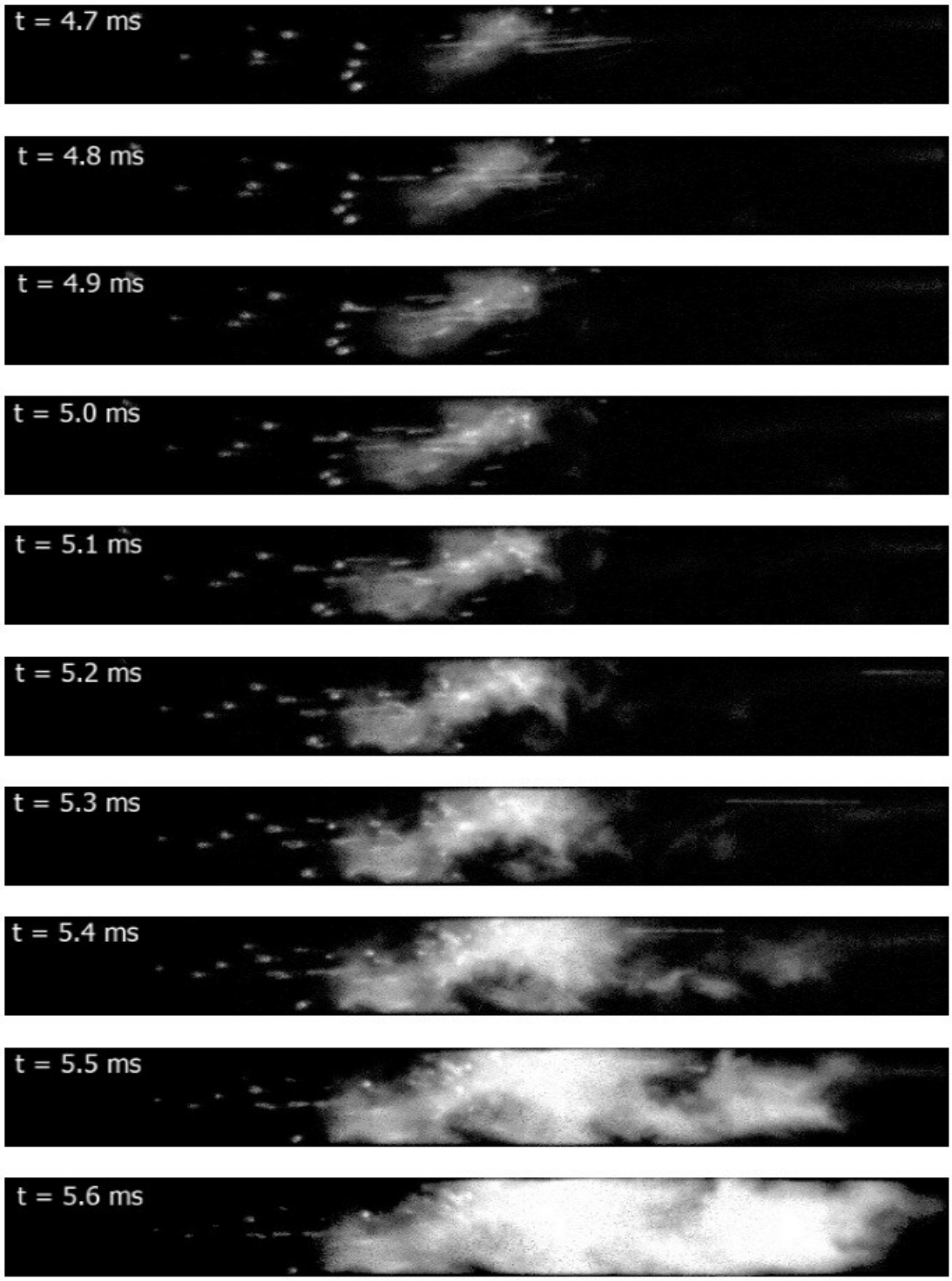

Figure 5. 18 Traversing jet ignition of Φ = 0.8 methane-air mixture at 40.6 ms nozzle traverse time (M-0.8-40.6-2)

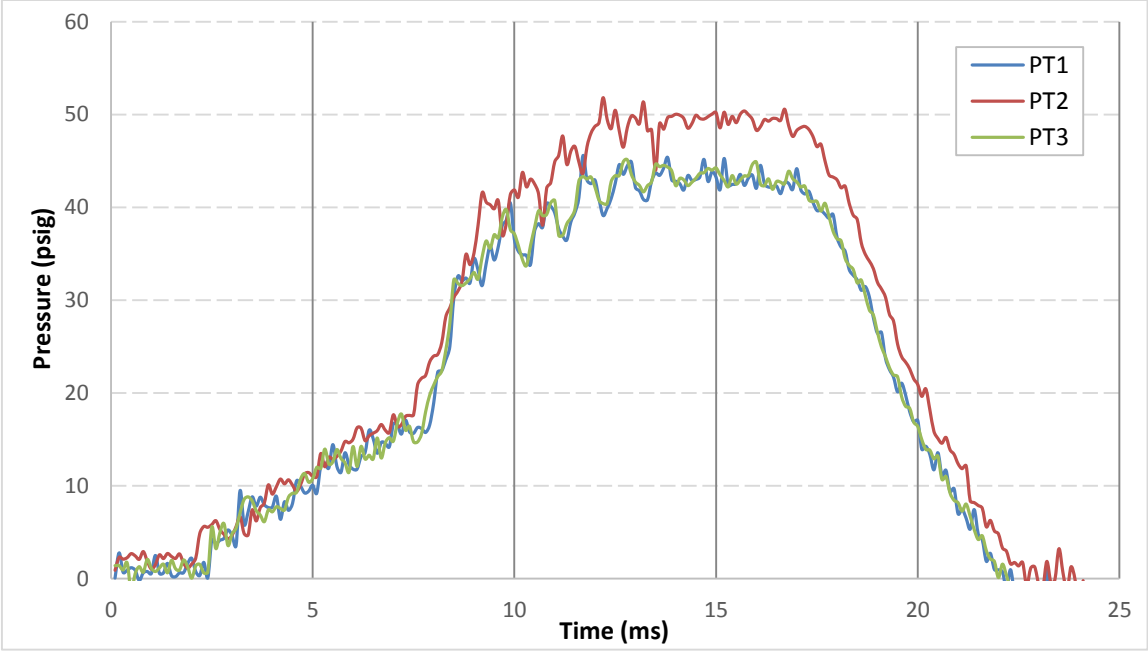

Figure 5. 19 Pressure history recorded at three different transducer location for methane at Φ = 0.8 for 40. 6 ms (M-0.8-40.6-3)

Figure 5.19 compares the pressure trace generated by the transducers PT1, PT2 and PT3 for methane combustion at Φ = 0.8 ignited with the slowest traversing jet. Similar to pressure traces seen for ethylene combustion the change owing to ignition is recorded at different peak levels across the transducers. While PT2 sees the highest pressure, PT1 and PT3 records approximately 5 psig lesser than PT2. All three traces follow a similar trend up until 8 ms after which PT3 starts recording higher pressure. When compared to ethylene where the pressure generated rapidly rises and begins to level of around 5 ms methane levels of at 10ms. Also, there is an indication of very slow increase in pressure up until 7.5 ms after which the rapid rise in pressure occurs. The pressure traces clearly dictates the combustion behavior of different fuels.

Figure 5.20 and 5.21 compares pressure traces generated by combustion of methane at three equivalence ratios with a fixed nozzle traverse time of 8.1 ms. The pressure curves follow similar behavior across each other with the most obvious difference of reduction in

pressure with respect to decrease in fuel content. All three traces reflects the pressure rise pattern observed in Figure 5.19. Pressure rise due to 0.8 equivalence ratio methane combustion across different nozzle traverse speeds is compared in Figure 5.22 at PT2 pressure transducer location. A very strong combustion was recorded with 40. 6 ms while others had a very similar pressure traces. It is clearly evident that the maximum pressure attained by fuel air mixtures reduces as the nozzle traverse speed increases. This indicates more complete combustion of the main chamber fuel as the nozzle approaches slower traverse speeds.

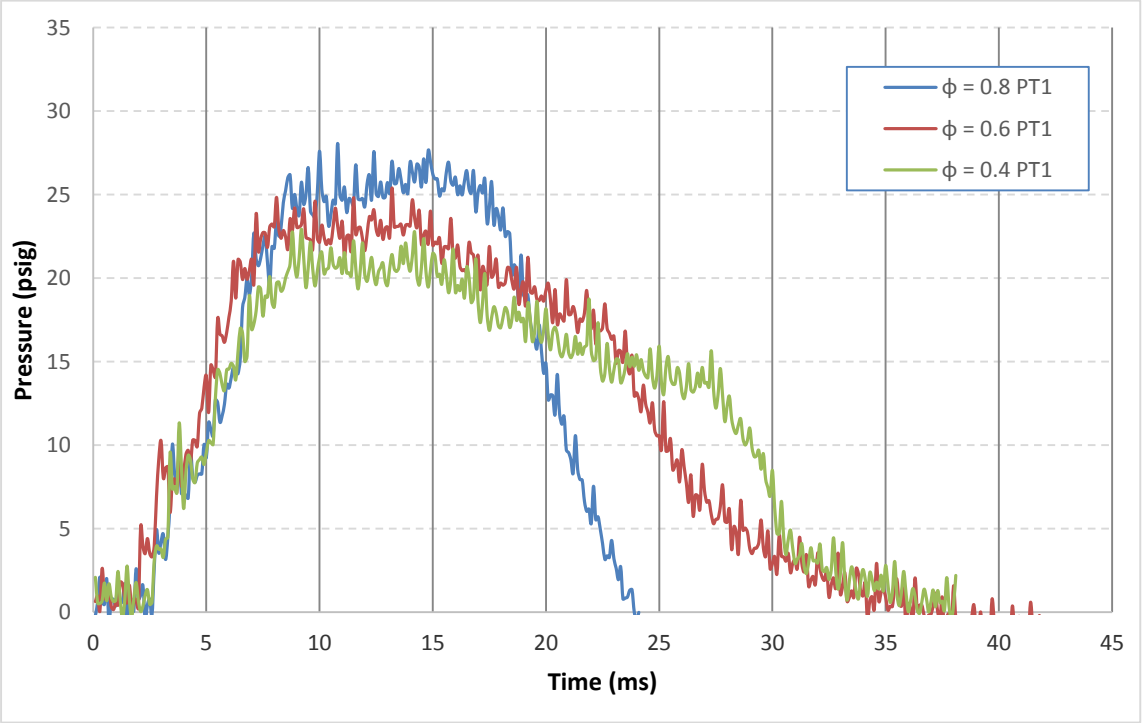

Figure 5. 20 Pressure history comparison at PT1 for methane combustion across equivalence ratios Φ = 0.8 (M-0.8-6.1-3), Φ = 0.6 (M-0.6-6.1-2), Φ = 0.4 (M-0.4-6.1-2) at 6.1 ms nozzle traverse time.

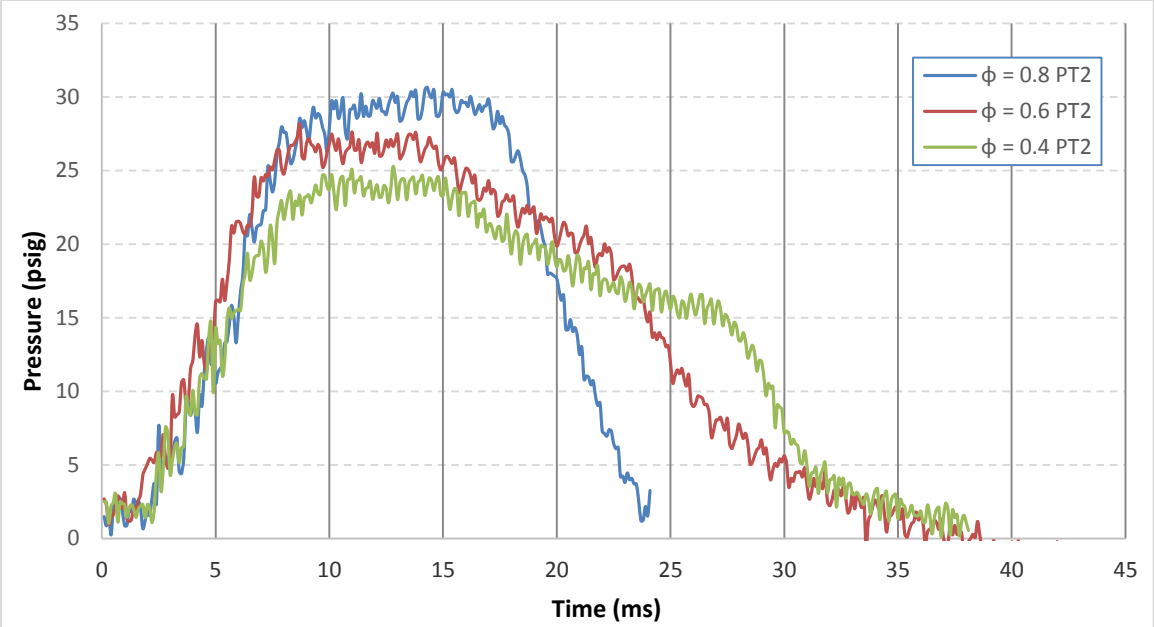

Figure 5. 21 Pressure history comparison at PT2 for methane combustion across equivalence ratios Φ = 0.8 (M-0.8-6.1-3), Φ = 0.6 (M-0.6-6.1-2), Φ = 0.4 (M-0.4-6.1-2) at 6.1 ms nozzle traverse time.

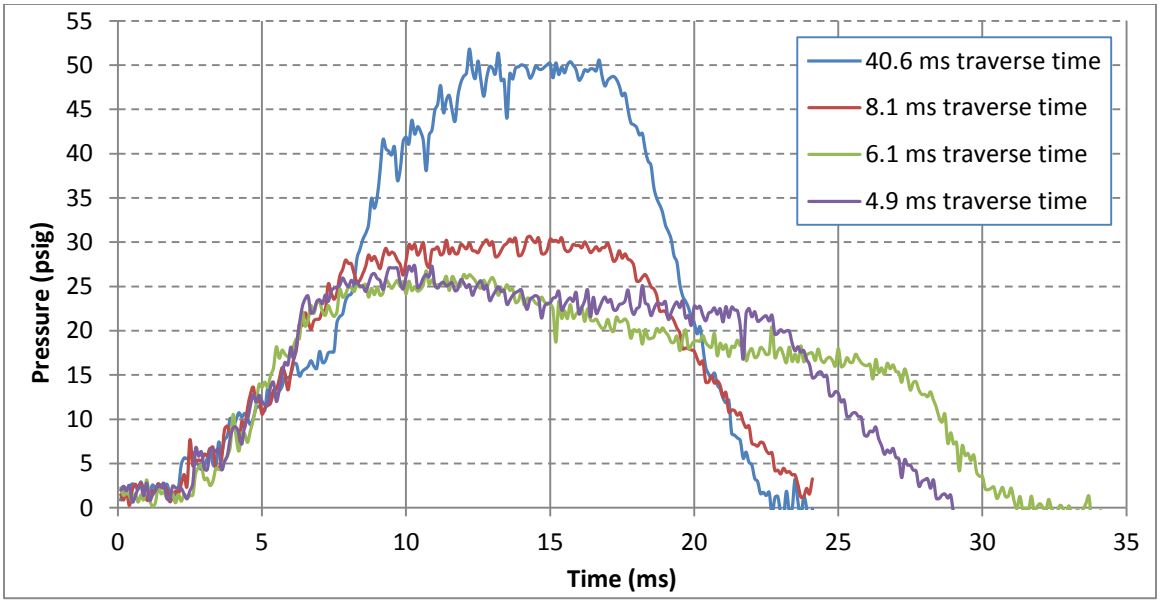

Figure 5. 22 Pressure history comparison at PT2 for methane combustion across different traverse time (40.6 ms – M-0.8-6.1-3, 8.1 ms - M-0.8-8.1-3, 6.1 ms - M-0.8-6.1-1, 4.9 ms - M-0.8-4.9-2) at Φ = 0.8 equivalence ratio.

5.4 Ignition Behavior of H2-Methane Blend

Pure methane is characterized by long ignition delay times and cannot be directly used as a fuel for supersonic propulsion aerospace applications. Some kind of ignition-aid is required to accelerate ignition delay time of methane-air mixtures and hydrogen has been proposed as one viable ignition enhancer. Experimental [75] and computational studies [76] have revealed that addition of hydrogen to natural gas improves the tolerance of exhaust gas recirculation(EGR) and greatly reduces NOx and hydrocarbon emissions in IC engines. Shreshta et al., [75] investigated that addition of small amounts of hydrogen to methane in a spark ignition engine increased performance and combustion efficiency significantly while emissions were reduced. Indeed the addition of hydrogen allows to extend the lean flammability limit of the natural gas mixture. The purpose of this section of the study is to investigate influences of hydrogen addition to methane on ignition delay times and flame propagation compared to methane. Although similar comparison has been carried out before by different researchers, no studies were attempted on this blend using hot jet as ignition source. Furthermore hydrogen blending and jet ignition have been viewed and tested separately as lean burn combustion enablers in IC engines and hence combining them should provide superior benefits.

Ju et al., [77] conducted ignition studies on hydrogen blended methane mixtures on a supersonic mixing layer. They identified three stages on reaction progress that affected the ignition delay time of these mixtures. The three stages were, a chain-branching inhibition stage, a transition stage and a reaction competition stage. During the first stage it was identified that endothermic reaction $CH_4 \rightarrow CH_3+H$ resulted in a slow development of temperature and reaction $H+CH_4 \rightarrow CH_3+H_2$, scavenged the radical H. As a result, ignition time increased quickly. During the second stage, production of new H radical through the reaction $CH_4 \rightarrow CH_3+H$ levelled of this rapid increase of ignition time. During the third stage, the increase of concentration of H radicals induced a fast procession of $H+CH_4 \rightarrow CH_3+H_2$ which suppressed the two key reactions, $H+O_2 \rightarrow OH+O$ and $H+O_2+M \rightarrow HO_2+M$ and then lead to a second rapid increase of ignition time.

Figure 5.23 compares the ignition behavior of CH_4 – H_2 mixtures for two equivalence ratios of 0.8 and 0.6 at 6.1 ms nozzle traverse time. The ignition and jet behavior of the sequence of images on the left is very similar to methane at Φ = 0.8 and ethylene-air mixture at Φ = 0.6 for 6.1 ms nozzle traverse that were discussed before. The ignition starts close to the wall dictated by the location of the nozzle. Whereas the blend at Φ = 0.6 (Figure 5.23 – right) ignites much earlier with an ignition delay time of 1.6 ms. The combustion starts at multiple sites as observed in the images. The trend where reduction in ignition delay time is consistent with increase in lean limit is also observed in the blended fuel mixture. However this relation does not hold true for ethylene-air mixtures. This indicates a possibility that the jet generated by ethylene combustion products readily reacts with high concentration of ethylene-air mixtures but when injected into methane mixtures the reactivity is reduced as the methane concentration is increased.

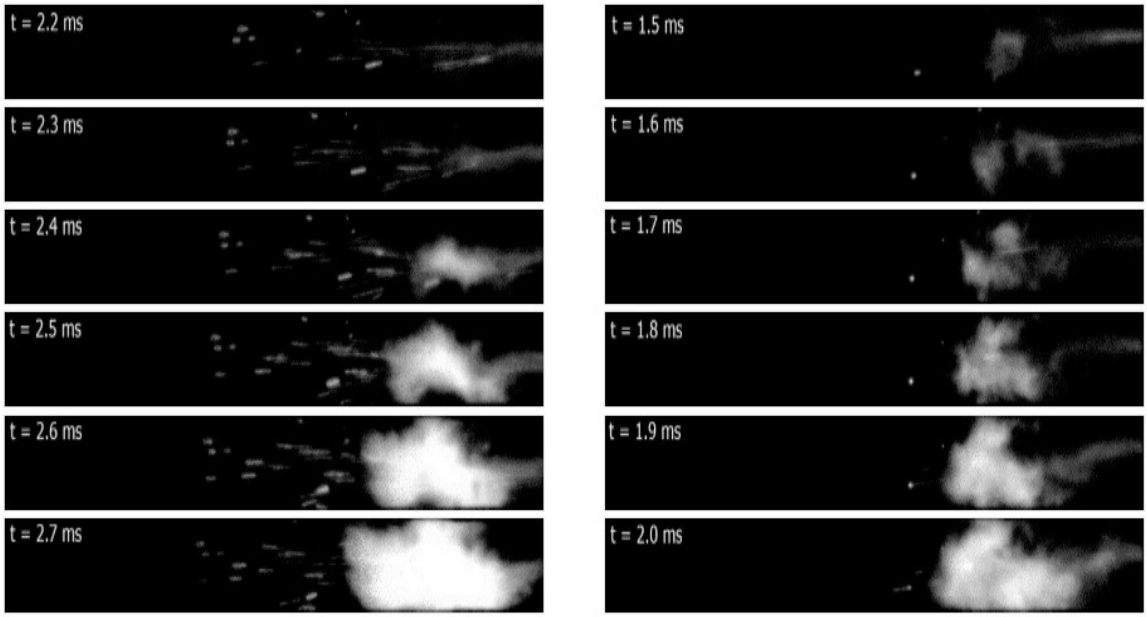

Figure 5. 23 Traversing jet ignition of hydrogen blended methane at Φ = 0.8 - B-0.8-6.1-1 (left) and Φ = 0.6 (right) for hot-jet traverse time of 6.1 ms - B-0.6-4.9-3

Figure 5.24 compares CH_4-H_2 mixtures at Φ = 0.8 and Φ = 0.6 at 8.1 ms nozzle traverse time. Both the images indicate ignition starting at multiple points and combustion proceeding rapidly from that point onward. 0.8 equivalence ratio case had a longer

induction time and the ignition starts closer to the wall due to wall impinging jet behavior that occurred earlier in the process. Though images in the right shows ignition sites in the middle, at t = 2.1 ms ignition appears to be controlled by the developed primary vortices. The ignition looks very similar to ignition of ethylene at Φ = 0.8 in Figure 5.3 where ignition appeared to proceed from vortex cores generated. In general for all the tests performed CH_4 - H_2 mixtures exhibited lower ignition delay times compared to methane and slightly higher ignition delay times compared to ethylene.

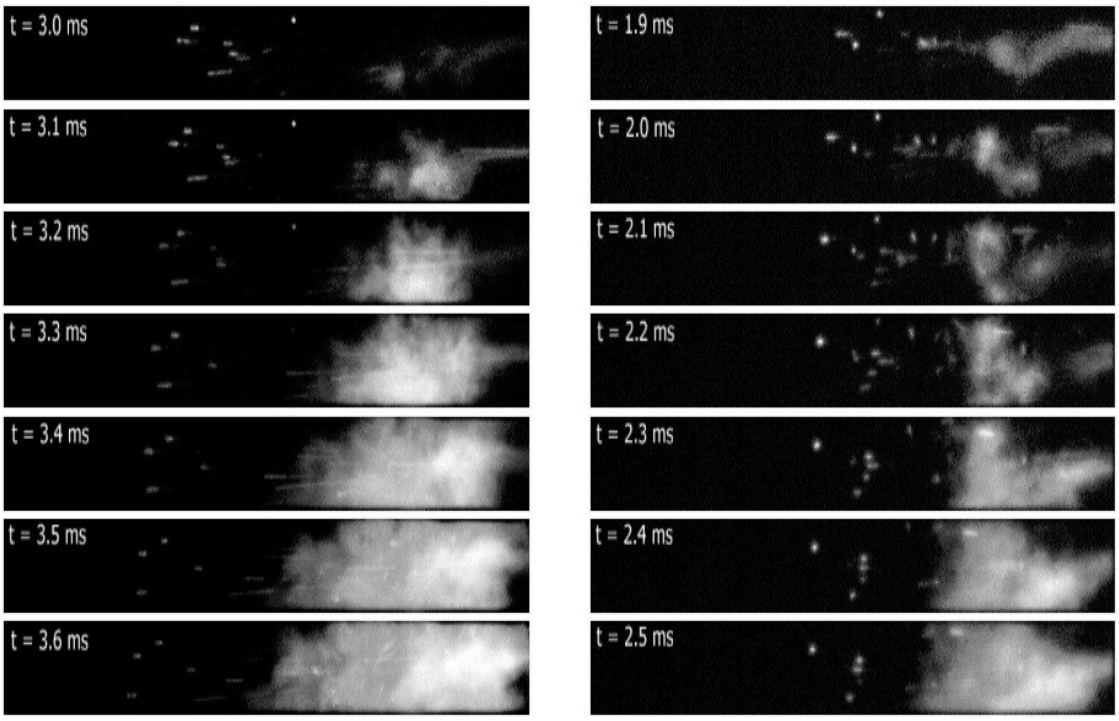

Figure 5. 24 Traversing jet ignition of hydrogen blended methane at 8.1 ms nozzle traverse time for Φ = 0.8 (B-0.8-8.1-2) – Test 2 and Φ = 0.6 (B-0.6-8.1-2) - Test 2

Figure 5.25 and Figure 5.26 compares lean ignition process as initiated by the traversing hot-jet in main chamber mixtures maintained at Φ = 0.4. Figure 5.26 is the continuation of sequence of images presented for ethylene in Figure 5.4. The ignition pattern at an ultra-lean equivalence ratio of 0.4 is completely different from the other concentration of mixtures investigated in this study. Spontaneous ignition happens near the vicinity of the jet injection location but no flame propagation will be seen further from the

point where jet manages to penetrate through the length of the CVC. This is similar to lean combustion behavior initiated using hot jets in the IC engine applications where flame propagation is not used rather the jet acts as a multi-point ignition source to combust the mixture at several zones thereby rapidly consuming the charge [78]. This implies two ways to combust lean mixtures on a CVC. One is to use a higher jet penetration while another configuration would be to inject jet from both ends as studied by Maxson [32] where a double efflux jet was used to penetrate and ignite the main chamber mixtures from both sides. With the ability to quickly combust the charge that is present within the jet penetration region; mixture stratification can be employed thereby maintaining leaner fuel air ratio near the ignition source and maintaining almost zero fuel far from it.

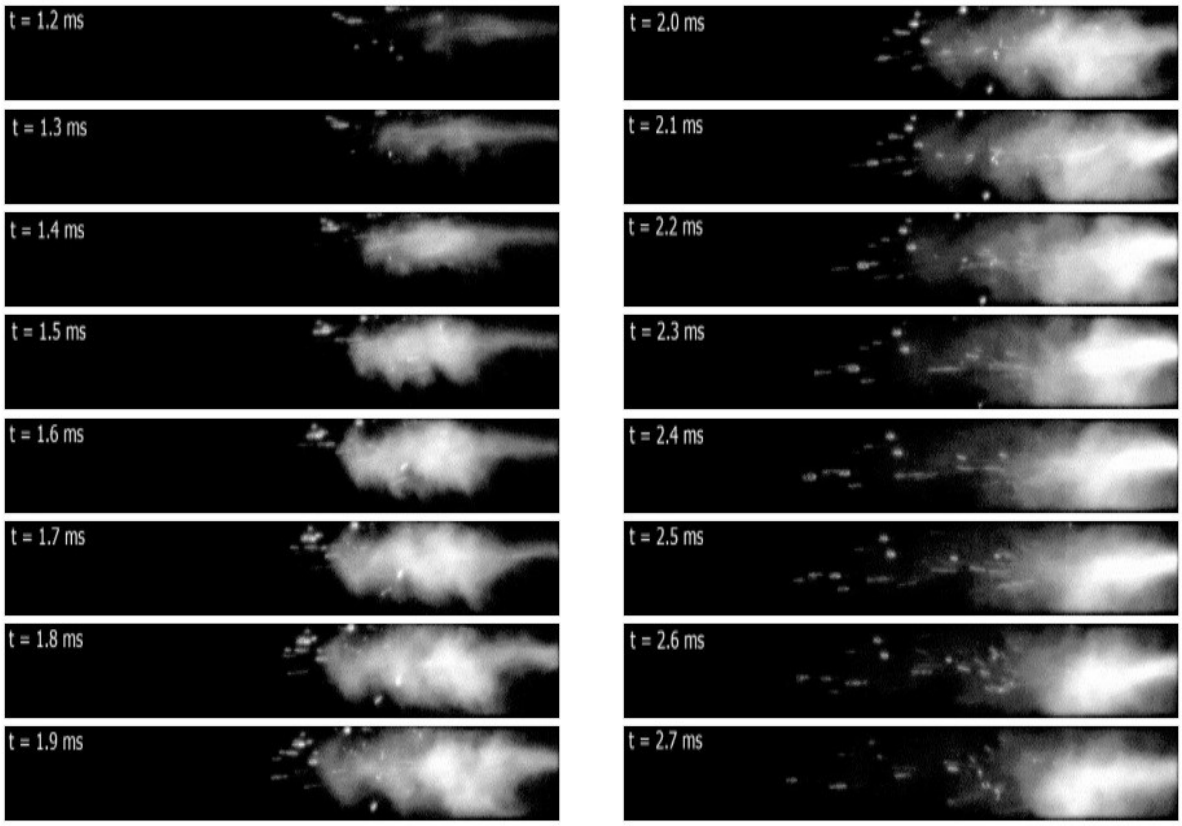

Figure 5. 25 Traversing jet ignition for Φ = 0.4 hydrogen blended methane-air mixture (B-0.4-6.1-2) for 6.1 ms nozzle traverse time - Both columns

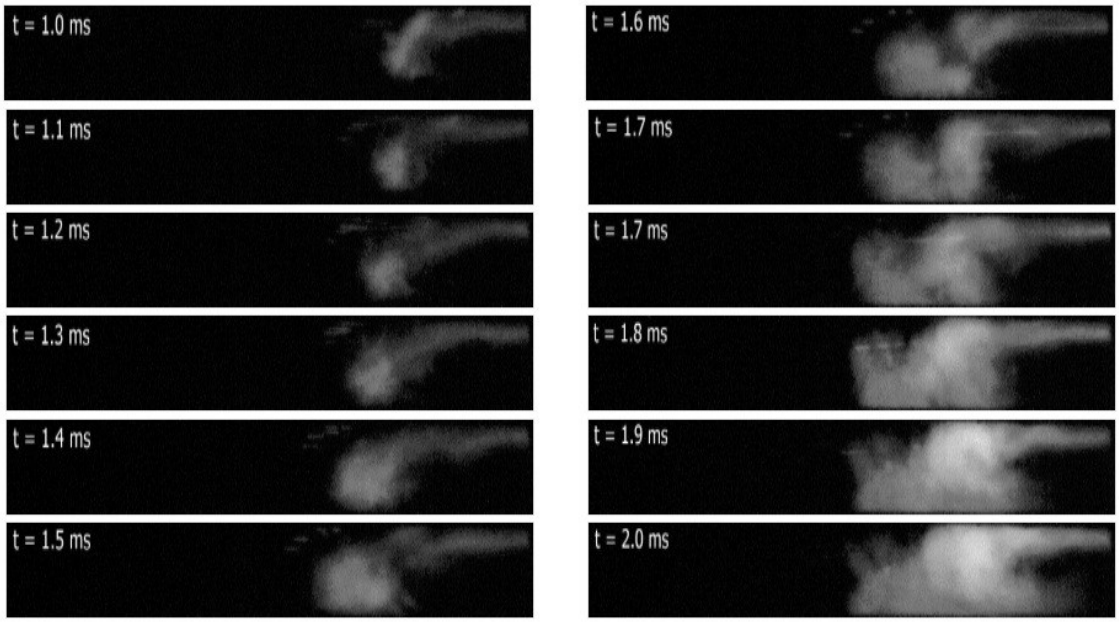

Figure 5. 26 Traversing jet ignition of Φ = 0.4 ethylene-air mixture (E-0.4-40.6-1) for 40.16 ms nozzle traverse time - Both columns

Figure 5.27 and 5.28 compares pressure traces for hydrogen blended methane-air mixtures across three equivalence ratios at 8.1 ms nozzle traverse time. The trace resembles more of an ethylene type of combustion event than that of a methane and the rapid increase in pressure levels off around 7ms. During initial stages where a very gradual increase in pressure was observed in methane-air traces although visible, is not pronounced for a sufficiently long time for the blended mixtures. Figure 5.29 and 5.30 compares ignition behavior of CH_4-H_2 mixtures for Φ = 0.8 at three different nozzle speeds. Across the compared speed the pressure variation is not very pronounced, nonetheless decrease in maximum pressure rise is seen with increase in nozzle traverse speed as observed for other cases.

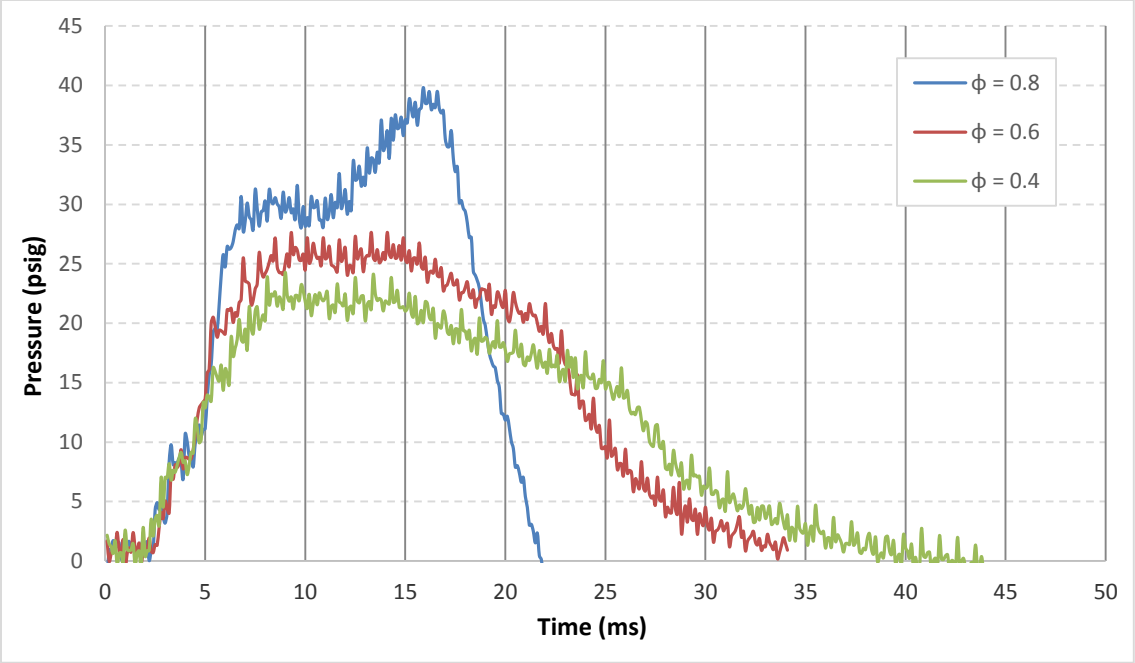

Figure 5. 27 Pressure history comparison at PT1 for hydrogen blended methane mixtures across different equivalence ratios for 8.1 ms nozzle traverse time (Φ = 0.8 (B-0.8-8.1-2), Φ = 0.6 (B-0.6-8.1-3) and Φ = 0.4 (B-0.4-8.1-3))

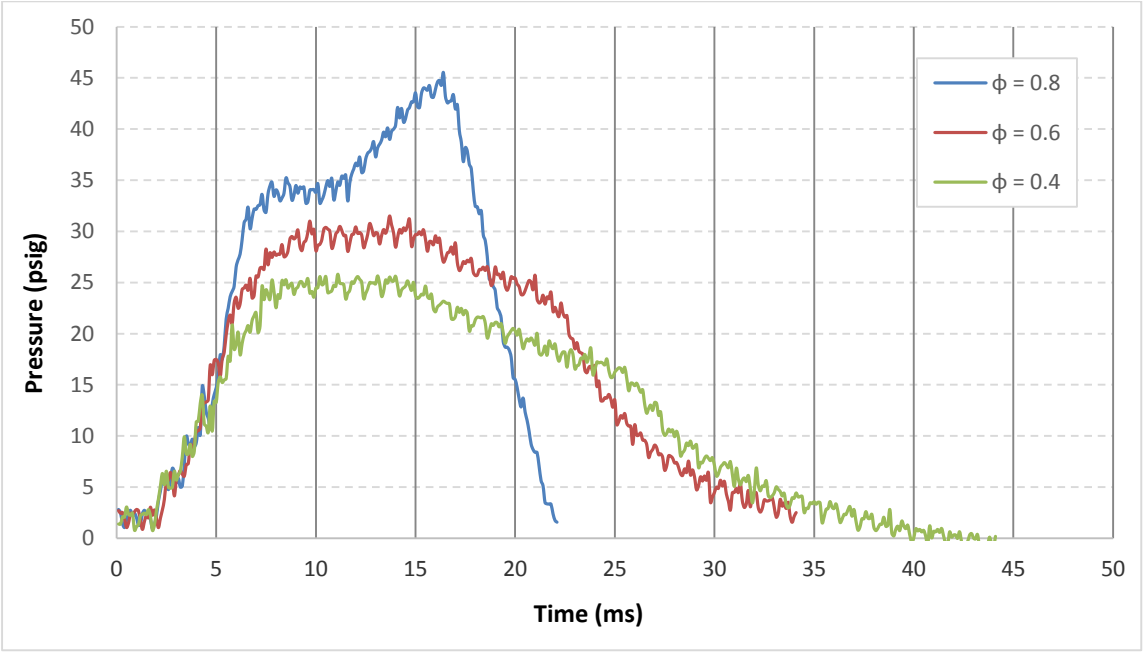

Figure 5. 28 Pressure history comparison at PT2 for hydrogen blended methane mixtures across different equivalence ratios for 8.1 ms nozzle traverse time (Φ = 0.8 (B-0.8-8.1-2), Φ = 0.6 (B-0.6-8.1-3) and Φ = 0.4 (B-0.4-8.1-3))

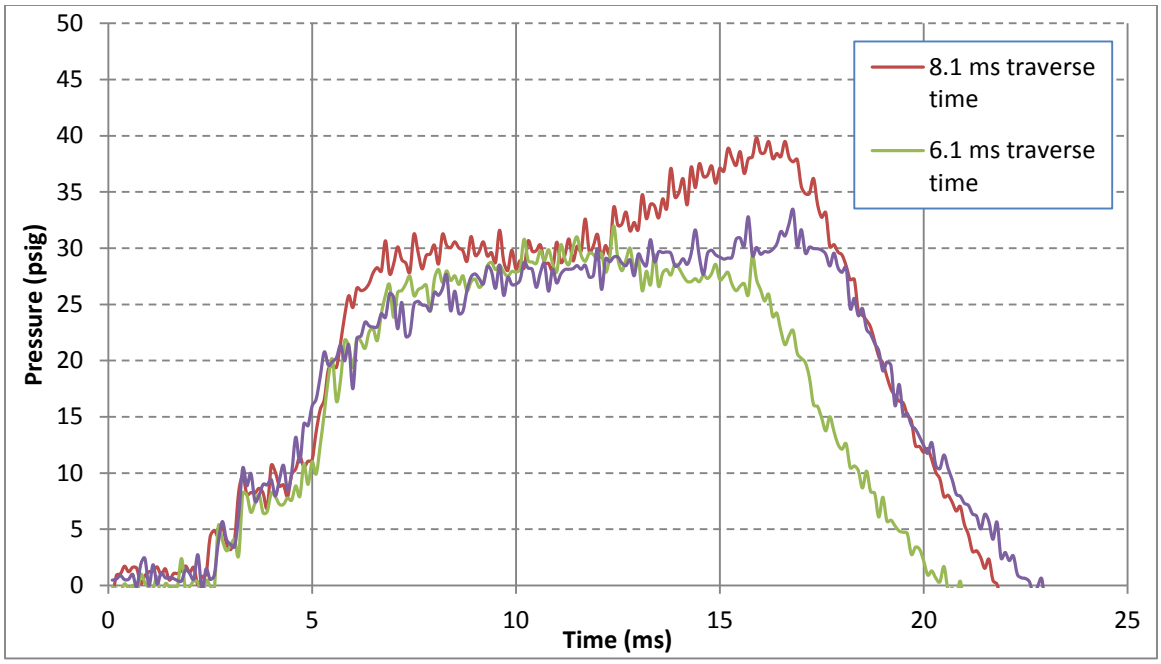

Figure 5. 29 Pressure history comparison at PT1 for hydrogen blended methane mixtures at Φ = 0.8 for traverse speeds of 8.1 ms (B-0.8-8.1-2), 6.1 ms (B-0.8-8.1-2) and 4.9 ms (B-0.8-4.9-1)

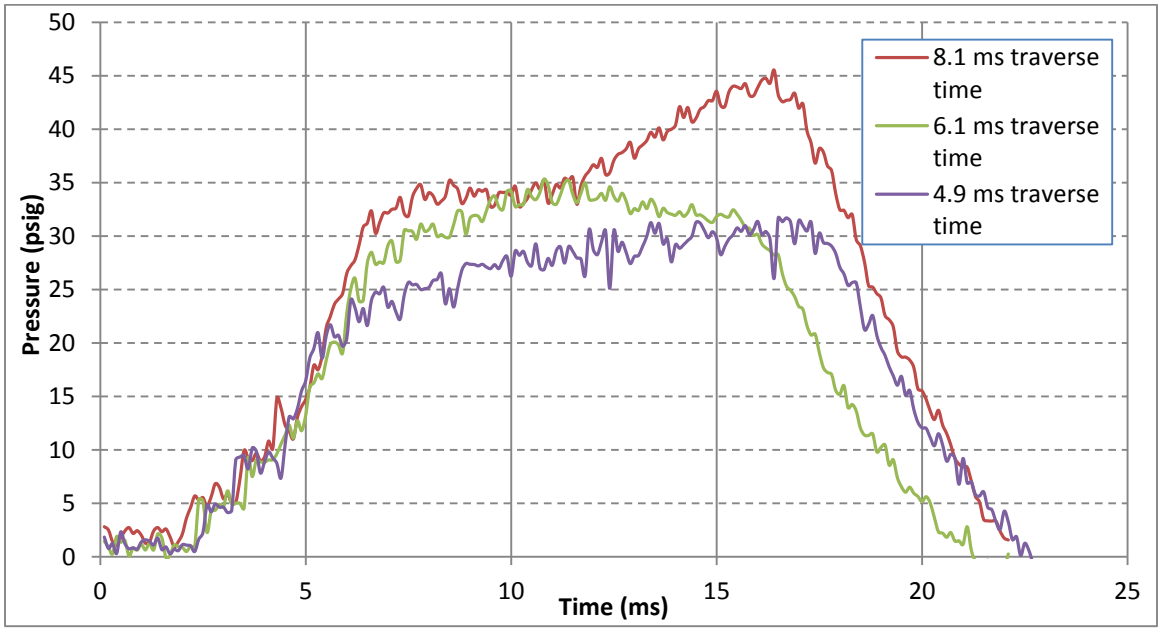

Figure 5. 30 Pressure history comparison at PT2 for hydrogen blended methane mixtures at Φ = 0.8 for traverse speeds of 8.1 ms, 6.1 ms and 4.9 ms

5.5 Image and Pressure Trace Comparison across Different Fuels

The ignition zones for pure methane and hydrogen-enriched methane have been compared for equivalence ratio of Φ = 0.8 and jet traversing in 40.6 ms in Figure 5.31. It is noticed that for both the fuels, the ignition zone tends to move towards the bottom wall of the CVC chamber, where ignition occurs. Figure 5.31 also indicates that the flame propagation is faster in the hydrogen-enriched methane mixture as compared to pure methane-air combustion. The results corresponding to pure methane and hydrogen-enriched methane mixture (Φ = 0.8 and spin rate at 750 rpm) are presented in Figure 5.32. It is observed that the location of the ignition zone was consistent for pure methane and hydrogen blended methane mixtures for fixed equivalence ratio and traverse speed, but the ignition delay time was lower.

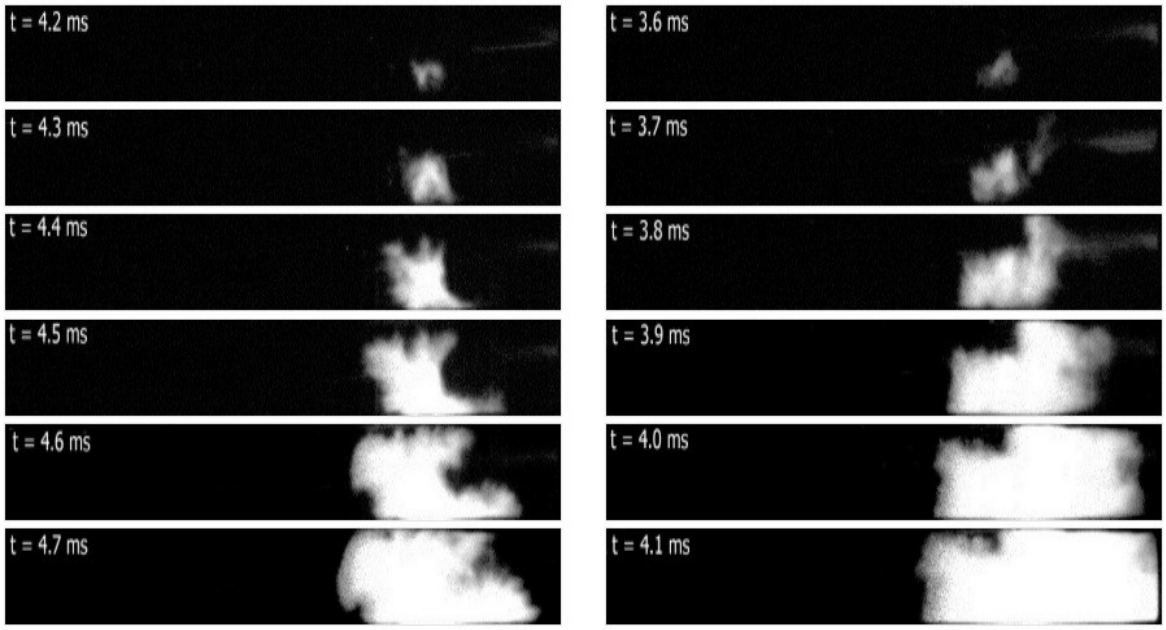

Figure 5. 31 Traversing jet ignition of methane at Φ = 0.8 (left) and hydrogen-enriched methane Φ = 0.8 (right) for hot-jet traverse time of 40.6 ms

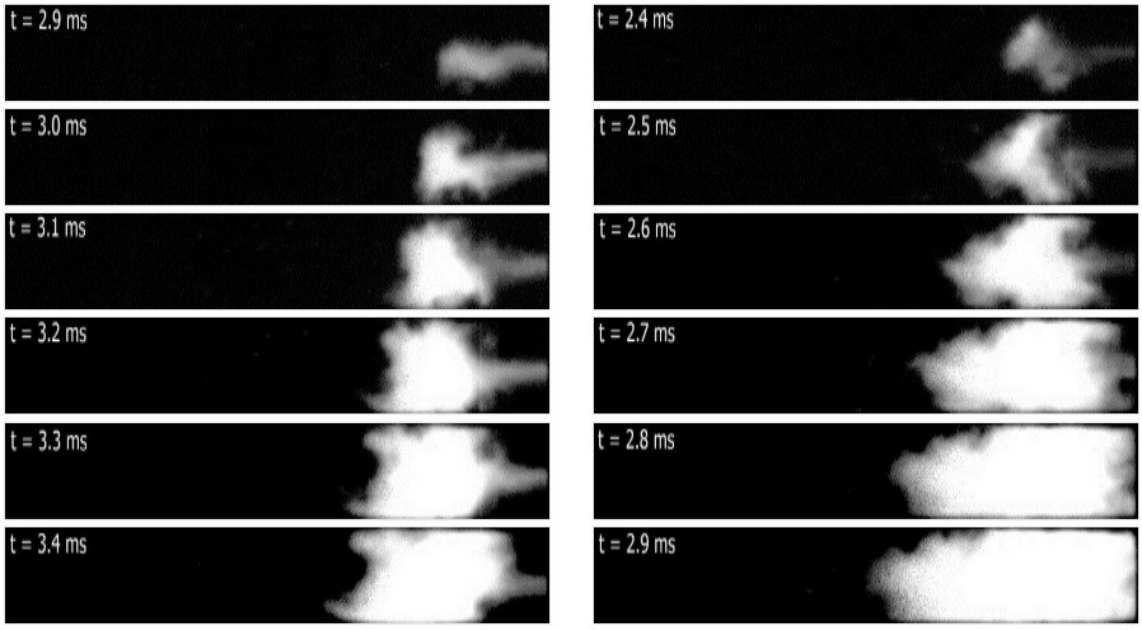

Figure 5. 32 Traversing jet ignition of methane at Φ = 0.8 (left) and hydrogen-enriched methane Φ = 0.8 (right) for hot-jet traverse time at 8.1 ms

Figure 5.33 and Figure 5.34 compares ignition behavior of three different fuels in terms of pressure rise. All three fuels are ignited with a jet moving at 8.1 ms speed and maintained at an equivalence ratio of 0.8. Higher peak pressure level and at the same time more rapid increase in pressure during the time of ignition is exhibited by ethylene. While comparing hydrogen blended methane mixture with ethylene the pressure rise is similar after the period of rapid rise. The trace for ethylene remains flat and then increases after 5 ms. Methane behaves differently here and is more flat through the period after the rapid rise. These traces are clear indication of enhancement of ignition behavior in pure methane mixtures by blending it with hydrogen. Apart from reducing the time delay there is benefit in terms of peak pressure rise.

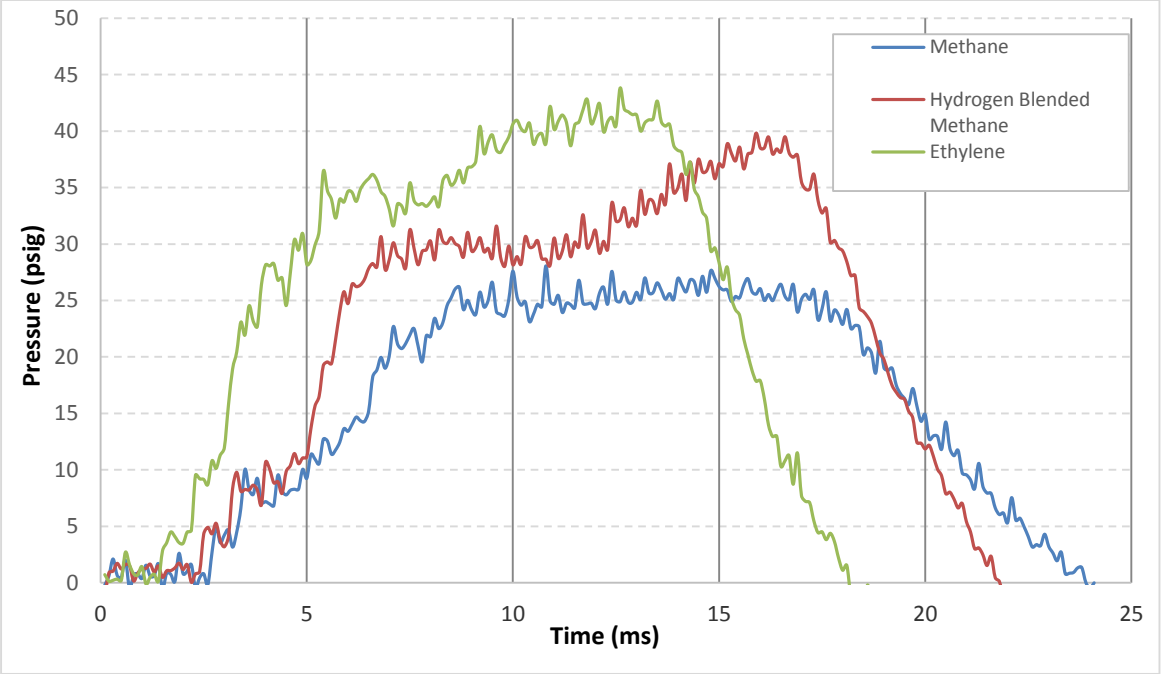

Figure 5. 33 Pressure history Comparison at PT1 across different fuels at Φ = 0.8, Methane (M-0.8-8.1-3), Hydrogen Blended Methane (B-0.8-8.1-2), and Ethylene (E-0.8-8.1-4) for 8.1 ms nozzle traverse time.

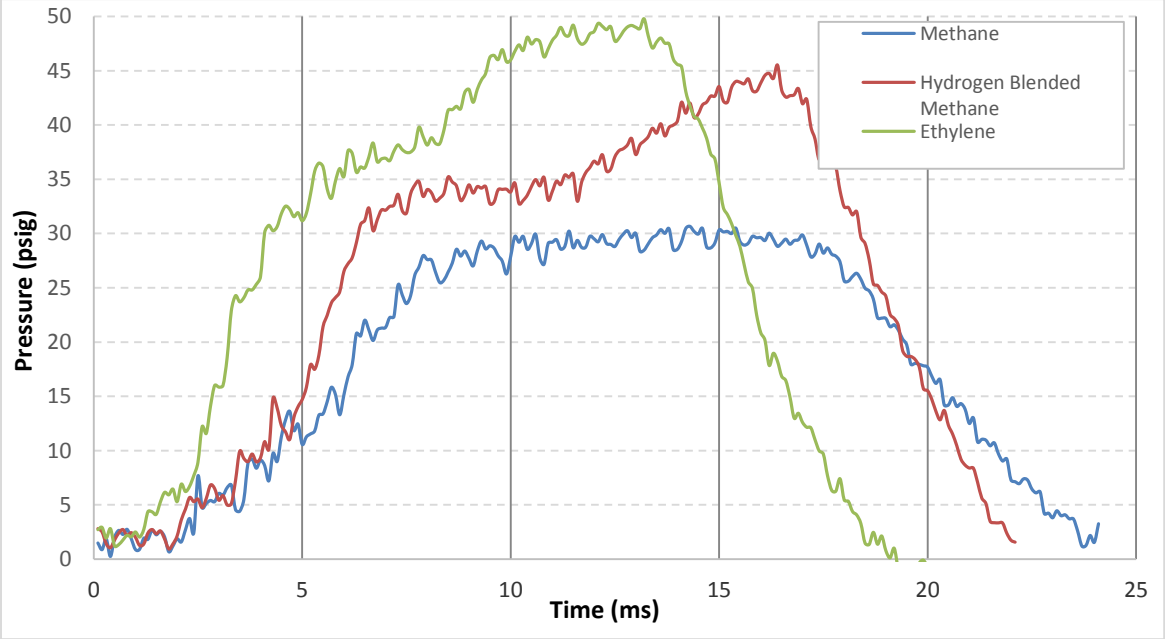

Figure 5. 34 Pressure history Comparison at PT2 across different fuels at Φ = 0.8, Methane (M-0.8-8.1-3), Hydrogen Blended Methane (B-0.8-8.1-2), and Ethylene (E-0.8-8.1-4) for 8.1 ms nozzle traverse time.

5.6 Ignition Delay Time Analysis

This section of the chapter compares the variation of ignition delay times across the fuels tested. The ignition delay time was affected by type of the fuel, equivalence ratio of the main chamber mixture and the traverse speed of the nozzle. Individual effects of all these parameters have been studied by comparing the ignition delay times. Table 5.1, 5.2 and 5.3 gives the overall ignition delay times of all the mixtures studied in this work. Entries in the table indicating 'NA' are the experimental cases where no ignition was detected. Almost all the fuel at $\Phi = 0.4$ failed to ignite past 750 rpm of pre-chamber rotation speed. Even though very few mixtures ignited there was no consistent combustion when the same case was repeated.

5.6.1 Effect on ignition delay time across fuels with fixed traverse time

Figure 5.35 compares ignition delay time of all the fuels at their tested equivalence ratios with nozzle completing its traverse at a time of 40.6 ms across the main chamber entrance. As discussed in previous sections of this chapter the ignition delay time reduced as the mixture became leaner for methane and hydrogen blended methane-air mixtures while the trend was reversed for ethylene-air mixtures. A similar trend was noticed for ignition delay times caused by a jet completing its traverse time in 8.1 ms shown in Figure 5.36. The only noticeable difference is a slight increase in ignition delay time for $\Phi = 0.4$ methane mixtures compared to $\Phi = 0.6$. The ignition delay time for the other nozzle traverse speeds showed a similar trend for all three fuels.

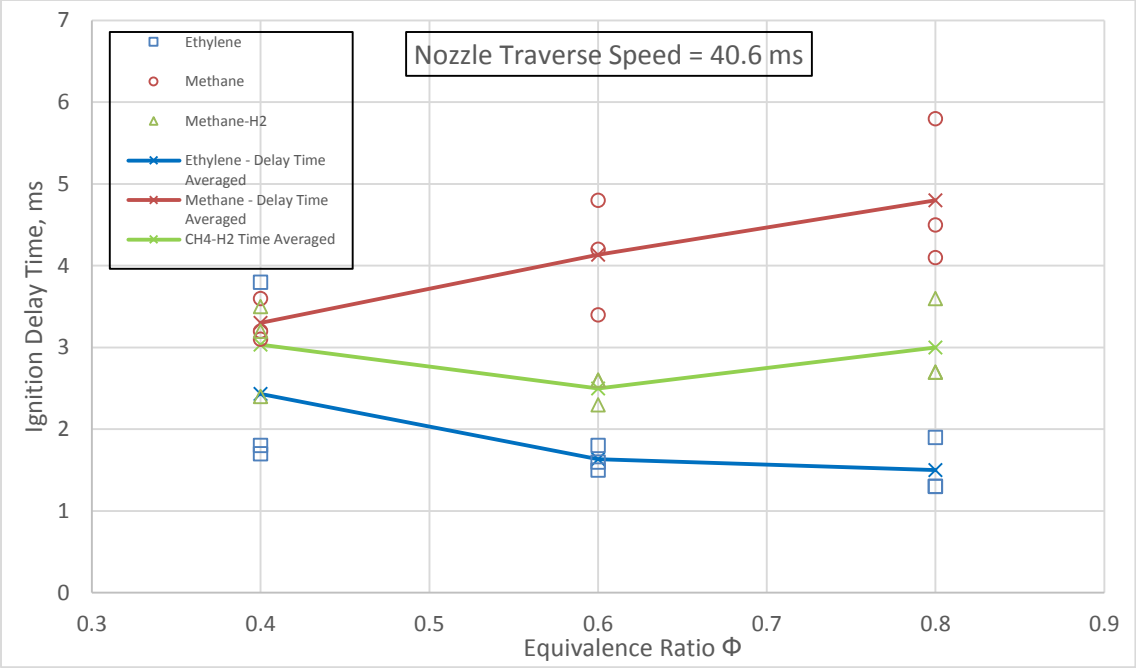

Figure 5. 35 Effect on ignition delay time across equivalence ratios for all fuels with fixed nozzle traverse speed of 40.6 ms

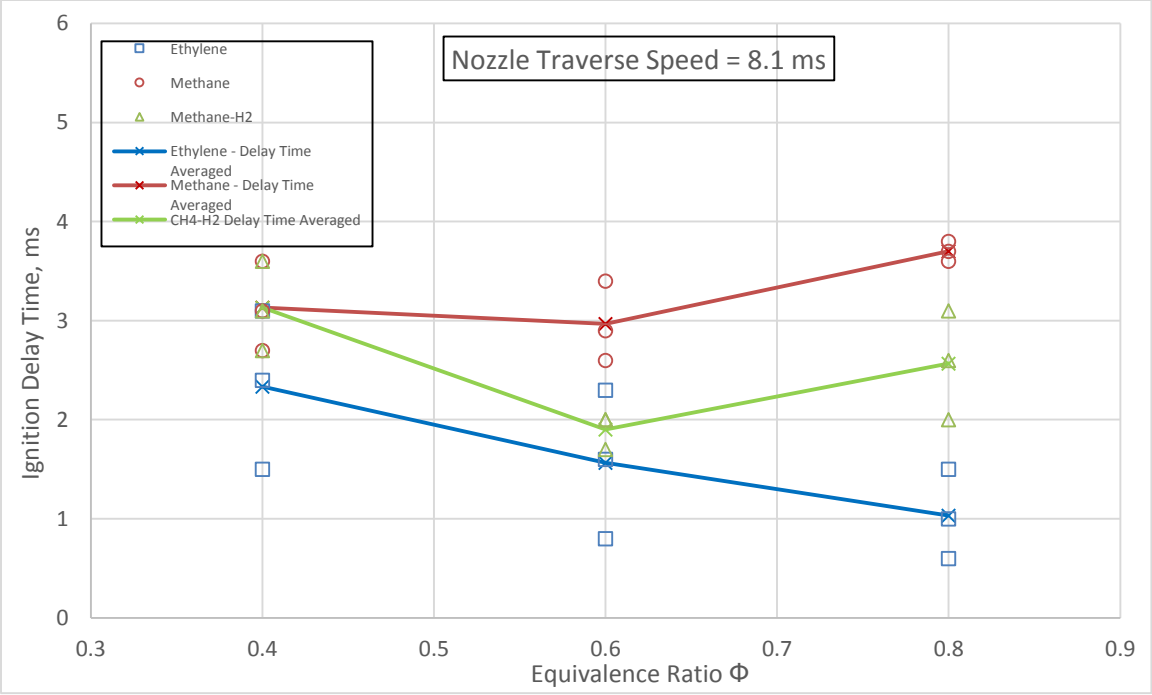

Figure 5. 36 Effect on ignition delay time across equivalence ratios for all fuels with fixed nozzle traverse speed of 8.1 ms

5.6.2 Ignition Delay Time Across Nozzle Traverse Speeds with Fixed Main Chamber Fuel

Figure 5.37, 5.38 and 5.39 attempts to capture the effect of nozzle traverse speed over a single fuel with varying equivalence ratio. All three graphs reveal that ignition delay time reduces as the nozzle traverse speed increases up until the point of 6.1 ms nozzle travel time after which ignition delay time starts to increase. This fact did not change with change in fuel type or change in equivalence ratio. The fundamental reason that a nozzle traverse time of 6.1 ms favoring lower ignition delay time is not clearly understood at this point of time. Although existing, this trend is weakly shown in the plot with ethylene as main chamber fuel. A curve fitting was not attended in this graph due to large spacing between recorded data between 150 rpm and 750 rpm in the x-axis. The curves connecting these points runs through points that are averages of all 3 measured ignition delay times for the same test case. Nonetheless the trend of ignition delay time variation is accurately captured.

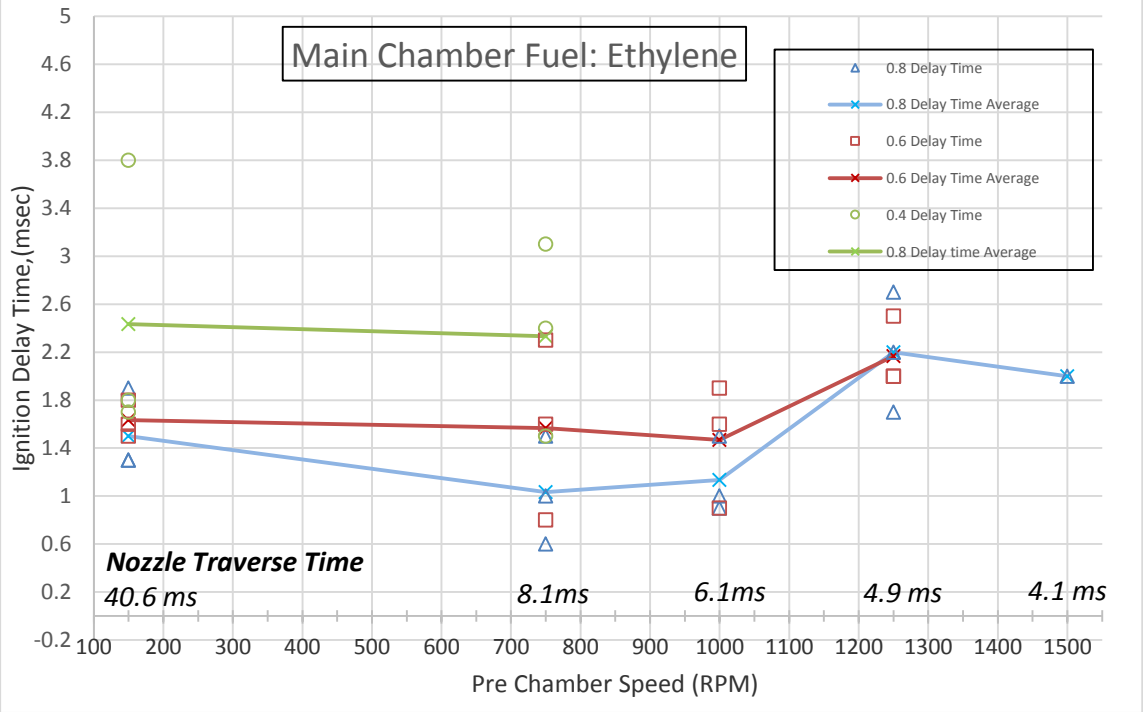

Figure 5. 37 Effect on Ignition delay Time across equivalence ratios for ethylene due to varying nozzle traverse speed

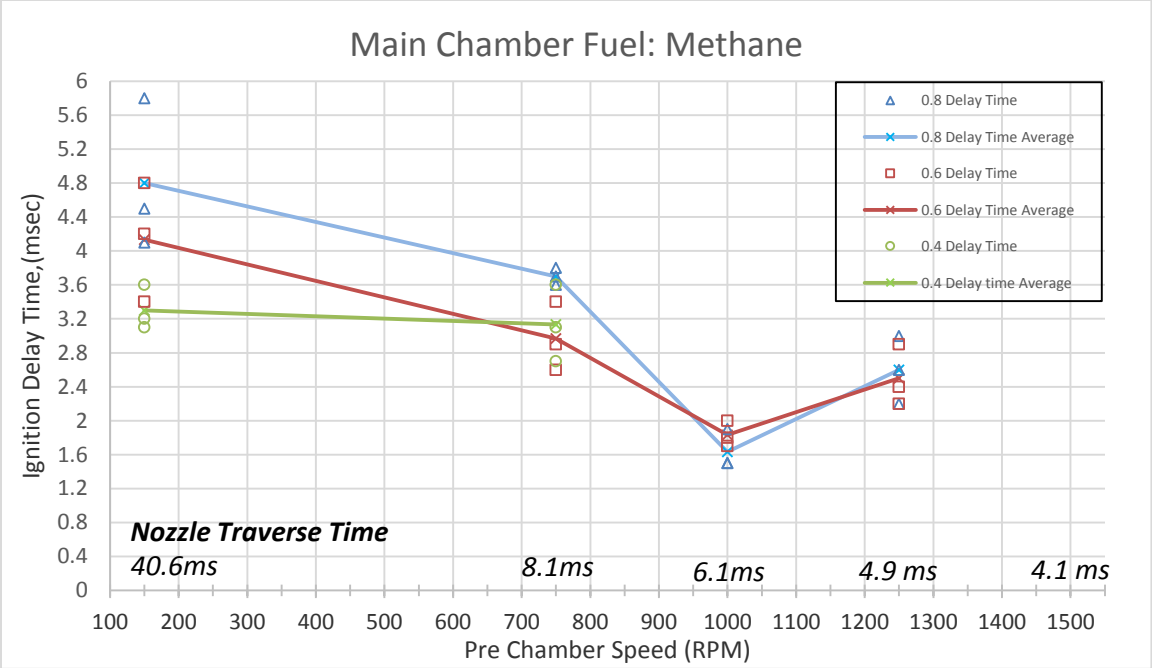

Figure 5. 38 Effect on ignition delay time across equivalence ratios for methane due to varying nozzle traverse speed

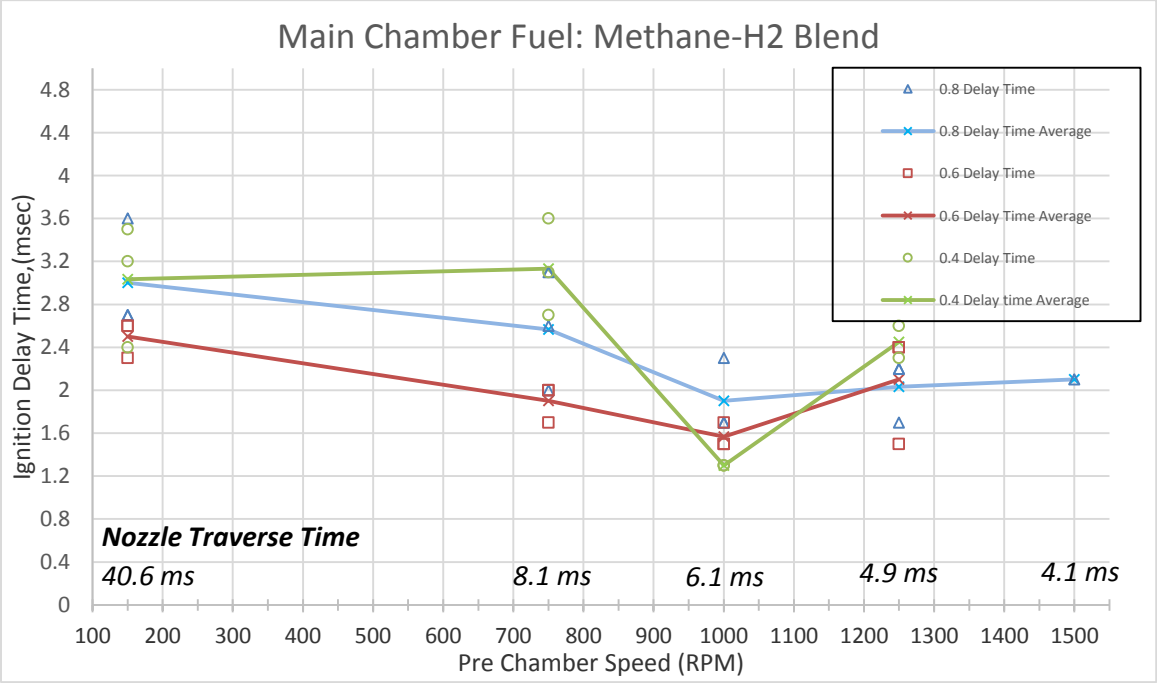

Figure 5. 39 Effect on ignition delay time across equivalence ratios for hydrogen blended methane due to varying nozzle traverse speed

5.6.3 Effect on Ignition Delay Time across Various Nozzle Traverse Speeds with Fixed Equivalence Ratio

The previous discussion holds true for comparing different fuels across different nozzle traverse speeds holding the equivalence ratio fixed. The reduction in ignition delay time with increasing traverse speed can be very clearly seen for Φ = 0.8 mixtures. As could be observed from the graphs only ethylene and hydrogen blended methane mixtures at Φ = 0.8 managed to ignite at 4.1 ms nozzle traverse time. Although the trend indicates rather increasing or nearly equal ignition delay times at 4.1 ms nozzle traverse time, ignition behavior at this traverse speed remains inconclusive due sparse data points.

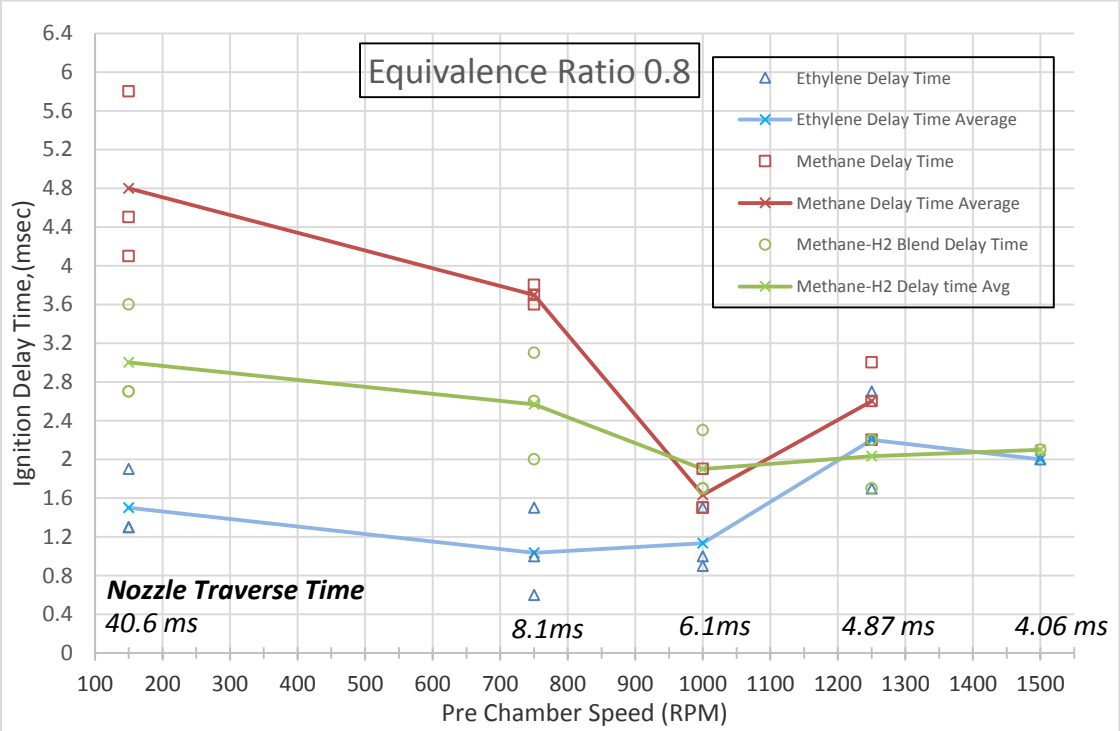

Figure 5. 40 Effect on ignition delay time across different fuels ratios with equivalence ratio of 0.8 due to varying nozzle traverse speed

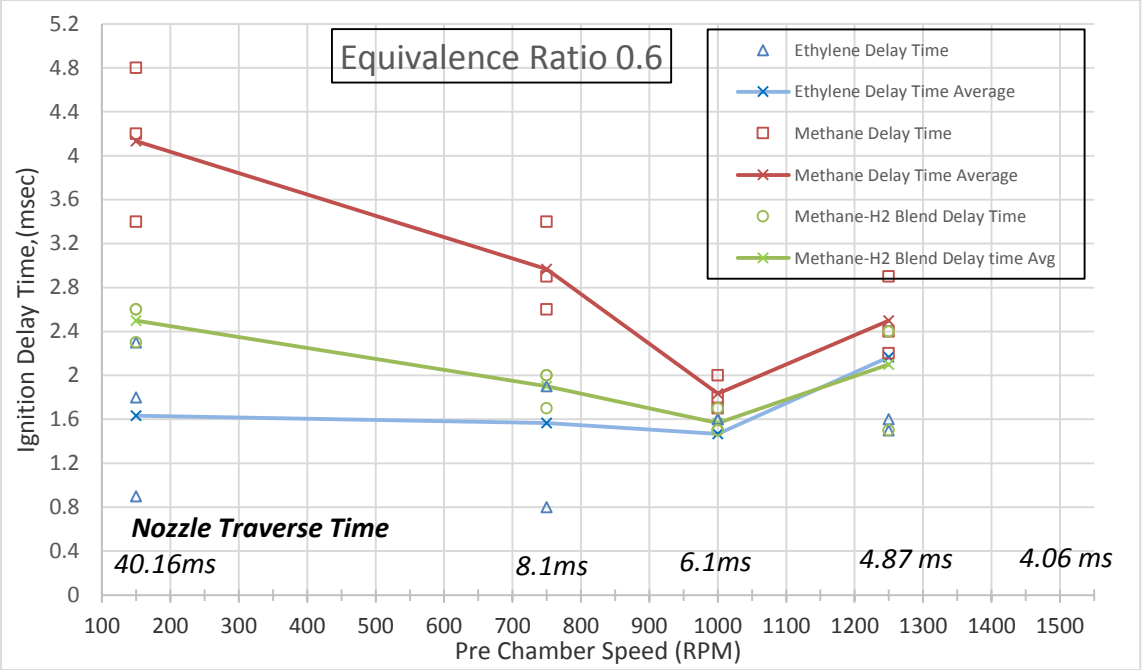

Figure 5. 41 Effect on ignition delay time across different fuels ratios with equivalence ratio of 0.6 due to varying nozzle traverse speed

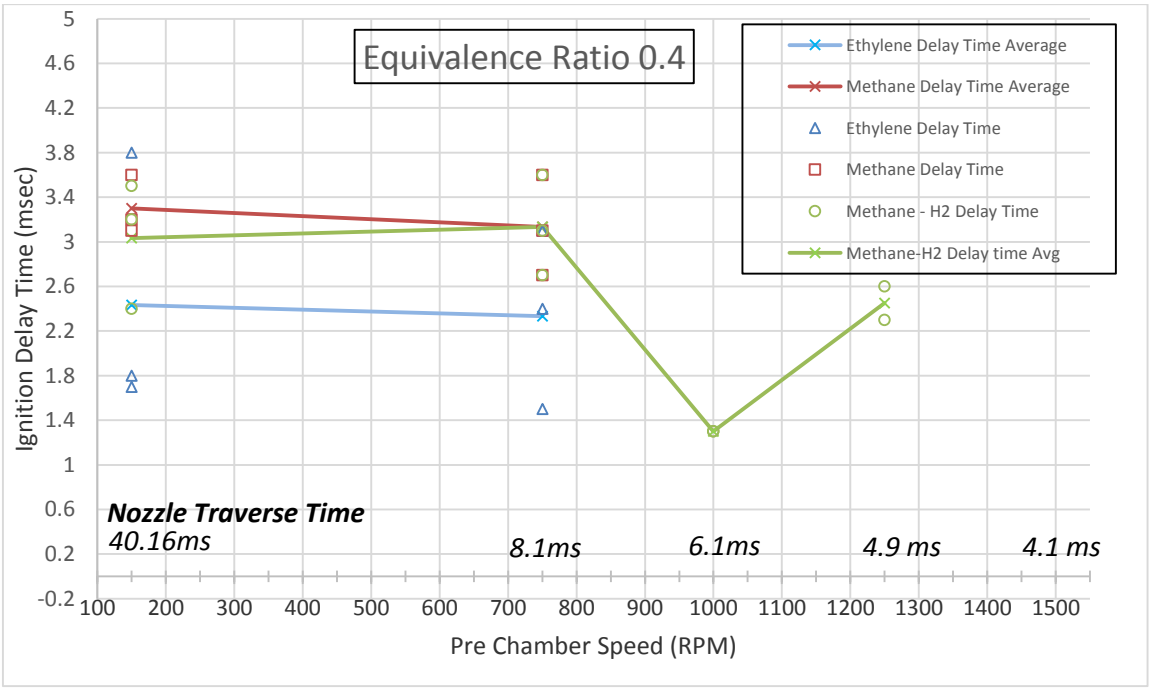

Figure 5. 42 Effect on ignition delay time across different fuels ratios with equivalence ratio of 0.4 due to varying nozzle traverse speed

Although only two data points in terms of ignition delay time were recorded at a pre-chamber rotation speed of 1500 rpm a single test was performed for all equivalence ratios across all three fuels. Multiple attempts had to be made before one successful experiment was performed at this maximum speed attempted due to problems that started in the magnetic pick up coil arrangement which produced inconsistent spark timing. While the pre-chamber is capable of rotating past 2500 rpm independently, the rig produced violent vibrations when a trial run was made at 1750 rpm with the sealing ring assembly and main chamber in place. Plus variation between free pre-chamber speed and the speed measured with the main chamber in place increased which indicates increased drag at higher speeds. The laser tachometer measurements were used to adjust the VFD frequency to attain the required speeds.

This also increased the heat produced as a result of pre-chamber surface rubbing against the O-ring at higher speeds. For one particular endurance test conducted where the pre-chamber was spinning at 1250 rpm in the assembled test setup the pre-chamber heated up to a noticeable level and the plastic O-ring assembly deformed due to this heat. Hence it is not recommended to operate the rig at speeds past 1000 rpm for more than 30 seconds.

6. CONCLUSION AND RECOMMENDATIONS

This chapter includes the concluded remarks for this experimental study and recommendations for future work.

6.1 Conclusions

An experimental methodology was prepared and tests were conducted to investigate the ignition characteristics of traversing hot jets issued in a CVC chamber containing lean air-fuel mixtures, with two hydrocarbon fuels and a hydrocarbon-hydrogen blend fuel. The investigation covered a range of jet traverse times from 40.6 ms to 4.1 ms, the minimum traverse time being limited by the maximum rotation speed capability of the current hardware setup and ignitability of the tested fuels. Methane, ethylene, and a 40:60 blend of hydrogen and methane were used as main-chamber fuels. These were investigated for ignition delay time and ignitability limits under varying equivalence ratios in the lean range for increasing jet traverse speeds.

A visual inspection method and an improved diaphragm preparation technique were proposed and adopted to eliminate failed tests due to improper rupture of the aluminum diaphragm. Test procedures to use blended mixtures in the combustion chambers have been developed. Preliminary experimental methodology to control the start of jet ejection have been tested.

Analysis from the high-speed images revealed that for the case of the ‘near wall’ jet which corresponds to 40.6 ms nozzle traverse time, the ignition location of the fuel were related with the ignition delay times since the jet source was almost stationary and the wall

impinging path remaining fairly constant. In later tests as the jet traverse speed increased, it was seen that the jet still followed the 'near wall' jet path for a certain duration of its traverse time which was clearly noticed in the ethylene-air mixtures tests. The change in ignition location due to change in traverse speeds were more pronounced for methane and hydrogen blended methane-air mixtures compared to ethylene.

Stronger combustion in the main chamber was achieved with slower traverse jet compared to higher speeds as evidenced by the pressure traces and the high-speed images. This indicates that the combustion event was still controlled by jet penetration and amount of hot gas injected even after ignition was initiated. It is assumed that the amount of jet hot gas mass is injected as a function of time is similar for all cases. The effect of traverse time may be understood with respect to prior jet ignition modeling work, which indicates that the mass ratio of entrained fresh mixture and injected hot gas in the vortices created by the jets must be carefully considered. At higher traverse speeds, the amount of hot gas injected into the primary initial vortices may be reduced as the jet moves across and creates multiple vortices.

For the lean mixtures at 0.4 equivalence ratio, the flame propagation event was mostly confined within the penetration distance of the hot jet. This was due to the fact that the mixtures were lean enough to not support a self-supporting flame propagation across the length of the channel. Instead the mixture ignited at multiple points near the jet penetration distance and combustion was confined around that zone.

Ignition delay time analysis across the fuels indicated that for methane and hydrogen blended methane-air mixtures the ignition delay time reduced with reducing equivalence ratios while this behavior was not exhibited by ethylene-air mixture. In general the ignition delay time reduced as the nozzle traverse time decreased up until 6.1 ms traverse time. Further reduction in traverse time resulted in increase in ignition delay times. The ignitability of the mixtures decreased as the traverse time decreased past 6.1 ms. Ignition of methane-air mixtures across all equivalence ratios completely ceased at 4.1 ms

traverse time. From the observed ignitability limits and current hardware capability it was realized that the fuels can be reliably ignited and the rig can be safely operated till 4.9 ms nozzle traverse time. Ignition enhancement was clearly evident due to substitution of hydrogen for methane in the blended mixtures. The supporting pressure traces showed clear distinction across different fuels due to ignition behavior of the fuel itself. The maximum pressure generated was influenced both by main chamber equivalence ratio and jet traverse speed.

6.2 Future Recommendations

The following section discusses on possibilities of improvements that can be made to the rig in terms of hardware modifications and changes in experimental methodology that was realized while conducting this current study.

1. The ignition sites and ignition characteristics at different traverse speeds were controlled by the vortex evolution process which was not visualized using the current high-speed imaging setup. The current main chamber design allows Schlieren imaging to be used which can shed light on the mixing process across the two gases at different densities. Further quantitative data can be obtained by using laser diagnostics in the form of Particle Image Velocimetry (PIV) or an advanced Planar Laser Induced Flourescence (PLIF) setup that can be used to gather insight on species evolution time history for this radical laden combustion process.

2. The current set of dynamic pressure transducers though suitable for high temperature and high pressure combustion applications exhibited sharp thermal drift effects due to interaction with flame and high temperature gases that was developed due to the ignition process. The thermal drift effect can be reduced by applying manufacturer recommended gel based compounds over the face of the transducer before starting an experiment. A methodology to access the pressure transducers in the main chamber and to perform the recommended procedure had to be developed and realized.

3. Although the failure of tests due to improper rupture of the diaphragm was eliminated by using a visual inspection technique the diaphragm rupture time variation due to variation in depth of scoring across different diaphragms was not controlled. An improvement from this manual scoring method can eliminate the variation in diaphragm time that results from varying depths of score in the aluminum diaphragm. This would enable better control on jet ejection location and time for the traversing hot jet experiments.

4. The alignment of chamber axis and parallelism of the chamber mating surfaces is imperfect, resulting in poor sealing during rotation. Each contribution to misalignment should be carefully measured, and the rig should be rebuilt to significantly improve the seal. The main chamber clamping should also be improved to reduced movement due to the recoil force of combustion pressure, which currently results in breaking of the seal and loss of the sealing O-ring in each test.

5. Excessive noise in the electrical systems of the rig interfered in triggering of pressure transducer by spark signal. The National Instruments hardware triggered at times due to disturbances created by turning on the ignition key and switching on the electric motor. Sources of the noise had to be examined and eliminated to allow for precise triggering of pressure recording due to the voltage peak produced by the spark trigger event.

6. The magnetic pick up sensor on the spark trigger setup had to be analyzed to correct the faulty spark trigger event that occurred when the pre chamber was spinning at 1500 rpm which resulted in wrong spark timing across various tests. An attempt made to run the rig at 1750 rpm with the main-chamber and pre-chambers set in place resulted in vibrations indicating balancing problems in the rig. Proper balancing procedures needed to be established and executed to operate the rig at higher speeds than realized in the current study.

7. The heat generated due to drag between the pre-chamber face and sealing ring assembly can significantly increase at speeds past 1000 rpm. An improved lubrication strategy and respective design changes can be implemented to reduce the friction effects at high pre chamber speeds.

8. A three-dimensional computational fluid dynamics (CFD) model with appropriate initial conditions as seen in the experiments needs to be developed and correlated with the experimental results. This can be used to make informed decisions on developing the design of experiments for the future, hence reducing the number of experimental tests that are needed to be performed.

LIST OF REFERENCES

LIST OF REFERENCES

[1] A. A. Boretti, M. J. Brear, and H. C. Watson, "Experimental and Numerical Study of A Hydrogen Fuelled I.C Engine Fitted With the Hydrogen Assisted Jet Ignition System," in *16th Australian Fluid Mechanics Conference*, Crown Plaza, Gold Coast, Australia, 2007, pp. 1142-1147.

[2] D. M. Hensinger, J. A. Maxson, K. Hom, and A. K. Oppenheim, "Jet Plume Injection and Combustion," *SAE International,* 1992.

[3] W. P. Attard and P. Parsons, "A Normally Aspirated Spark Initiated Combustion System Capable of High Load, High Efficiency and Near Zero NOx Emissions in a Modern Vehicle Powertrain," *SAE International,* 2010.

[4] K. Kailasanath, "Recent Developments in the Research on Pulse Detonation Engines," *AIAA Journal,* vol. 41, pp. 145-159, 2003.

[5] D. H. Lieberman, K. L. Parkin, and J. E. Shepherd, "Detonation Initiation By A Hot Turbulent Jet For Use In Pulse Detonation Engines," in *38th Joint Propulsion Conference*, Indianapolis, IN, 2002.

[6] V. I. Tarzhanov, I. V. Telichko, V. G. Vil'danov, V. I. Sdobnov, A. E. Makarov, S L Mukhin, I. G. Koretskii, V. A. Ogarkov, V. V. Vlasov, A. D. Zinchenko, A. V. Vorob'ev, A. N. Grachev, V. A. Matkin, and V. A. Potashnikov, "Detonation of Propane-Air Mixtures under Injection of Hot Detonation Products," *Combustion Explosion and Shock Waves,* vol. 42, pp. 336-345, 2006.

[7] Y. Matsutomi, S. E. Meyer, S. D. Wijeyakulasuriya, Z. Izzy, M. R. Nalim, M. Shimo, M. Kowalkowski, and P. H. Snyder, "Experimental Investigation on the Wave Rotor Combustor," in *46th Joint Propulsion Conference*, Nashville, TN, 2010.

[8] P. Akbari and M. R. Nalim, "Review of Recent Developments in Wave Rotor Combustion Technology," *AIAA Journal of Propulsion & Power,* vol. 25, pp. 833-844, 2009.

[9] M. R. Nalim, "Assesment of Combustion Modes for Internal Combustion Wave Rotor," *Journal of Engineering for Gas Turbines and Power,* vol. 121, 1999.

[10] E. Toulson, H. J. Schock, and W. P. Attard, "A Review of Pre-Chamber Initiated Jet Ignition Combustion Systems," *SAE Paper* p. 2263, 2010.

[11] G. G. Dober and H. C. Watson, "Modelling the Flame Enhancement of a HAJI Equipped Spark Ignition Engine," *IPC-10 Proceedings Paper Number 99091,* 1999.

[12] W. P. Attard, J. Kohn, and P. Parsons, "Ignition Energy Development for a spark initiated combustion system capable of High Load, High Efficiency and Near Zero NOx Emissions," *SAE International,* 2010.

[13] S. D. Wijeyakulasuriya, "Transient and Translating Gas Jet Modelling for Pressure Gain Combustion Applications," Doctor of Philosophy, Purdue University, West Lafayette, Indiana, 2011.

[14] W. P. Attard and P. Parsons, "Flame Kernel Development for a Spark Initiated Pre Chamber Combustion System capable of High Load, High Efficiency and Near Zero NOx Emissions," *SAE International,* 2010.

[15] I. U. Perera, "Experimental Investigation into Combustion Torch Jet Ignition of Methane-Air, Ethylene-Air, and Propane-Air Mixtures," MS Thesis, Purdue University, Indianapolis, 2010

[16] M. Bilgin, "Stationary and Rotating Hot Jet Ignition and Flame Propagation In a Premixed Cell," Ph.D. Dissertation, Aeronautics and Astronautics Dept, University of Washington, Seattle, WA, 1998.

[17] S. D. Wijeyakulasuriya and M. R. Nalim, "Transient Translating Gas Jets in Confined Channels," presented at the 45th AIAA/ASME/SAE/ASEE Joint Propulsion Conference & Exhibit, Denver, Colorado, 2009.

[18] M. Bilgin, J. J. Keller, and R. E. Breidenthal, "Ignition and Flame Propagation with Rotating Hot jets In a Simulated Wave Engine Test Cell," *AIAA Paper 98- 3399,* 1998.

[19] D. Baronia, "Numerical Analysis of Hot Jet Injection and Premixed Flame Propogation in a Channel,"MS Thesis, Mechanical Engineering, IUPUI, 2006.

[20] A. Karimi, M. Rajagopal, and R. Nalim, "Traversing Hot-Jet Ignition In A Constant-Volume Combustor," in *Proceedings of ASME Turbo Expo 2013 GT2013*, San Antonio, Texas, USA 2013.

[21] A. Ungut and P. J. Shuff, "Deflagration to detonation transition from a venting pipe," *Combustion Science and Technology,* pp. 75-87, 1989.

[22] R. Sadanandan, D. Markus, R.Schiebl, and U.Mass, "Mixture Fraction Measurements During the Hot-Jet Ignition of Hydrogen/Air Mixtures," presented at the Proceedings of European Combustion Meeting, 2005.

[23] R. Sadanandan, D. Markus, R.Schiebl, U.Mass, J.Olofsson, H. Seyfried, M. Richter, and M. Alden, "Detailed Investigation of Ignition by Hot gas Jets," *Proceedings of the Combustion Institute,* pp. 719-726, 2007.

[24] H. Tsuji, "Ignition and Flame Stabilization of Stream of Combustible Gaseous Mixtures by Hot Jet," Aeronautical Research Institute, University of Tokyo 357, 1960.

[25] H. G. Wolfhard, "The Ignition of Combustible Mixtures by Hot Gases," *Jet Propulsion,* vol. 28, pp. 798-804, 1958.

[26] Z. J. Fink and M. Vanpée, "Overall Kinetics of Hot Gas Ignition," *Combustion Science and Technology,* vol. 11, pp. 229-238, 1975.

[27] F. Mayinger, M. Jordan, A. Eder, I. S. Zaslonko, V. P. karpov, and S. M. Frolov, "Flame-Jet Ignition of fuel-Air Mixtures. Experimental Findings and Modeling," in *17th International Colloquium on the Dynamics of Explosions and Reactive Systems (ICDERS)*, ed. Heidelberg, Germany, 1999.

[28] L. A. Gussak and V. P. Karpov, "The application of LAG process in the pre-chamber engines," *SAE Technical Paper,* 1979.

[29] T. Date and S. Yagi, "Research and Development of Honda CVCC Engine," *SAE Technical Paper,* vol. 740605, 1974.

[30] M. C. Turkish, "3 valve stratified charge engines: Evolvement, Analysis and Progression," *SAE Technical Paper,* vol. 741163, 1974.

[31] E. Murase, S. Ono, K.Hanada, and A. K.Oppenheim, "Pulsed Combustion Jet in Lean Mixtures," 1994.

[32] J. A. Maxson, D. M. Hensinger, K. Hom, and A. K. Oppenheim, "Performance of Multiple Stream Pulsed Jet Combustion Systems," in *SAE International Congress and Exposition*, Detroit, Michigan, 1991.

[33] A. A. Boretti and W. Harry C, "The Lean Burn Direct-Injection Jet-Ignition Flexi Gas Fuel LPG/CNG Engine," *SAE International,* 2009.

[34] A. A. Boretti, "Modelling auto ignition of hydrogen in a jet ignition pre-chamber," *International Journal of Hydrogen Energy,* vol. 35, pp. 3881-3890, 2010.

[35] E. Murase and K. Hanada, "Ignition Timing Control of Homogeneous Charge Compression Ignition Engines by Pulsed Flame Jets," *Combustion Science and Technology,* pp. 129-140, 2002.

[36] W. P. Attard and H. Blaxill, "A Lean Burn Gasoline Fuelled Pre-Chamber Jet Ignition Combustion System Acheiving High Efficiency and Low NOx at Part Load," *SAE International,* 2012.

[37] E. Toulson, H. C. Watson, and W. P. Attard, "Modelling Alternative Prechamber Fuels in Jet Assisted Ignition of Gasoline and LPG," *SAE International,* 2009.

[38] W. P. Attard and H. Blaxill, "A Gasoline Fueled Pre-Chamber Jet Ignition Combustion System at Unthrottled Conditions," *SAE International,* 2012.

[39] T. E, A. Huisjen, X. Chen, C. Squibb, G. Zhu, and H. Schock, "Visualization of Propane and Natural Gas Spark Ignition and Turbulent Jet Ignition Combustion," *SAE International,* 2012.

[40] Z. H. Kyaw and H. C. Watson, "Hydrogen Assisted Jet Ignition for Near Elimination of NOx and Cyclic Variability in the S.I. Engine," presented at the Twenty-Fourth Symposium on Combustion, 1992.

[41] T. M. Elharis, "A Multi-step Reaction Model for Stratified-Charge Combustion in Wave Rotors," MS Thesis, Department of Mechanical Engineering, IUPUI, Indianapolis 2011

[42] S. Wijeyakulasuriya and M. R. Nalim, "Multidimensional Modelling of Gas Mixing in Transient Translating Confined Turbulent Jets," in *49th AIAA Aerospace Sciences Meeting*, Orlando, Florida, 2011.

[43] S. D. Wijeyakulasuriya, I. U. Perera, and M. R. Nalim, "Mixing and Ignition Potential of a Transient Confined Turbulent Jet in a Wave-Rotor Constant-Volume Combustor," in *46th AIAA/ASME/SAE/ASEE Joint Propulsion Conference & Exhibit*, Nashville, TN, 2010.

[44] Y. Matsutomi, C. Hein, C. Lian, S. Meyer, C. Merkle, and S. Heister, "Facility Development for Testing of Wave Rotor Combustion Rig," in *43rd AIAA/ASME/SAE/ASEE Joint Propulsion Conference and Exhibit, AIAA 2007-5052*, Cincinnati, OH, 2007.

[45] *Methodology Manual, Star-CD V .3.20*.(2004).

[46] A. Karimi, P. Chinnathambi, M. Rajagopal, and M. R. Nalim, "Hot-Jet Ignition of Hydrocarbons and Hydrogen in Air: Effect of Jet Chemical Activity," presented at the AIAA-2013-3710, 49th JPC, San Jose, CA, 2013.

[47] A. Karimi, P. Chinnathambi, M. Rajagopal, and M. R. Nalim, "Effect of Jet Composition in Hot-Jet Ignition of Premixed Mixture in a Constant-Volume Combustor " in *8th US National Combustion Meeting*, Park City, UT, 2013.

[48] F. R. Menter, "Two-equation eddy-viscosity turbulence modeling for engineering applications," *AIAA Journal,* vol. 32, pp. 1598-1605, 1994.

[49] D. B. Spalding, "Mixing and Chemical Reaction in Steady Confined Turbulent Flames," *Thirteenth Symposium (International) on Combustion, The Combustion Institute, Pittsburg,PA,* pp. 649-657, 1971.

[50] B. F. Magnussen and B. H. Hjertager, "Development of the eddy-break-up model of turbulent combustion," *Sixteenth Symposium (International) on Combustion, The Combustion Institute, Pittsburgh, PA,* pp. 719-729, 1976.

[51] K. Murphy, "Experimental Investigation of Traversing Hot-Jet Ignition of Ethylene, and Propane-Air Mixtures in a Constant-Volume Combustor," M.S.M.E Thesis, Department of Mechanical Engineering, Purdue University, Indianapolis,unpublished.

[52] K. Lee, K. Y. Bang, and G. Mortazavi, Summer MURI Report 2012 " Design of Safe Electrical System for Wave Rotor Igniter Experiment ", CPRL,IUPUI,2012.

[53] W. P. Attard, E. Toulson, A. Huisjen, X. Chen, G. Zhu, and H. Schock, "Spark Ignition and Pre-Chamber Turbulent Jet Ignition Combustion Visualization," *SAE International,* 2012.

[54] J. A. Baker and G. B. Skinner, "Shock-Tube Studies on the Ignition of Ethylene-Oxygen-Argon Mixtures," *Combustion and Flame,* vol. 19, pp. 347-350, 1972.

[55] F. D. Davidson and K. R. Hanson, "Interpreting Shock Tube Ignition Data," *International Journal of Chemical Kinetics,* vol. 36, pp. 510-523, 2004.

[56] R. F. Fristrom and A. A. Westenberg, *Flame Structure*. New York: McGraw-Hill, 1965.

[57] A. S. Sokolic, *Gas sampling and chemical analysis in combustion process*: Pergamon Press, 1963.

[58] C. F. U. Tipper, *Oxidation and Combustion Reviews*, 1965.

[59] A. G. Merzhanov, "The present state of Thermal Ignition Theory," *Combustion and Flame,* vol. 16, 1971.

[60] M. Vanpée and G. H. Wolfhard, "Comparison between Hot Gas Ignition and Limit Flame Temperatures," *ARS JOURNAL,* vol. 29, pp. 517-519, 1959.

[61] R. J. Cato and J. M. Kuchta, "Hot Gas Ignition Temperatures of Hydrocarbon Fuel Vapor-Air Mixtures," *Bureau of Mines,* vol. AD0643518, 1966.

[62] W. L. Grosshandler, "RADCAL: A Narrow-Band Model for Radiation Calculations in a Combustion Environment," in *NIST Technical Note 1402*, Springfield, VA, 1993.

[63] C. E. Baukal, "Heat Transfer Modes," presented at the Heat Transfer in Industrial Combustion, CRC press, Florida, 2000.

[64] S. Kito, K. Wakai, S. Takahashi, N. Fukaya, and Y. Takada, "Ignition Limit of Lean Mixture by Hydrogen Flame Jet Ingition," *JSAE Review,* vol. 3, pp. 373-378, 2000.

[65] J. R. Parker, "Algorithms for Image Processing and Computer Vision," *New York, John Wiley & Sons, Inc,* pp. 23-29, 1997.

[66] L. Allocoa, F. Catapano, A. Montarano, and P. Sementa, "Study of E10 and E85 Effect on Air Fuel Mixing and Combustion Process in Optical Multicylinder GDI Engine and in a Spray Imaging Chamber " *SAE International,* 04/08/2013 2013.

[67] Y. Hidaka, T. Kataoka, and M. Suga, "A Shock Tube investigation of ignition in Ethylene-Oxygen-Argon Mixtures," *Bulletin of The Chemical Society of Japan,* vol. 47, pp. 2166-2170, 1974.

[68] J. E. BROADWELL and R. E. BREIDENTHAL, "A simple model of mixing and chemical reaction in a turbulent shaer layer," *Journal of Fluid Mechanics,* vol. 125, pp. 397-410, 1982.

[69] P. Akbari and M. R. Nalim, "Analysis of Flow Processes in Detonative Wave Rotors and Pulse Detonation Engines ." in *44th AIAA Aerospace Sciences Meeting, AIAA Paper 2006-1236*, Reno, 2006.

[70] M. R. Nalim and K. Pekkan, "Internal Combustion Wave Rotors for Gas Turbine Engine Enhancement," *ASME Paper IGTC-2003-FR-303,* 2003.

[71] M. R. Nalim, "Assessment of Combustion Modes for Internal Combustion Wave Rotors " *ASME J. of Engineering for Gas Turbines & Power,* vol. 121, pp. 265-271, 1999.

[72] J. Warnatz, U. Maas, and R. W. Dibble, "Combustion: Physical and Chemical Fundamentals, Modelling and Simulation, Experiments, Pollutant Formation," *Springer-Verlag,* 1996.

[73] V. Kilchyk, "Pressure-Wave Amplification of Flame Area in Wave Rotor Channels," PhD Purdue University, West Lafayette, 2009.

[74] V. Kilchyk, M. Nalim, and C. Merkle, "Laminar premixed flame fuel consumption rate modulation by shocks and expansion waves," *Combustion and Flame,* vol. 158, pp. 1140-1148, 2011.

[75] S. O. B. Shrestha and G. A. Karim, "Hydrogen as an additive to methane for spark ignition engine applications " *International Journal of Hydrogen Energy,* pp. 577-586, 1999.

[76] J. L. Gauducheau, B. Denet, and G. A. Searby, "A Numerical Study of lean CH4-H2-air premixed flames at high pressure " *Combustion Science and Technology,* pp. 81-89, 1999.

[77] Y. Ju and T. Niioka, "Ignition simulation of methane/hydrogen mixtures in a supersonic mixing layer " *Combustion and Flame,* vol. 102, pp. 462–470, 1995

[78] E. Toulson, H. C. Watson, and W. P. Attard, "Gas Assisted Jet Ignition of Ultra-Lean LPG in a Spark Ignition Engine," *SAE International,* 2009.

APPENDICES

Appendix A Pre-Chamber and Main Chamber Design Drawings

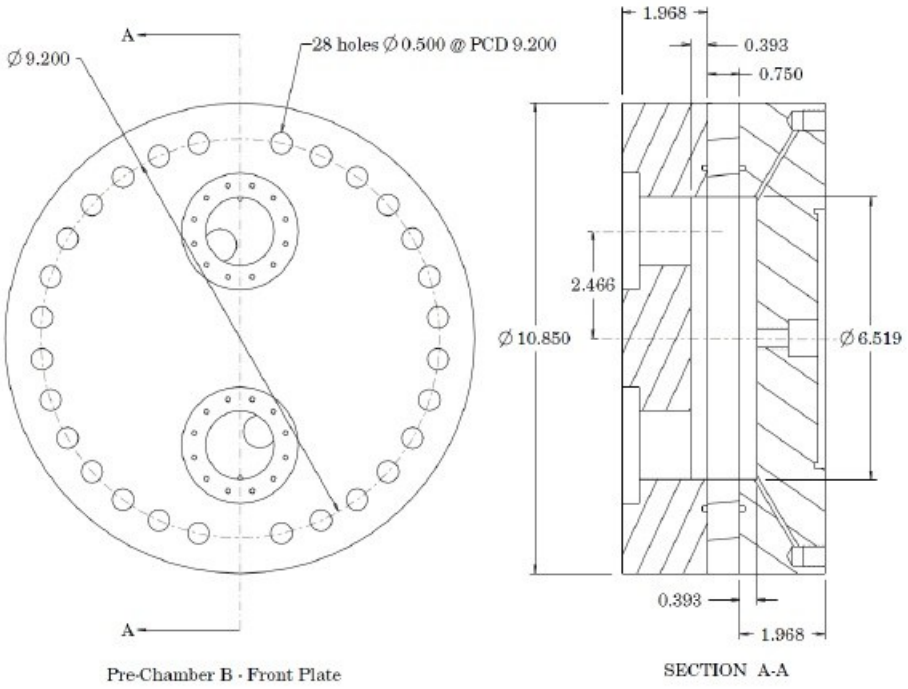

Figure A. 1 Pre-chamber dimensions

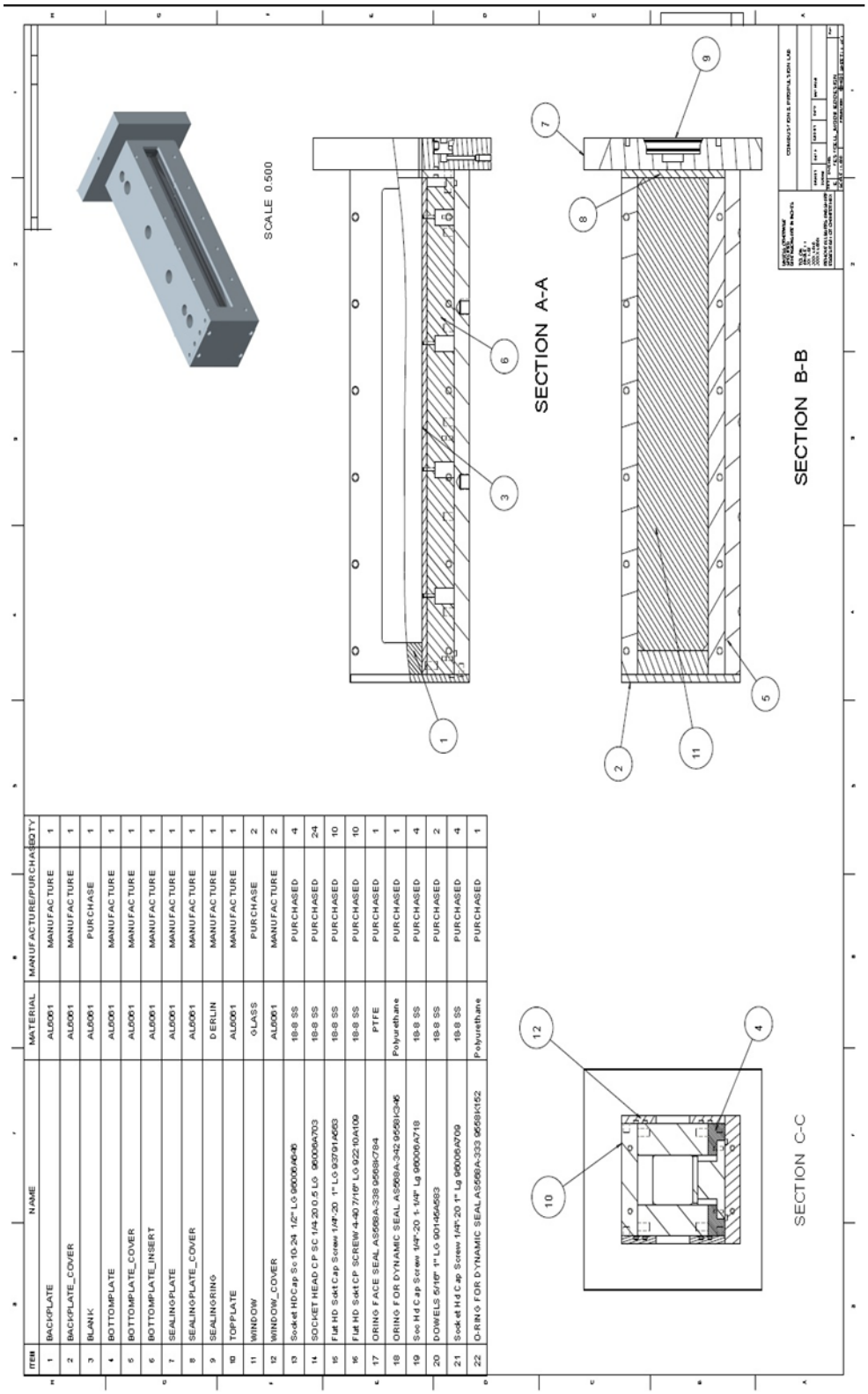

ITEM	NAME	MATERIAL	MANUFACTURE/PURCHASE	QTY
1	BACKPLATE	AL6061	MANUFACTURE	1
2	BACKPLATE_COVER	AL6061	MANUFACTURE	1
3	BLANK	AL6061	PURCHASE	1
4	BOTTOMPLATE	AL6061	MANUFACTURE	1
5	BOTTOMPLATE_COVER	AL6061	MANUFACTURE	1
6	BOTTOMPLATE_INSERT	AL6061	MANUFACTURE	1
7	SEALINGPLATE	AL6061	MANUFACTURE	1
8	SEALINGPLATE_COVER	AL6061	MANUFACTURE	1
9	SEALINGRING	DERLIN	MANUFACTURE	1
10	TOPPLATE	AL6061	MANUFACTURE	1
11	WINDOW	GLASS	PURCHASE	2
12	WINDOW_COVER	AL6061	MANUFACTURE	2
13	Socket HD Cap Sc 10-24 1/2" Lg 90006A245	18-8 SS	PURCHASED	4
14	SOCKET HEAD CP SC 1/4-20 0.5 LG 90006A703	18-8 SS	PURCHASED	24
15	Flat HD Sokt Cap Screw 1/4"-20 1" LG 93791A053	18-8 SS	PURCHASED	10
16	Flat HD Sokt CP SCREW 4-40 7/16" LG 92210A109	18-8 SS	PURCHASED	10
17	ORING FACE SEAL AS568A-338 9568/784	PTFE	PURCHASED	1
18	ORING FOR DYNAMIC SEAL AS568A-342 9568/346	Polyurethane	PURCHASED	1
19	Soc Hd Cap Screw 1/4"-20 1-1/4" Lg 90006A718	18-8 SS	PURCHASED	4
20	DOWELS 5/16" 1" LG 90145A583	18-8 SS	PURCHASED	2
21	Socket Hd Cap Screw 1/4"-20 1" Lg 90006A709	18-8 SS	PURCHASED	4
22	O-RING FOR DYNAMIC SEAL AS568A-333 9568/152	Polyurethane	PURCHASED	1

Figure A. 2 Main chamber assembly with bill of materials

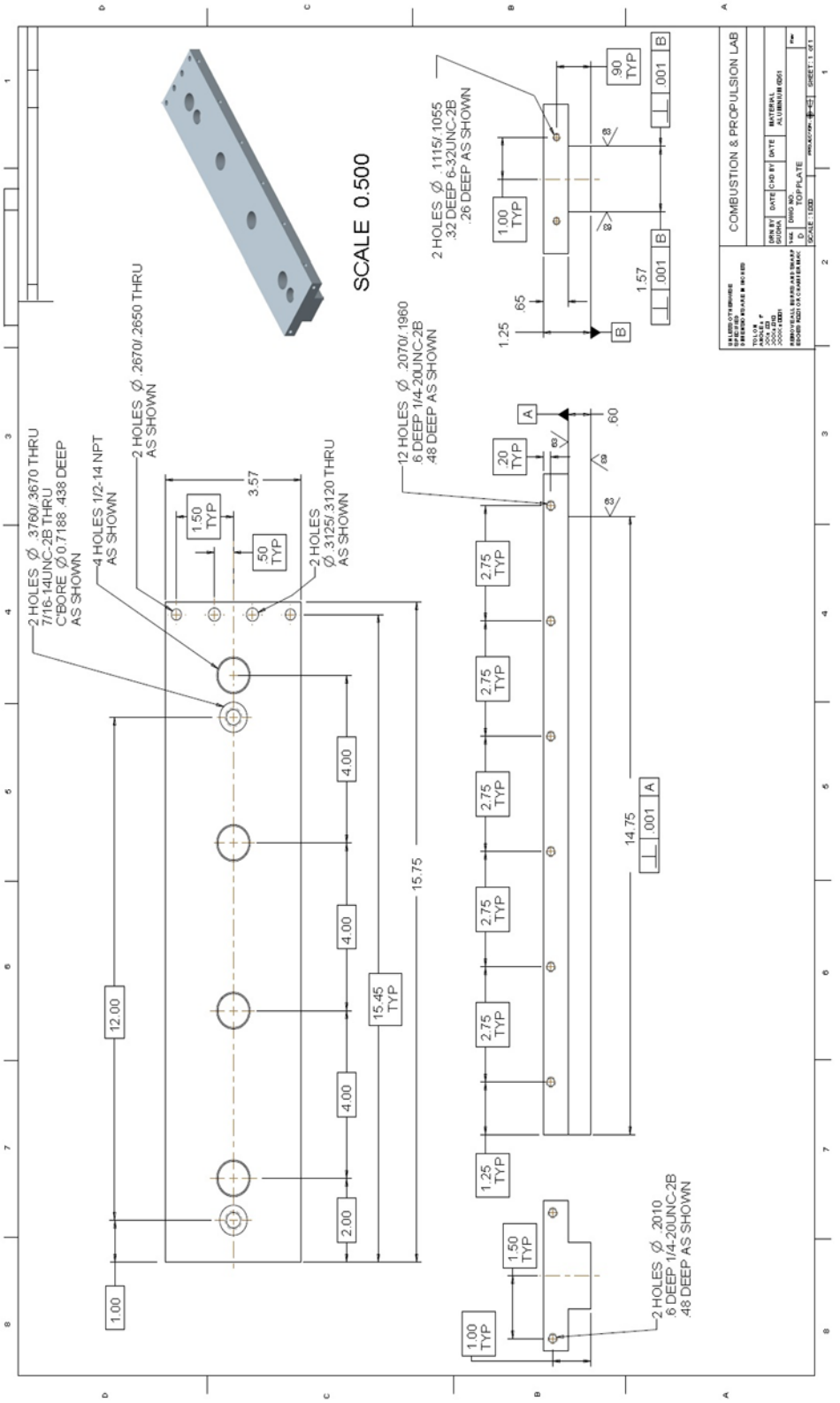

Figure A.3 Top plate part drawing in the main chamber assembly

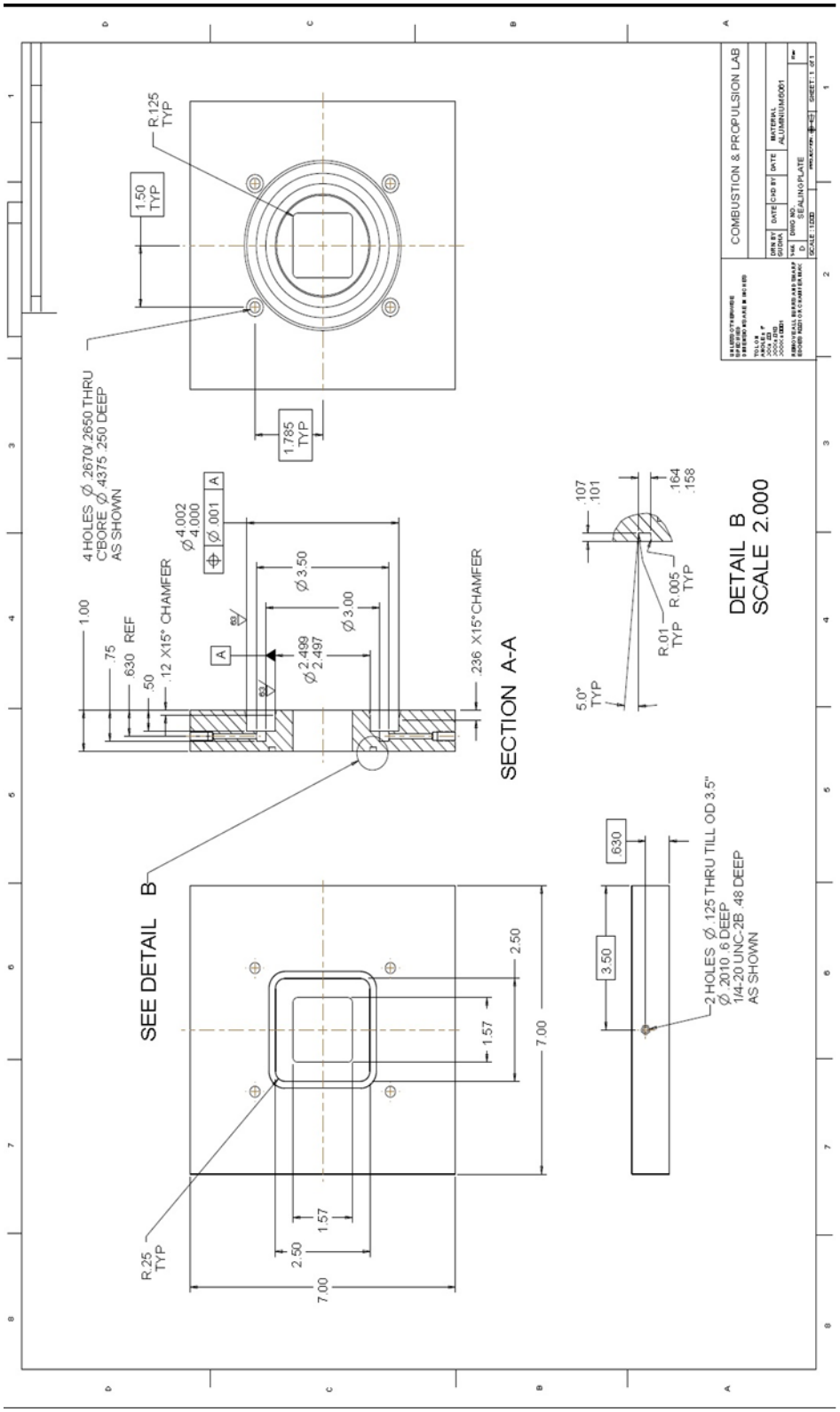

Figure A. 4 Sealing plate part drawing in the main chamber assembly

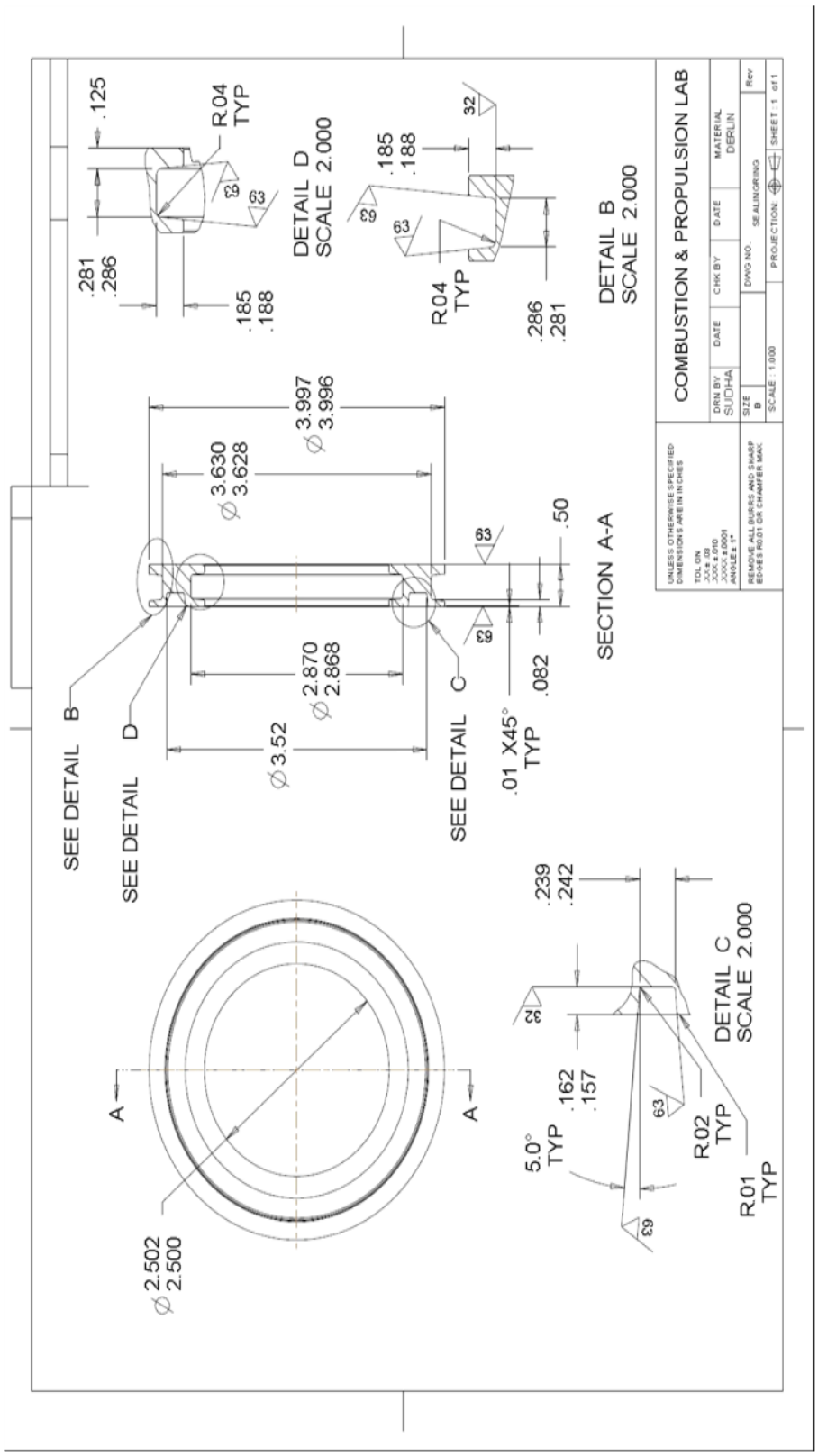

Figure A. 5 Sealing ring part drawing in the main chamber assembly

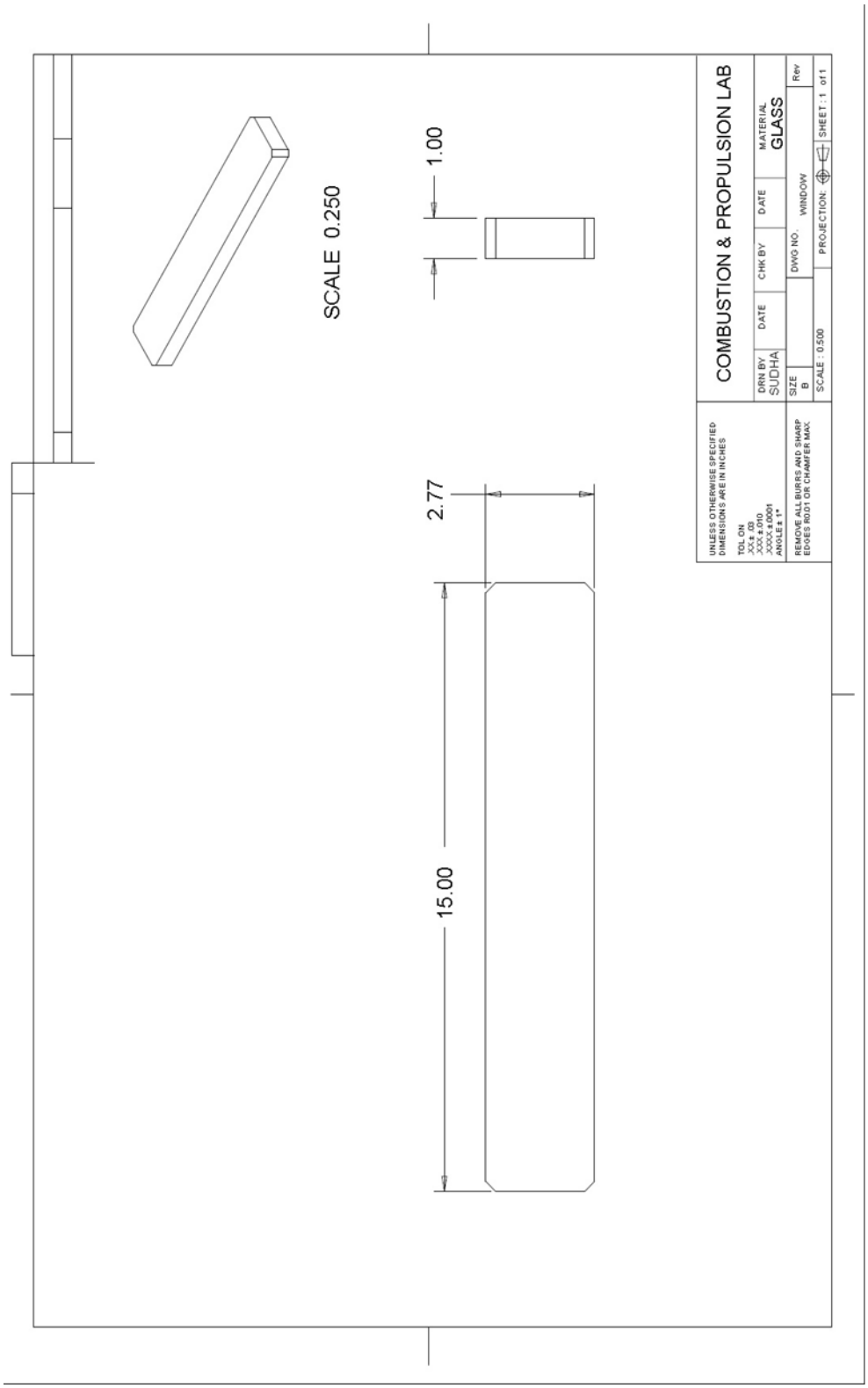

Figure A. 6 Optical window part drawing in the main chamber assembly

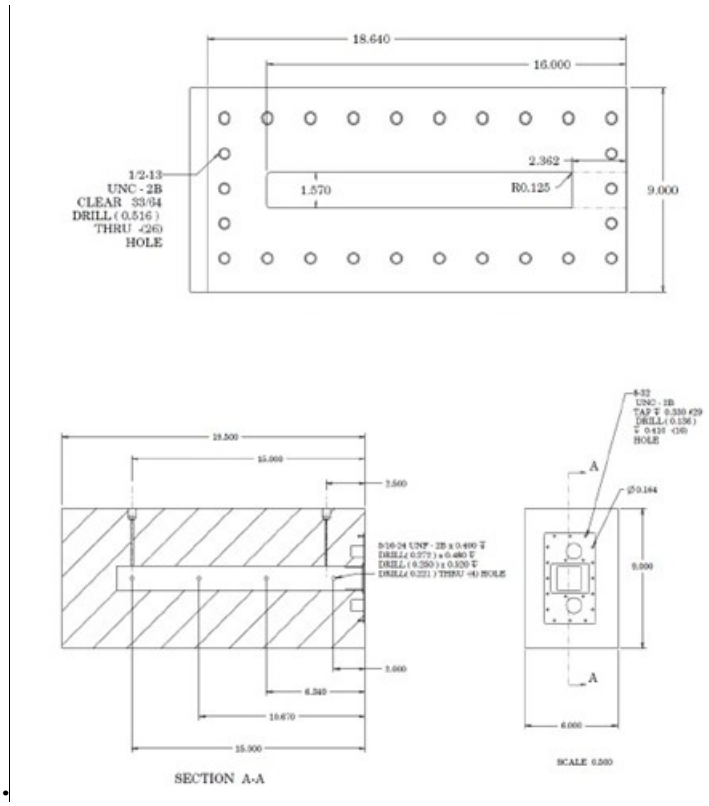

Figure A. 7 Previous version of the main chamber assembly

Appendix B Nozzle Dimensions

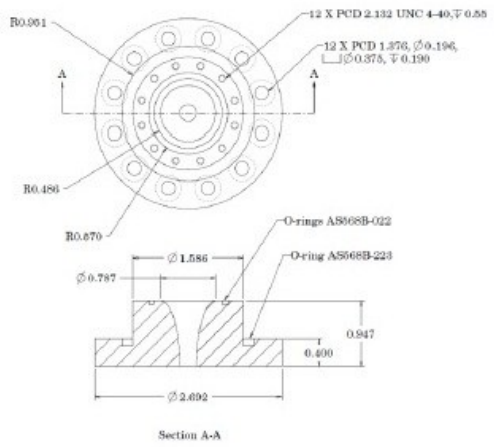

Figure B. 1 Nozzle basic dimensions

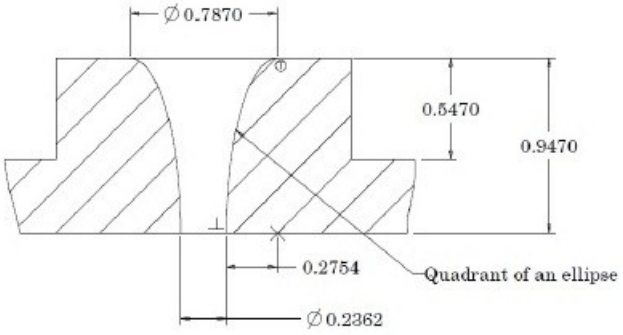

Figure B. 2 Nozzle type A

Appendix C Pressure Transducer Specifications

ICP® High Frequency-General Purpose
With integral electronics

Optional o-ring isolation mounting adaptor is available for blast applications; see page 59.

Dimensions shown in inches except where noted.

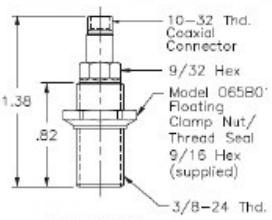

Model 102A12
Ground Isolated

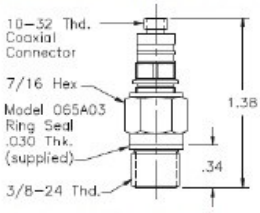

Models 102A, A03, A04, A06, A15
Ground Isolated

Mounting Adaptors on Page 58

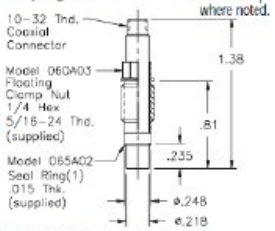

Models 113A21, A22, A23, A24, A26
NEW all Invar Models 113A31, A32, A33, A34, A36

	Dynamic Range (2)	psi	0.05 to 200	0.1 to 500	0.2 to 1000	1 to 5000	2 to 10 000
	MODEL NUMBERS		102A12, A15 113A21 113A31	102A06 113A26 113A36	102A04 113A24 113A34	102A 113A22 113A32	102A03 113A23 113A33
AMPLITUDE	Sensitivity (9)	mV/psi	25	10 ± .5	5 ± .25	1 ± .05	0.5 ± .03
	Resolution	psi	0.003	0.01	0.02	0.1	0.2
	Range (for 5V output)	psi	200	500	1000	5000	10 000
	Range (for 10V output) (3)	psi	400	1000	2000	10 000	20 000
	Maximum Pressure	psi	1000	10 000		15 000	20 000
	Linearity (4)	%FS	≤ 1				
FREQ RESP	Resonant Frequency (5)	kHz	≥ 500				
	Rise Time	µs	≤ 1				
	Discharge Time Constant (6)	sec	≥ 1	≥ 50	≥ 100	≥ 500	≥ 1 000
	Low Frequency (-5%) (6)	Hz	0.5	0.01	0.005	0.001	0.0005
ENVIRONMENTAL	Shock (max)	g pk	20 000				
	Acceleration Sensitivity	psi/g	0.002				
	Temperature Range	°F	-100 to +275				
	Temperature Coefficient	%/°F	≤ 0.03				
	Flash Temperature	°F	3000				
ELECTRICAL	Polarity (positive pressure)		positive				
	Output Impedance	ohm	≤ 100				
	Output Bias	+volts	8 to 14				
	Power Required: Voltage	+VDC	20 to 30				
	Constant Current	mA	2 to 20				
	Ground Isolation	model	102A12, A15	102A06	102A04	102A	102A03
PHYSICAL	Sensing Element	material	quartz				
	Case (7)	material	17-4PH (113A30 series : Invar)				
	Diaphragm (8)	material	Invar				
	Connector (8)	type	10-32 coaxial				
	Sealing (8)	type	epoxy				
OPTIONS	Hermetic Seal (8)	prefix	H				
	Stainless Steel Diaphragm	prefix	S (for series 113A20 only)				
	Emralon Gnd. Isolation Coating	prefix	E (for series 113 only)				
	Negative Polarity	prefix	N				
	Momentum Trap	prefix	T				
	Water-resistant Cable	prefix	W (specify length)				

NOTES:
1. For recess mount, Model 065A06 seal sleeve is available.
2. Measures dynamic pressures from full vacuum to rated maximum.
3. ≥+24 VDC supply required for 10V output. If optional calibration to 10V range is required, linearity specs may change.
4. %FS any calibrated range; zero-based best straight line.
5. Suppressed resonance.
6. Discharge Time Constant (DTC) relates low-frequency to signal lost during transient events at room temperature. See technical section on page 78.
7. Special diaphragm or case material available.
8. Diaphragms of all sensors are welded or integral. Hermetic option specifies a fused-glass electrical connector and welded joints.
9. Unless otherwise designated, sensitivities are ± 15%.

Figure C. 1 PCB 113A32 Pressure transducer specifications

Appendix D Labview® Program Developed for Recording Pressure Time History

Figure D. 1 Labview front end VI

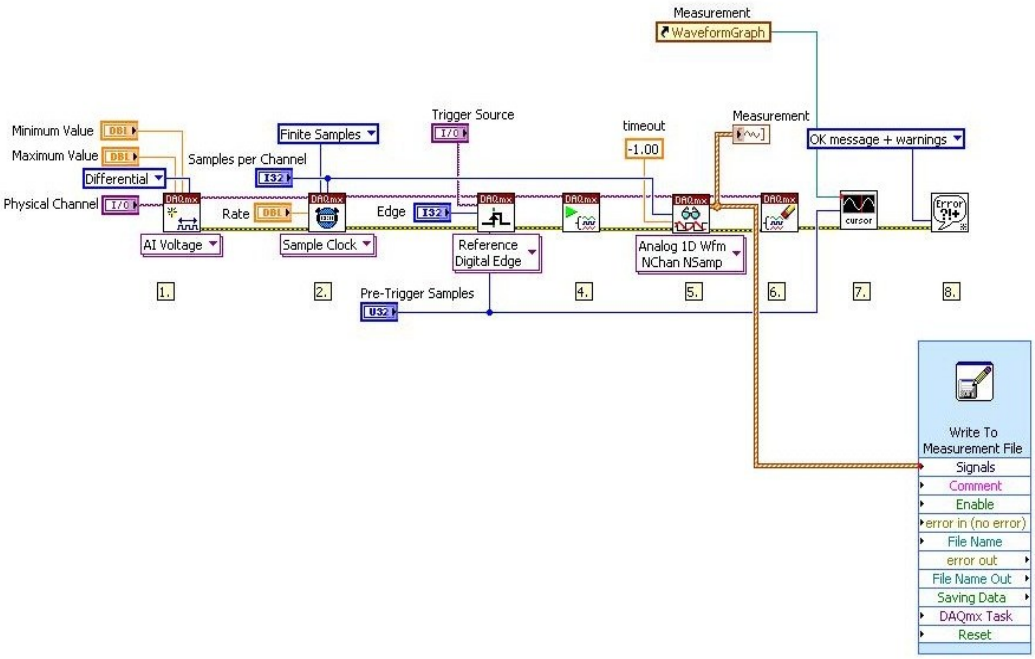

Figure D. 2 Labview block diagram